# Changes in aerosols and clouds following a rapid reduction in emissions: Case studies from the COVID-19 pandemic

by

Ruth A. R. Digby
B.Sc., University of Victoria, 2016
M.Sc., University of Victoria, 2019

A Dissertation Submitted in Partial Fulfillment of the
Requirements for the Degree of

DOCTOR OF PHILOSOPHY

in the School of Earth and Ocean Sciences

Changes in aerosols and clouds following a rapid reduction in emissions:
Case studies from the COVID-19 pandemic

by

Ruth A. R. Digby
B.Sc., University of Victoria, 2016
M.Sc., University of Victoria, 2019

Supervisory Committee

Dr. Adam Monahan, Co-Supervisor
(School of Earth and Ocean Sciences)

Dr. Nathan Gillett, Co-Supervisor
(Canadian Centre for Climate Modeling and Analysis;
School of Earth and Ocean Sciences)

Dr. Knut von Salzen, Departmental Member
(Canadian Centre for Climate Modeling and Analysis;
School of Earth and Ocean Sciences)

Dr. Jason Cole, Outside Member
(Canadian Centre for Climate Modeling and Analysis)

**Supervisory Committee**

Dr. Adam Monahan, Co-Supervisor
(School of Earth and Ocean Sciences)

Dr. Nathan Gillett, Co-Supervisor
(Canadian Centre for Climate Modeling and Analysis;
School of Earth and Ocean Sciences)

Dr. Knut von Salzen, Departmental Member
(Canadian Centre for Climate Modeling and Analysis;
School of Earth and Ocean Sciences)

Dr. Jason Cole, Outside Member
(Canadian Centre for Climate Modeling and Analysis)

## ABSTRACT

This thesis explores the uncertainties in several key aerosol- and cloud-related fields. Although the three projects described here investigate different topics, they are united by a common theme: how well do we understand the impacts of potential changes in emissions?

The first two science chapters revolve around the COVID-19 pandemic and associated changes in anthropogenic activity. Each of these chapters asks two questions. First, did the emissions change in question lead to a statistically significant anomaly in satellite observations of relevant fields? And second, how well do current models reproduce the observed changes?

The first of the COVID-19 chapters explores the impact of reduced aviation on cirrus cloud. Aviation-induced cirrus is the largest source of uncertainty in, and by some estimates may be the largest component of, aviation's net radiative forcing.

Despite a sustained global reduction in air traffic, with April 2020 flight numbers less than 40% of their 2019 levels (FlightRadar24, 2020c), aviation-weighted cirrus coverage was not significantly reduced in Spring 2020. A regression model based on the contrail cirrus simulations of Bock and Burkhardt (2016a) did not exhibit a statistically significant dependence of cirrus anomalies on aviation intensity, and suggested that current models may overestimate the impacts of aviation on cirrus. We apply these results to calculate the first observationally constrained estimate of the radiative forcing of aviation-induced cirrus: (-3, 22) $mW/m^2$, much lower than but consistent with the current best estimate of 57 (17, 98) $mW/m^2$ (Lee 2021).

The second of the COVID-19 chapters explores the impact of reduced aerosol emissions on aerosol optical depth (AOD). Of the regions considered, only India experienced statistically significant reductions in total or dust-subtracted AOD. Earth system model simulations from the CovidMIP experiment over-predict the magnitude of the Spring 2020 total and dust-subtracted AOD anomalies, but this bias can be attributed in part to biases in the model inputs. Through a series of sensitivity tests we demonstrate that, given sufficiently accurate inputs, Earth system models can reproduce the observed total and dust-subtracted AOD anomalies to within observational uncertainty. These results provide confidence in the ability of Earth system models to predict the large-scale aerosol responses to other emission scenarios as well.

The final science chapter of this thesis assesses the sensitivity of black carbon's (BC's) simulated climate impacts to the choice of its refractive index, which determines the extent to which BC absorbs or scatters radiation. We compare ensembles simulated with three values of the refractive index that are commonly used in the climate modeling community. Increasing from low to high absorption can increase simulated global-mean absorbing aerosol optical depth (AAOD) by 42% and effective radiative forcing from BC-radiation interactions (BC ERFari) 47%. The AAOD increase is comparable to that from recent updates to aerosol emission inventories, and in BC source regions, a third as large as the difference in AAOD retrieved from different satellites. The BC ERFari increase is comparable to the scale of the uncertainty in recent literature assessments. Although model sensitivity to the choice of BC refractive index is modulated by other parameterization choices, our results highlight the importance of considering refractive index diversity in model intercomparison projects.

# Contents

# List of Tables

# List of Figures

## ACKNOWLEDGEMENTS

This thesis marks the culmination of four wonderful, difficult years. I am deeply grateful to everyone who has been a part of the journey.

First, to Adam and Nathan. Thank you for being the best supervisors an aspiring researcher could hope for. Your support on matters both academic and personal has been deeply appreciated. I never expected to have this much fun with a PhD, and it's really been thanks to the two of you.

Second, to Knut. From our first exchange you have shown boundless enthusiasm and support for my science. I am so grateful for your mentorship and for the scientific opportunities you've helped to create for me. Here's to many more projects together!

Third, to Jason. My first project would not have been possible without your satellite expertise. Thank you for being so generous with your time and for your many helpful pointers on comparing models with observations, both then and since.

I am twice grateful to Dr. Hansi Singh: for her guidance as a member of my supervisory committee for the first three years of my PhD, and for her Physics of Climate course which was foundational to my understanding of my new field.

To the UVic Climate Lab, especially those of you who joined our virtual coffee sessions that first strange year and built a community despite being scattered across the globe: your friendship (and abstract proofreading) has been such a gift. And to the CCCma, which I am astonished to realize has been my scientific home for half my PhD: thank you for welcoming me so warmly.

Always, to Mum and Dad. You deserve all the credit for my curiosity about and love for the natural world. Mum, your mix of creative vision and gritty practicality are an inspiration, and I channel you in each new project I take on. Dad, from math problems at the kitchen table to the physics of telemarking to the finer points of linseed oil paint, we have explored the world's inner workings together. I would not see the world as I do without you. Thank you both for every phone call, every visit home, every cup of coffee by the river. I am grateful for every moment we've had together.

And finally, to Nic, without whom none of this would have been possible.

The research described in this thesis was carried out in what is now known as Victoria, located on the traditional and unceded territories of the lək̓ʷəŋən and W̱SÁNEĆ peoples. It has been my very great honour to spend the last fourteen years on their territory. As a settler studying climate science, I recognize the deep harm done by historical and ongoing colonial structures which have resulted in both the displacement and disenfranchisement of indigenous peoples, and the climate crisis which I study. May the process of reconciliation teach us to walk more lightly on this earth.

This work was supported by a Canada Graduate Scholarships - Doctoral program award from the Natural Sciences and Engineering Research Council of Canada.

# DEDICATION

*For Dad.*

# Chapter 1

# Introduction

I started my PhD in April 2020, mere weeks after the World Health Organization declared COVID-19 a global pandemic. This thesis is a product of that experience. The projects described in these pages emerged in natural succession as the pandemic shaped our communal behaviour, and they are linked by a common thread: the drive to understand climate responses to current or future changes in human behaviour.

Understanding the climate responses to emission reductions could not be more urgent. Put plainly: the climate is changing (Gulev et al., 2021), and we are responsible (Eyring et al., 2021), and for a myriad of reasons ranging from ecosystem stability (Caretta et al., 2022; Cooley et al., 2022; Parmesan et al., 2022) to human health (Cissé et al., 2022; Reddington et al., 2023) to social justice (Brulle and Pellow, 2006; Deivanayagam et al., 2023; Birkmann et al., 2022), it is critical that we reduce our impact as rapidly as possible. In order to take effective action, we need to understand both our present impacts on the climate and the likely effects of future changes.

In the early months of the COVID-19 pandemic, public health measures were instituted to limit the spread of the virus. These measures, which included domestic and international travel bans, restrictions on public and private gatherings, and in some cases, stay-at-home orders that affected all but the most essential workers (Hale et al., 2021), had the side effect of dramatically reducing emissions from many sectors (Le Quéré et al., 2020; Forster et al., 2020). Collectively referred to as the COVID-19 lockdowns in this work, these changes provided an unprecedented window through which to study human-climate interactions.

Chapters 2 and 3 of this thesis leverage the COVID-19 lockdowns to assess two important but uncertain sources of anthropogenic forcing: aviation and aerosol emissions. In both studies, the observed changes are first examined in their own right and then used to evaluate model simulations. In doing so, we assess first our current impacts on the climate and second our ability to projecct the impacts of potential future changes. Chapter 4 then conducts a model sensitivity analysis to better understand key uncertainties in the climate impacts of one aerosol species, black carbon.

Chapter 2 concerns aviation. The most uncertain, and by its central estimate in a recent multimodel synthesis (Lee et al., 2021) perhaps the largest, component of aviation's effective radiative forcing is aviation-induced cirrus (AIC). Because of its large radiative impact and short lifetime, AIC is a popular target for mitigation strategies, for example through navigational avoidance in which flight paths are diverted away from regions where AIC is likely to persist (Kärcher, 2018; Rosenow et al., 2018; Grewe et al., 2017). However, the efficacy of this approach depends on contrail cirrus having a substantially larger radiative forcing than other aviation sources such as $CO_2$, since rerouting typically results in a longer flight track and correspondingly higher emissions. There is therefore a pressing need to constrain both the current radiative forcing of AIC and the changes in natural cirrus that can occur when air traffic is reduced. Because AIC is challenging both to observe and to simulate (Bock and Burkhardt, 2016b; Burkhardt et al., 2010; Kärcher et al., 2009; Kärcher, 2018; Myhre et al., 2009b), the most effective constraint on AIC is through observations of cirrus fields during large-scale flight groundings (Travis et al., 2002; Hong et al., 2008; Sandhu and Baldini, 2018). In Spring 2020, the COVID-19 lockdowns resulted in an aviation reduction of unprecedented scale (FlightRadar24, 2020b). Chapter 2 first investigates whether remotely sensed observations of cirrus coverage during this period exhibit a statistically significant reduction, and then assesses how well the observed change (or lack thereof) compares with a regression model developed from existing simulations of contrail cirrus (Bock and Burkhardt, 2016a). Based on these findings, we compute the first observationally-derived estimate of the radiative forcing of aviation-induced cirrus.

Chapter 3 concerns aerosols and their response to emission reductions. The Shared Socioeconomic Pathways (SSPs; Riahi et al., 2017) and Representative Concentration Pathways (RCPs; van Vuuren et al., 2011; Lamarque et al., 2011) all project declining aerosol emissions over the coming decades, but the climate and air quality responses to such changes remain uncertain (Szopa et al., 2021). Previous observational constraints on simulated changes have been based on slow (e.g. decadal) emission trends (e.g. Ramachandran et al., 2022; Lund et al., 2023). COVID-19 provides an important opportunity to investigate the impacts of a rapid emission reduction. There are several advantages to studying abrupt perturbations: a short-but-strong signal may be easier to disentangle from other sources of variability, and the study period is short enough that instrument drift is unlikely to be a concern. Crucially for aerosol model evaluation, existing simulations indicate that the presence and severity of undesirable climate responses to emission reductions may be proportional to the rate at which emissions are reduced (Acosta Navarro et al., 2017; Hienola et al., 2018; Samset et al., 2020; Shindell and Smith, 2019; Shindell et al., 2012; Sillmann et al., 2013). Similar to Chapter 2, Chapter 3 first investigates whether remotely sensed observations of total aerosol optical depth (AOD) or dust-subtracted aerosol optical depth (DSAOD) exhibit detectable responses to the Spring 2020 emission reductions, and then assesses how well the observations compare with model simulations. The model evaluation component of Chapter 3 begins with results from the COVID-19 Model Intercomparison Project (CovidMIP; Jones et al., 2021), in which Earth system models simulated COVID-19-like reductions in aerosols and greenhouse gases. We then conduct sensitivity tests in the Canadian Atmosphere Model (CanAM5; Cole et al., 2023) to disentangle the drivers of the DSAOD signal. The appendices to Chapter 3 describe our investigation into the impacts of sampling on observed and simulated AOD. Through this analysis we demonstrate that, given sufficiently accurate model inputs, the observed AOD and DSAOD signals can be reproduced by Earth system models to within observational uncertainty.

Finally, Chapter 4 considers uncertainties in aerosol radiative forcing. Black carbon is the most strongly warming of the aerosols, with particularly important impacts in the Arctic (AMAP, 2021; Sand et al., 2016; von Salzen et al., 2022). It also has serious negative health impacts (Song et al., 2022; Yang et al., 2021; Verma et al., 2021). There is therefore clear motivation to reduce its emissions. Although its effective radiative forcing is understood to be positive, the magnitude of this forcing remains uncertain (AMAP, 2021; Bond et al., 2013; Szopa et al., 2021; Thornhill et al., 2021). Chapter 4 isolates one source of uncertainty: the refractive index, which determines the extent to which an aerosol absorbs and scatters radiation. The refractive index is difficult to constrain in measurements and there is great diversity in the range of values used in Earth system models (Bond and Bergstrom, 2006). We investigate how much the simulated absorbing aerosol optical depth and effective radiative forcing due to BC-radiation interactions can vary when the refractive index is varied across the range of commonly-used values. For the first time, our results demonstrate that the choice of refractive index used in models can have statistically significant impacts on simulated fields commonly used to assess black carbon's climate impacts, comparable to the impacts of other known uncertainties, and that this parameter should be considered whenever model simulations are compared.

The contents of Chapters 2 and 3 have been published as Digby et al. (2021) and Digby et al. (2024) respectively, and at the time of writing, the contents of Chapter 4 had been submitted for consideration in Geophysical Research Letters.

# Chapter 2

# Aviation-Induced Cirrus during COVID-19

Global aviation dropped precipitously during the COVID-19 pandemic, providing an unprecedented opportunity to study aviation-induced cirrus (AIC). AIC is believed to be responsible for over half of aviation-related radiative forcing, but until now, its radiative impact has only been estimated from simulations. Here we show that satellite observations of cirrus cloud do not exhibit a detectable global response to the dramatic aviation reductions of spring 2020. These results indicate that previous model-based estimates may overestimate AIC. In addition, we find no significant response of diurnal surface air temperature range to the 2020 aviation changes, reinforcing the findings of previous studies. Though aviation influences the climate through multiple pathways, our analysis suggests that its warming effect from cirrus changes may be smaller than previously estimated.

The contents of this chapter appeared in Geophysical Research Letters as *An observational constraint on aviation-induced cirrus from the COVID-19-induced flight disruption* (Digby et al., 2021).

## 2.1 Introduction

Aviation is responsible for an estimated 3.5% of anthropogenic effective radiative forcing (ERF) (Lee et al., 2021), a number which has been growing rapidly as air traffic has increased over recent decades. Of this forcing, the largest – and most uncertain – component is the contribution from contrail cirrus, which is estimated to make up $\sim 55\%$ of the total aviation forcing and was calculated at 57 (17, 98) mW/m$^2$ for 2018 in a recent multimodel synthesis (Lee et al., 2021).

Contrail cirrus consists of both linear contrails, which form behind aircraft, and the artificial cirrus cloudiness formed when these linear contrails disperse. Because aircraft emission plumes may be temporarily supersaturated with respect to ice (Minnis et al., 2004), contrails can form in conditions where natural cirrus cannot, and therefore have the potential to substantially impact regional high-level cloudiness (Burkhardt and Kärcher, 2011; Sassen, 1997). High-level cloud is also affected by the aerosols emitted by aircraft, which can serve as ice nuclei; the ice nucleation efficiency of black carbon, in particular, remains uncertain (Karcher et al., 2007; Kärcher et al., 2021; Voigt et al., 2021). Finally, the formation of contrail cirrus can compete with natural cirrus for water vapour, reducing the formation of the latter (Burkhardt and Kärcher, 2011). In this work we will refer to the combination of these effects as aviation-induced cirrus (AIC). Like natural cirrus, the radiative impact of AIC is dominated by its longwave effect, and is expected to decrease the diurnal surface air temperature range (DTR) (Sassen, 1997; Travis and Changnon, 1997; Travis et al., 2002).

Because of its large radiative impact and short lifetime, AIC is a popular target for mitigation strategies aimed at reducing the climate impact of aviation (see, e.g., overview in Kärcher, 2018). One such strategy is navigational avoidance, or the diverting of flight paths away from regions where contrails are likely to form (Kärcher, 2018; Rosenow et al., 2018; Grewe et al., 2017). However, the efficacy of this approach hinges on contrail cirrus having a substantially larger radiative forcing than other aviation sources such as $CO_2$, since rerouting will result in a longer flight track and correspondingly higher emissions. There is therefore substantial interest from both scientific and policy-making communities in a detailed understanding of the radiative impact of AIC.

This radiative impact is extremely difficult to constrain. Once linear contrails disperse into contrail cirrus, they become indistinguishable from natural cirrus, precluding observational studies over the majority of their evolution (Kärcher, 2018; Burkhardt et al., 2010). Possible influences of climate change or changes in other sources of anthropogenic aerosols make it difficult to isolate the impacts of the long-term increase in aviation. Simulating AIC requires a detailed representation of microphysics and particle characteristics (Kärcher, 2018; Kärcher et al., 2009; Bock and Burkhardt, 2016b), and radiative transfer calculations have proven to be sensitive to models' horizontal, vertical, and temporal resolution (Lee et al., 2021; Myhre et al., 2009b), as well as the choice of radiative transfer scheme itself (Myhre et al., 2009b). Indirect sources of AIC (the soot-cloud effect, impacts of AIC on natural cirrus) are even more poorly constrained (Kärcher, 2018; Burkhardt and Kärcher, 2011; Lee et al., 2021). For a detailed discussion of the uncertainties in simulating AIC RF, refer to Lee et al. (2021).

Given the immense challenge of simulating and observing AIC, large-scale flight groundings provide our best probe of the relationships between aviation density, cirrus cover, and DTR. The aviation reductions associated with the COVID-19 pandemic have dwarfed previous flight groundings, which were too short and too geographically limited to yield robust signals (Travis et al., 2002; Hong et al., 2008; Sandhu and Baldini, 2018). In early April 2020, the total number of flights globally fell to $<40\%$ of 2019 levels (FlightRadar24, 2020c), and by December 2020, had only recovered to $\sim75\%$ (FlightRadar24, 2020b). In this work, we investigate whether these unprecedented reductions in global aviation have led to detectable changes in cirrus cover or in DTR.

## 2.2 Data

### 2.2.1 Aviation data

Spatially resolved aviation data were purchased from the global flight tracking service FlightRadar24 (FlightRadar24, 2020a). We obtained flight tracks for all recorded flights on every second Friday from January through July of 2019 and 2020, corresponding to 15 days in each year. Only 30 days' data were purchased for reasons of cost, but the days were selected days to centre around the period of greatest aviation change. Our selection matched days of the week, rather than calendar dates, between 2019 and 2020 due to the weekly cycle in the number of flights.

We interpolate these flight tracks to a $1° \times 1°$ spatial grid and 30-second temporal grid, filtering by altitude ($z > 18{,}000$ft / 5,486m) to include only the flights most likely to form contrails. The resulting flight density distribution is then scaled to areal density (flights per square km). Aviation anomalies are expressed as differences between mean daily aviation densities of particular months in 2020 and 2019. The March-April-May (MAM) mean anomaly is shown in Figure 2.A.1a.

We additionally construct a 21-year aviation timeseries using publicly available data from Airlines for America (A4A; Airlines for America, 2021). We quantify aviation in terms of total kilometres flown, since this metric is the most physically relevant for contrail formation; expressing aviation in terms of annual aircraft departures yields similar results, shown in Figure 2.A.5. In both cases, data correspond to passenger and cargo aircraft, and are only available through 2019.

Although data on total aircraft kilometres flown in 2020 are not readily available, we utilize the facts that (a) there has been a roughly linear relationship between total aircraft kilometres and assigned seat kilometres (AKSs) for the past decade (Airlines for America, 2021), and (b) in 2020, ASKs fell 68.1% over 2019 levels (IATA Pressroom, 2021). We thus obtain a value for aircraft kilometres in 2020 by scaling the kilometres flown in 2019 by a factor of $(1 - 0.681)$.

### 2.2.2 Cirrus data

Cirrus fractions are taken from the Moderate Resolution Imaging Spectroradiometer (MODIS) instruments on the satellites Aqua and Terra (Platnick et al., 2017; King et al., 2013). Aqua and Terra have equatorial overpasses at 1:30 am/pm and 10:30 am/pm local time, respectively.

We use the product *Cirrus_Fraction_Infrared_FMean* from the monthly gridded products MOD08_M3 (Terra) and MYD08_M3 (Aqua), which have $1° \times 1°$ spatial resolutions (King et al., 2013). Anomalies are expressed relative to a linear trend fit to the available historical data, and are calculated individually for each grid cell. Data are available for Terra from February 2000 and for Aqua from July 2002; Aqua's MAM and annual (ANN) means are computed for 2003 onwards.

The majority of our analysis utilizes the MODIS-mean cirrus fraction (i.e. the Aqua-Terra mean, spanning 2003-2020), though we show results for the satellites individually for completeness. MAM 2020 MODIS-mean anomalies are shown in Figure 2.A.1b.

### 2.2.3 Temperature data

Temperature data are taken from two sources: European Centre for Medium-Range Weather Forecasts (ECMWF) 5th Generation Reanalysis (ERA5) (Hersbach et al., 2018), which has the advantage of homogeneous, gridded spatial coverage, and Global Historical Climatology Network (GHCN) stations (Menne et al., 2012a,b), which have the advantage of being instrumental station data but which have an extremely heterogeneous distribution.

ERA5 values are calculated from the dataset *ERA5 hourly data on single levels from 1979 to present*, which provides 2m temperature minima and maxima on a $1° \times 1°$ spatial grid. GHCN weather station data are computed from the GHCN-D daily dataset. From this dataset we select only stations from the World Meteorological Organization (WMO) network which have more than 20 days' records in a given month, for every year from 2000-2020. These filters greatly reduce the number of available stations, but improve the reliability of the resulting anomalies. We have repeated our analysis requiring only 15 years' records; although this approximately doubles the number of available stations, our conclusions are unaffected, and the change in spatial sampling with time introduces spurious signals which can be misleading at first glance. We therefore maintain the more rigorous selection to avoid confusion.

DTR anomalies are expressed relative to a linear trend fit to the 2000-2019 data, and are calculated individually for each station or grid cell. MAM 2020 anomalies derived from ERA5 and GHCN data are shown in Figs. 2.A.2c and 2.A.2d respectively.

## 2.3 Results

Our analysis consists of two components: first, assessing the observed response of cirrus cover and DTR to changes in aviation during 2020, relative to their typical interannual variability; and second, comparing those observations to estimates of the expected signal strength derived from the application of a statistical model to pre-existing simulations of aviation-induced cirrus. In both stages we restrict our analysis to the region between 75° N and 75° S, as the satellite cirrus products we use are unreliable at higher latitudes (Hubanks et al., 2020). We emphasize that the results presented here describe the net effect of aviation on cirrus cloud, which includes not only the formation of contrails but also any interactions between contrail cirrus and natural cirrus, or between (contrail or natural) cirrus and the aerosols emitted by aircraft.

### 2.3.1 Observed response

As shown in Figure 2.A.1a, the 2020 aviation density anomalies – which closely resemble the typical aviation density distribution, not shown – are extremely regionalised. Aviation-induced changes in cirrus cover or DTR would therefore not be expected over large regions of the globe. To account for this we weight our observations by the 2019 aviation density distribution, which focuses the analysis on regions where aviation is important without selecting arbitrary regions for analysis. We weight by the mean 2019 aviation density rather than by the change in aviation from 2019 to 2020 to avoid having a combination of positive and negative weights, as aviation levels did increase in 2020 in a small number of grid cells. The details of this calculation are described in Appendix 2.A.1.

Figure 2.1 shows the typical values and variability of aviation, cirrus fraction, and DTR over 2000-2020. Air traffic is expressed in terms of annual kilometres flown, and the anomalies in panel (d) are expressed as a percent change relative to a linear trend fit to the 2000-2019 values. The centre and right-hand columns show aviation-weighted, MAM-mean cirrus fraction and DTR respectively; MAM is the three-month period containing the largest COVID-19-induced aviation reduction.

The centre column of Figure 2.1 plots cirrus measurements taken from the Aqua and Terra satellites individually, and the average of the two. In all three timeseries, the 2020 cirrus fraction anomalies are not statistically significant at the 5% level. Interestingly, the two MODIS satellites observe opposite tendencies in their cirrus data. These trends are discussed further in Appendix 2.A.2.

In the right-hand column of Figure 2.1, orange and yellow lines correspond to DTR measurements taken from ERA5 reanalysis and GHCN weather stations, respectively. The discrepancy between their measurements is due to a combination of the heterogeneous spatial sampling of the GHCN stations, and a $\sim 2°$C offset between the two datasets when sampled over the same locations (Figure 2.A.2). Despite these discrepancies, the two datasets yield the same result: aviation-weighted DTR showed no response to the COVID-19-induced aviation reductions.

The month-by-month evolution of aviation, cirrus fraction, and DTR anomalies

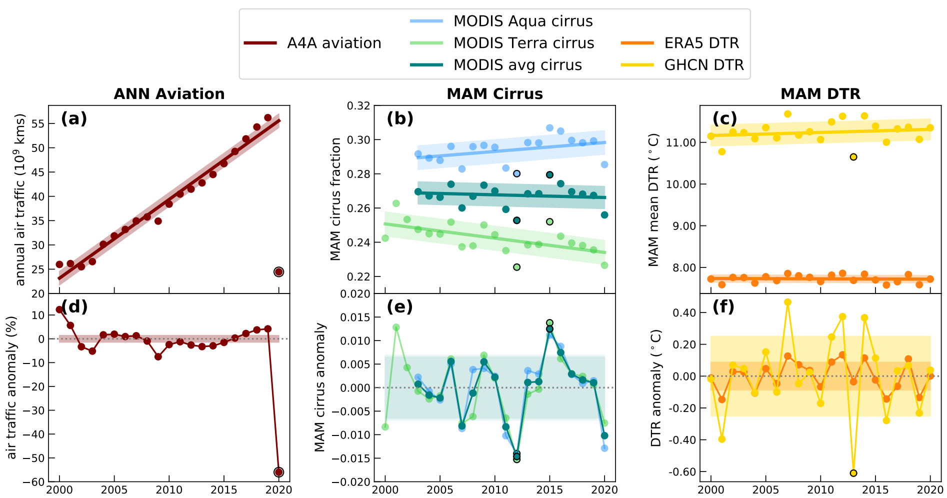


Figure 2.1: Evolution of air traffic, cirrus fraction, and DTR over 2000-2020. *Left* (panels a, d): annual-mean aviation intensity, expressed in billions of kilometres flown. *Centre, right* (panels b/e, c/f): MAM-mean, aviation-weighted values and detrended anomalies of cirrus fraction and DTR respectively. In all panels, solid lines show the linear trend fits, shaded regions indicate $\pm 1\sigma$, and black outlines identify anomalies which are statistically significant at the 5% level relative to the other years in the timeseries. The differences between DTR values calculated from ERA5 and GHCN data in panel (c) can be ascribed to the heterogeneous spatial distribution of GHCN stations, combined with a $\sim 2°$C offset between the two datasets (Figure 2.A.2).

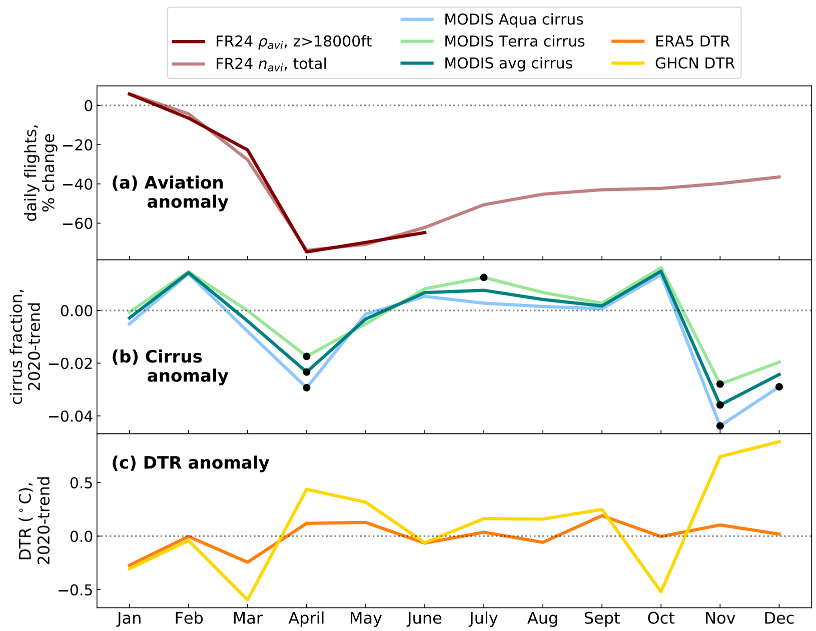


Figure 2.2: Monthly-mean anomalies of aviation, aviation-weighted cirrus fraction, and aviation- weighted DTR through 2020. Aviation anomalies (panel a) are expressed as a percent change over 2019 values of high-altitude aviation density and commercial flight departures (dark and light lines, respectively). The anomalies in panels (b) and (c) are expressed as an absolute change relative to a linear trend fit to the 2000-2019 values. Trends are calculated separately for each grid cell in each month. Black circles in panel (b) indicate months in 2020 where anomalies are statistically significant at the 5% level relative to their values through the reference period; significance tests were not conducted for aviation, as the anomalies are computed relative to 2019 only, and none of the DTR measurements in panel (c) were statistically significant.

through 2020 is examined in Figure 2.2. Aviation anomalies were largest in April 2020. Although cirrus fraction and DTR anomalies showed sizeable excursions around this time, these anomalies are not exceptional when compared to other excursions which occurred later in the year when the aviation signal was much smaller. Moreover, the low cirrus fraction and high DTR observed in April 2020 were driven by anomalies in Europe, which had an exceptionally clear spring with record-breaking levels of solar irradiance (Madge, 2020; van Heerwaarden et al., 2021). It has been elsewhere demonstrated that this event was not due to the reduced contrails and aerosols of the COVID-19 pandemic, but to meteorological conditions (van Heerwaarden et al., 2021; Schumann et al., 2021). Finally, joint distributions of individual grid cell anomalies (Figure 2.A.3) do not suggest dependence on aviation changes.

### 2.3.2 Comparison with simulated response

We next investigate whether existing simulations of AIC would predict a detectable cirrus response to the 2020 aviation reduction, and whether the observed changes are consistent with the magnitude of that simulated response.

We start with a simulated global distribution of contrail cirrus coverage for the year 2006, taken from (Bock and Burkhardt, 2016a, hereafter BB16). These simulations were produced using the contrail cirrus parametrization ECHAM5-CCmod, developed for the climate model ECHAM5 (Bock and Burkhardt, 2016b). Following their example we restrict our consideration to the subset of contrail cirrus with optical depths $\tau \geq 0.05$, which has been shown to be the best threshold for comparison with satellite observations over the United States (Kärcher et al., 2009; Bock and Burkhardt, 2016a).

Only a subset of this contrail cirrus would contribute to an increase in total cirrus cover. To account for overlap with naturally occurring cirrus, we scale the BB16 contrail cirrus map by the fraction of contrail cirrus contributing to an increase in *total* cloud cover, shown in their Figure 6b. Since this scale factor corresponds to overlap with all cloud types, and we are interested only in overlap with cirrus, it will tend to underestimate the simulated aviation-induced change in cirrus. We discuss the sensitivity of our results to this choice of scaling in Appendix 2.A.3.

We then build a multiple linear regression model for cirrus anomalies as follows. Let $\mathbf{x}(t)$ be the annual mean cirrus anomaly field; $\mathbf{x}^{(\mathbf{s})}$ be the fixed simulated contrail cirrus field for 2006, scaled to account for overlap; and $a(t)$ be the aviation intensity normalized such that $a(2006) = 1$. We can then write,

$$\mathbf{x}(t) = \mathbf{h_0} + c_a \mathbf{x^{(s)}} a(t) + \mathbf{h_t} t + \mathbf{w}(t) \tag{2.1}$$

where $\mathbf{w}(t)$ is the field of meteorological noise and $\mathbf{h_0}$, $c_a$, and $\mathbf{h_t}$ are fixed. If the simulated cirrus response to aviation was perfectly modelled we would expect $c_a = 1$.

We can simplify this expression by taking the dot product of both sides with $\mathbf{x^{(s)}}$, and then dividing by the squared norm of $\mathbf{x^{(s)}}$:

$$\frac{\mathbf{x^{(s)}} \cdot \mathbf{x}(t)}{\mathbf{x^{(s)}} \cdot \mathbf{x^{(s)}}} = \frac{\mathbf{x^{(s)}} \cdot \mathbf{h_0}}{\mathbf{x^{(s)}} \cdot \mathbf{x^{(s)}}} + c_a a(t) + \frac{\mathbf{x^{(s)}} \cdot \mathbf{h_t}}{\mathbf{x^{(s)}} \cdot \mathbf{x^{(s)}}} t + \frac{\mathbf{x^{(s)}} \cdot \mathbf{w}(t)}{\mathbf{x^{(s)}} \cdot \mathbf{x^{(s)}}} \tag{2.2}$$

which can be written

$$\beta(t) = c_0 + c_a a(t) + c_t t + e(t) \tag{2.3}$$

The term $c_t t$ (from the field $\mathbf{h_t}$) is included to account for the possibility of an unspecified linear trend due to the effects of climate change or changes in anthropogenic aerosols from non-aviation sources (Kärcher, 2017). Since we include a linear trend in our regression, we do not detrend the observed cirrus anomalies here, in contrast to the previous analyses; anomalies are simply expressed relative to the mean cirrus distribution for 2000-2019.

This model relies on two fundamental assumptions: first, that contrail cirrus production scales linearly with aviation, and second, that the spatial pattern of aviation-induced cirrus has not changed over time.

The first assumption is consistent with the findings of Bickel et al. (2020), who investigate the scaling of RF and ERF from contrail cirrus with changes in aviation density. Although they report a nonlinear response due to saturation effects at high aviation densities, in the range of densities considered here, departures from linearity appear to be small.

The second assumption is of greater potential concern. Aviation growth has not been spatially uniform: over the period of analysis, the proportional increase of aviation in East Asia and India has been much larger than that in Europe or North America. To test the sensitivity of our results to this simplifying assumption, we conduct our analysis both for the entire globe (restricted, as above, to the range 75° S to 75° N) and for a subregion containing North America, the North Atlantic, and Europe (NAm-Eur; 130° W to 45° E, 20° N to 65° N).

The results of these analyses are shown in Figure 2.3. We fit Eqn. 2.3 separately for cirrus measured by Aqua, Terra, and the average of the two. We quantify aviation in terms of total kilometres flown, since this metric is the most physically relevant for contrail formation. For completeness, we repeat the analysis using the annual number of flights; these results are shown in Figure 2.A.5, and the values of $c_a$ for all combinations of dataset and domain are summarized in Table 2.A.1.

Our results indicate that, in all cases but one, the response of cirrus to changes in aviation is not statistically detectable ($c_a$ is consistent with zero), and is considerably smaller than would be predicted from simulated contrail cirrus levels given our assumptions ($c_a < 1$). When $c_a$ is calculated for the Global domain using cirrus measurements from Aqua only, its result is neither consistent with zero nor with one, indicating a response which is statistically detectable but nevertheless smaller than that predicted from our model.

Our bootstrapped confidence intervals describe the expected range of meteorological variability. Had the intervals we calculate here been centred on one (i.e., had the model and assumptions described above perfectly represented the response of cirrus coverage to changes in aviation over time), none of them would intersect zero. Thus we can conclude that these models predict a detectable signal which does not appear in satellite observations (except, again, for in the Aqua-based calculation of a Global $c_a$).

Our regression model also indicates the presence of a small, and statistically insignificant, negative linear trend in $\beta(t)$ for all of the above cases. The MODIS-average predictions are $c_t = -0.01\,(-0.03,\, 0.08)$ and $c_t = -0.01\,(-0.03,\, 0.02)$ for the Global and NAm-Eur domains respectively. We have investigated the effects of autocorrelation on the estimation of $c_a$ and $c_t$, and find a negligible impact on the resulting confidence intervals.

## 2.4 Discussion and conclusions

We have investigated the response of cirrus cover and diurnal surface air temperature range (DTR) to the rapid decrease in aviation that occurred in response to the COVID-19 pandemic. Neither cirrus nor DTR exhibit a response to these aviation changes which is outside the range of natural variability. Comparison with previous model simulations of aviation-induced cirrus indicates that our observations are consistent with a response which is significantly smaller than that simulated.

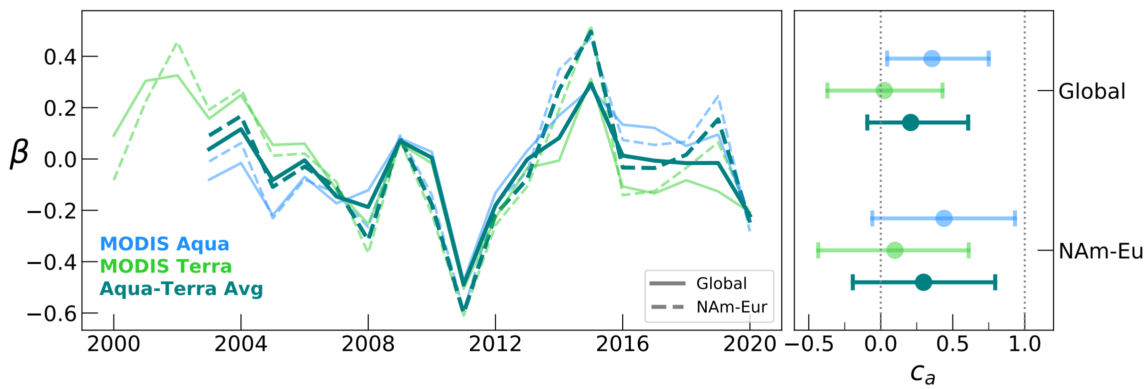


Figure 2.3: Lines (left panel) show the time series of $\beta$ (the normalized dot product of observed cirrus anomalies on the simulated contrail cirrus pattern from Bock and Burkhardt (2016a), Eqn. 2.2-2.3). Solid lines indicate global quantities, and dashed lines correspond to the NAm-Eur subregion. Points (right panel) show the regression coefficients $c_a$ from Eqn. 2.3, with error bars spanning the bootstrapped 5-95% confidence intervals. In both panels, light blue and light green quantities correspond to results obtained using cirrus measurements from Aqua and Terra respectively; darker teal quantities are derived using the MODIS mean. The numerical values of $c_a$ are summarized in Table 2.A.1.

The absence of a detectable DTR response strongly suggests that apparent changes in DTR identified after previous much shorter and more geographically-limited flight disruptions (Travis et al., 2002; Hong et al., 2008; Sandhu and Baldini, 2018) are unlikely to have been driven by changes in aviation.

We have assumed in our analysis that other (non-aviation) changes during COVID-19, such as decreases in aerosol emissions at ground level, had a negligible effect on cirrus cover. Our results could also be sensitive to the method by which we account for overlap between natural cirrus and AIC. Sensitivity analyses addressing both of these issues are described in the appendix. They do not affect our conclusions.

Our observations have identified linear trends in cirrus coverage over the past 20 years, in both aviation-weighted (Figure 2.1) and unweighted (Appendix 2.A.2) global means. These trends, which differ in sign between Aqua and Terra, are interesting in their own right and deserving of a separate, dedicated analysis beyond that which we present in the appendix.

### 2.4.1 Comparison with other COVID-19 studies

Our observational non-detection of a cirrus response is broadly consistent with the results of Gettelman et al. (2021), who found the impacts of COVID-19 on high cloud to be smaller than the internal variability. However, their analysis considered annual mean quantities, and we would not expect to see a contrail cirrus response when averaged over such a long time period given the recovery of aviation levels throughout the year. Their results are therefore not directly comparable to ours.

Schumann et al. (2021) reported that changes in cirrus optical thickness and outgoing longwave radiation over Europe in spring and summer 2020, relative to 2019, were dominated by meteorology, but that the agreement between cirrus optical thicknesses in their model and observations increased slightly when the model incorporated contrails. Although their results are suggestive of a small aviation-induced cirrus response over Europe in 2020, their simulated response may be *weaker* than the observed response (their Figure S1), which is opposite to our global result. Overall, their findings suggest a low signal-to-noise ratio, consistent with our results.

Finally, (Quaas et al., 2021, hereafter Q21) investigate MAM-mean changes in the Northern Hemisphere midlatitudes. They report that cirrus coverage was approximately unchanged in low-aviation regions, but decreased $\sim$5% and 9% in the regions with the second-highest and highest 20% of air traffic respectively. It is worth noting that these anomalies were not outside the range of the preceding 10 years' variability, except perhaps for the highest-traffic region where 2020 cirrus levels appear comparable to or slightly lower than the next lowest recorded value (that from 2012). This magnitude of response is consistent with our Figure 2.1.

Our study primarily differs from Q21 in our methods of accounting for the high natural variability of cirrus coverage. Q21 compare measured cirrus levels in 2020 to those in different years with similar circulation conditions; in essence, they attempt to predict cirrus occurrence using the 500 hPa geopotential height. Because of the limited sample available in the observational record and the imperfect link between 500 hPa height and cirrus, the residual changes in cirrus that they measure would still include an unknown contribution from internal variability, which is extremely difficult to characterise. To avoid this issue and ensure that the uncertainties calculated in our comparison of the simulated and modelled responses are as robust as possible, we therefore adopt the complementary approach of investigating whether observations exhibit a response which is outside the range of natural variability, comparing this response to climate simulations, and using bootstrapping to estimate the uncertainty due to meteorological variability.

### 2.4.2 Implications for radiative forcing

A detailed assessment of the climate impacts of AIC, or of its reduction during COVID-19, is outside the scope of this work. We have looked exclusively at changes in cirrus extent; ERF depends also on the cirrus' optical thickness (Kärcher, 2018; Burkhardt and Kärcher, 2011) and on what surface the cirrus overlays (Yang et al., 2010). Optical thickness is in turn a function of ice crystal properties (shape, size, and number) and of ambient conditions (e.g. temperature, humidity, wind shear) (Kärcher et al., 2009; Yang et al., 2010; Bock and Burkhardt, 2016a; Kärcher et al., 2021). The net effect of these properties may not be independent of cirrus coverage. However, we can make some simple inferences.

First, it is reasonable to expect that if our observations indicate a smaller response of cirrus coverage to aviation than is modelled by BB16, the resultant ERF will also be smaller.

Second, we can extend our comparison from BB16 to the current literature best estimate using the detailed multimodel synthesis of (Lee et al., 2021, hereafter L21). Their assessment of the radiative forcing from contrail cirrus drew on results from 5 global models, with corrections applied to account for differences in methodology including aviation inventory, temporal resolution, and radiative transfer scheme. Once these differences had been accounted for, the contrail cirrus ERF determined by BB16 was the smallest of those considered. Our observations are therefore consistent with an AIC ERF which is not only smaller than that computed by BB16, but is smaller than was found by any of the studies considered in L21.

Finally, we can use the results of BB16 and L21 to derive a back-of-the-envelope estimate for the AIC ERF implied by our observations. We emphasize that this estimate is a highly simplified approach to a very nuanced problem, and our results should not be treated as truly quantitative. A detailed description of the calculation, and of the necessary approximations involved, is provided in Appendix 2.A.4. With these approximations we find an AIC ERF of $8\,(-3,\,22)\,\mathrm{mWm^{-2}}$ for 2018, well below the L21 best estimate of $57\,(17,\,98)\,\mathrm{mWm^{-2}}$. Reassuringly, however, the uncertainty ranges of these two estimates do overlap.

Our results suggest that the navigational avoidance of potential contrail-forming regions is not yet a viable solution. If the ERF of AIC is indeed lower than previously believed, then the necessary increase of fossil fuel consumption caused by rerouting may result in a net increase in aviation's climate impact.

### 2.4.3 Conclusions

In conclusion, we find that observations of cirrus and DTR during COVID-19 do not exhibit a detectable response to the rapid reduction in air traffic, whereas models suggest that a cirrus response should have been detectable despite the large natural variability of natural cirrus. Together our results imply that, although aviation influences climate through multiple processes, the cirrus-mediated effect of aviation may be smaller than previously estimated.

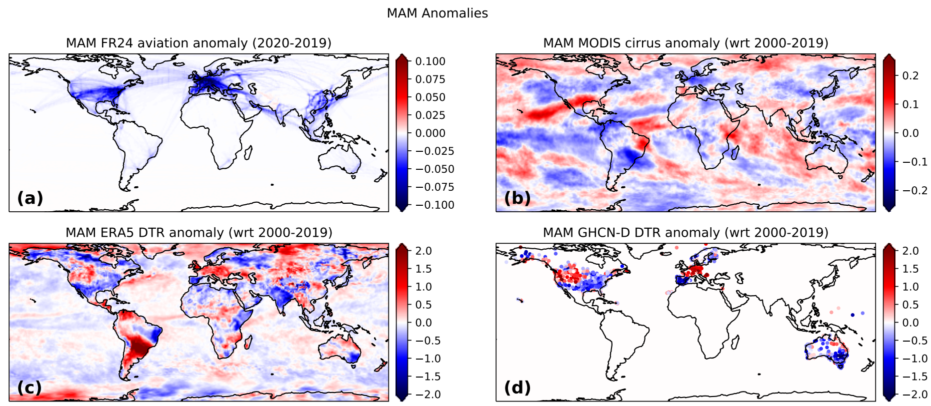


Figure 2.A.1: Global distribution of mean (a) aviation density [flights/km$^2$], (b) MODIS cirrus fraction, (c) ERA5 DTR [°C], and (d) GHCN DTR [°C] anomalies, averaged over March-May 2020. Aviation density anomalies are calculated with respect to the 2019 density distribution, and cirrus and DTR anomalies with respect to a linear trend fit to the 2000-2019 data. Cirrus in panel (b) is the average of measurements taken from the satellites Aqua and Terra.

# 2.A Appendix to Chapter 2

## 2.A.1 Calculation of aviation-weighted means

The aviation-weighted mean $\mu_{avi}$ of a global quantity $x$ is calculated as

$$\mu_{avi} = \sum_i (x_i \rho_i) / \sum_i \rho_i \tag{2.A.1}$$

where $\rho_i$ is the mean January-June 2019 aviation density in grid cell $i$, and the sum is over all $1° \times 1°$ grid cells. We weight by the mean 2019 aviation density rather than by the change in aviation from 2019 to 2020 to avoid having a combination of positive and negative weights, as aviation levels did increase in 2020 in a small number of grid cells.

The global distributions of MAM 2020 anomalies in aviation density, MODIS cirrus fraction, and DTR from ERA5 and GHCN are shown in Figure 2.A.1. Aviation density anomalies are calculated relative to 2019 and cirrus and DTR anomalies are relative to a linear trend fit to the 2000-2019 data.

### 2.A.2 Further analysis of observational data products

#### Comparing DTR measurements from ERA5 and GHCN

Our analysis utilizes DTR measurements from two sources: ERA5 reanalysis, which has the advantage of homogeneous, gridded spatial coverage, and GHCN weather stations, which have the advantage of being instrumental station data but which have an extremely heterogeneous distribution. Figure 2.1c shows an apparent $\sim$3.5 degree discrepancy between the aviation-weighted MAM DTR values from these two stations, with GHCN recording systematically larger temperature ranges. In Figure 2.1f, which shows the detrended anomalies of these two quantities, GHCN shows generally the same behaviour as ERA5 but with larger excursions.

There are two sources of discrepancy between the datasets. First, as seen in Figure 2.A.1, our GHCN stations are largely confined to the United States, Europe, and Australia. This distribution is due in part to our requirement for all stations to have WMO IDs and to have a full 21 years' record. Weighting by the 2019 aviation distribution (which is very similar to the distribution of anomalies in Figure 2.1a) enhances the signal in the United States, Europe, and China, and suppresses it elsewhere; because our GHCN data lacks stations in China, the ERA5 and GHCN results will be sampling different regions.

We account for these spatial differences in Figure 2.A.2, which compares GHCN station data to values from the corresponding 1x1° ERA5 grid cells. Panels (a) and (b) plot colocated GHCN and ERA5 values against one another for MAM 2020; panels (c) and (d) show the aviation-weighted MAM values of GHCN stations and colocated ERA5 grid cells over 2000-2020.

From this figure it is evident that spatial differences account for a portion, but not all, of the difference between GHCN and ERA5 DTR values. There remains a $\sim$1.9°C offset between the two. This offset may be due to the spatial averaging inherent in a 1x1° grid cell as compared to an individual station.

#### Trends in annual-mean cirrus coverage

The two MODIS satellites observe opposite tendencies in their cirrus data (Figure 2.1b): in Aqua, the aviation-weighted MAM cirrus fraction increases 0.81%/decade, whereas Terra observes a decrease of -0.72%/decade; the MODIS-mean trend is 0.16%/decade. Percentages here are a measure of cirrus fraction (i.e. the MODIS-mean trend is a linear increase of 0.0016/decade); we have expressed our trends as

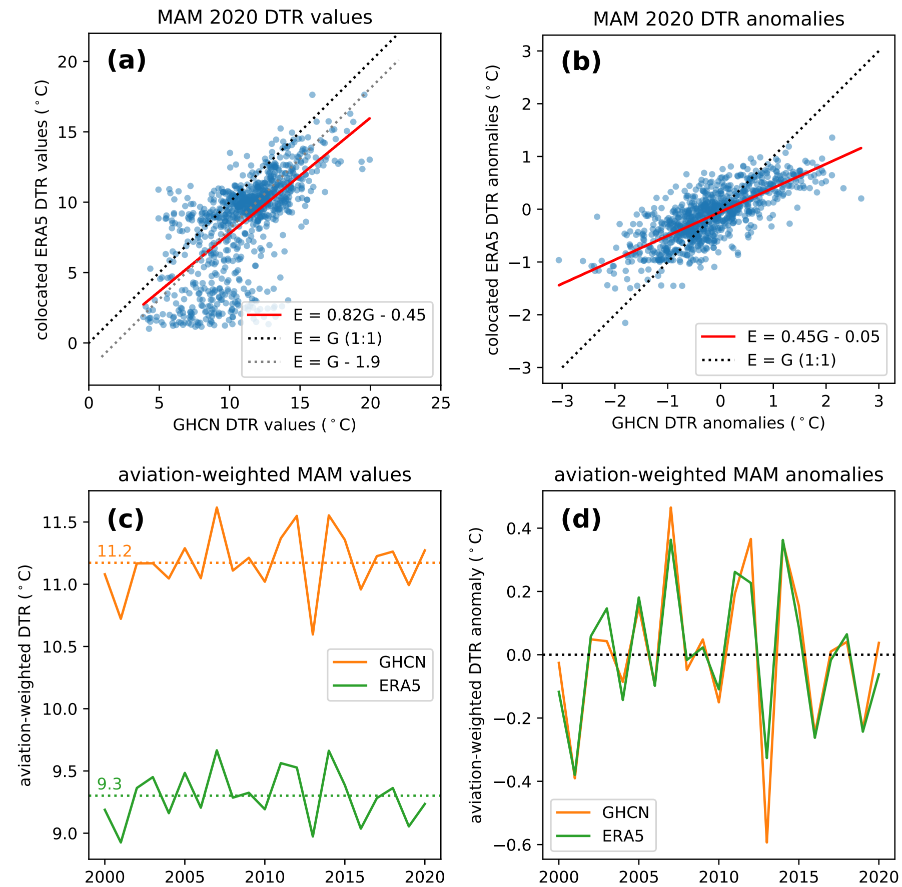


Figure 2.A.2: Comparison of DTR measurements taken from GHCN weather stations and from colocated ERA5 reanalysis grid cells. Panels (a) and (b) plot the MAM 2020 DTR values and anomalies, respectively, from GHCN and ERA5 against one another. Dotted black lines show a 1:1 relationship to guide the eye, and red lines show the results of an ordinary least squares fit to the data. In panel (a), the dotted grey line shows a 1:1 fit shifted downwards by 1.9°C. Panels (c) and (d) plot timeseries of aviation-weighted MAM GHCN and colocated ERA5 values and anomalies over 2000-2020. Dotted lines in panel (c) indicate the timeseries means. When the different spatial sampling of the two datasets is accounted for, they exhibit similar behaviour with an offset of ∼1.9°C.

percent per decade for comparison with literature estimates. The trends calculated for Aqua and Terra individually are both statistically significant at the 5% level, but the MODIS-mean trend is not statistically significant.

For comparison with literature estimates we also calculate the non-aviation-weighted, 75°S to 75°N mean trends in annual-mean cirrus fraction. Trends for Aqua and Terra are 0.10%/decade and -0.35%/decade respectively, and the MODIS-mean trend is -0.13%/decade; of these three, only the Terra trend is statistically significant at the 5% level. The MODIS-mean trend is not equal to the mean of the individual satellites' trends because they are fit over different domains (Terra over 2000-2019, Aqua and the average over 2003-2019); when all trends are fit to the 2003-2019 data, the MODIS-mean trend is equal to the mean of the two satellites' trends as expected.

There are few recent studies on trends in global cirrus cover against which these estimates can be compared. Zerefos et al. (2003) and Stordal et al. (2005) analyzed ISCCP cirrus observations for 1984-1998 and 1984-1999 respectively; both found that cirrus in high-aviation regions increased by a few percent per decade whereas cirrus in neighbouring low-aviation regions had statistically insignificant but typically negative trends. More recently, Quaas et al. (2021) reported a $\sim$2-3%/decade increase in MAM cirrus coverage over 2011-2019 in high-aviation regions but no statistically significant changes in neighbouring low-aviation regions.

The above sources broadly agree on not statistically significant but predominantly negative cirrus trends in low-aviation regions, which is consistent with our results. However, our aviation-weighted trends are substantially lower than those reported elsewhere. Of most relevance is the comparison with Quaas et al. (2021), whose data and timeframe are most similar to our own. However, we note that their trend was fit to the shorter period, and that 2011 and 2012 both had anomalously low aviation-weighted cirrus values; when we fit our aviation-weighted MAM cirrus values over this restricted time period we obtain a MODIS-mean trend of 1.45%/decade.

### 2.A.3 Sensitivity tests

#### Joint distributions of global anomalies

Because even aviation-weighted spatial averages may mask potential local responses, we plot in Figure 2.A.3 the joint distributions of MAM aviation density, cirrus fraction, and DTR across individual grid cells. Here cirrus fractions are the MODIS average and DTR is taken from ERA5. Panels (a) and (b) appear to suggest a relationship between aviation density and each of cirrus fraction and DTR for the largest negative aviation density anomalies. There is in particular the appearance of a relationship between the largest reductions in aviation density and increases in cirrus fraction. We investigate this tail more closely in panel (d), which plots the timeseries of cirrus anomalies for grid cells which had aviation density anomalies below -0.05 flights/km$^2$ (blue) and -0.10 flights/km$^2$ (orange). The 2020 cirrus excursion for these high-anomaly cells is not substantially larger than that seen in previous years, particularly when positive excursions are also considered. Although the 2020 excursion appears statistically significant at the 5% level using a 2-sided Student's t-test, so do the excursions in 2000 and 2010 (the latter only being significant for the moderate threshold). We emphasize that the high-anomaly tail is primarily located in Europe, which had an unusually clear spring with record-breaking irradiance levels that have been attributed to causes other than the COVID-19 pandemic van Heerwaarden et al. (2021).

### Sensitivity to other changes during COVID-19

We use models from the CovidMIP project Jones et al. (2021) to test our assumption that the effects of reducing aviation can be isolated from concurrent reductions in surface emissions of greenhouse gases and aerosols. CovidMIP is a model intercomparison project which simulates the emission reductions associated with the COVID-19 pandemic (scenario *ssp245-covid*) relative to a baseline scenario without these changes (*ssp245*). CovidMIP models do not explicitly simulate aviation, so any changes in their high cloud under ssp245-covid relative to ssp245 must be due to changes in surface emissions.

We select for analysis a subset of CovidMIP models (CanESM5, MIROC, MPI-M, and MRI) which have cloud data available from 2015 onwards. For each model, we calculate a baseline high-cloud fraction using the period 2015-2019 under ssp245. We then compare 2020 high cloud anomalies relative to this baseline in each of *ssp245* and *ssp245-covid*.

High cloud fractions are calculated by taking the maximum cloud fraction at model levels with $p$ <400 hPa. The determination of this threshold, and measurement of the maximum cloud fraction above it, are computed independently for each cell.

The results of this analysis are shown in Figure 2.A.4. The absence of significant difference between the two scenarios provides evidence that changes in surface emis-

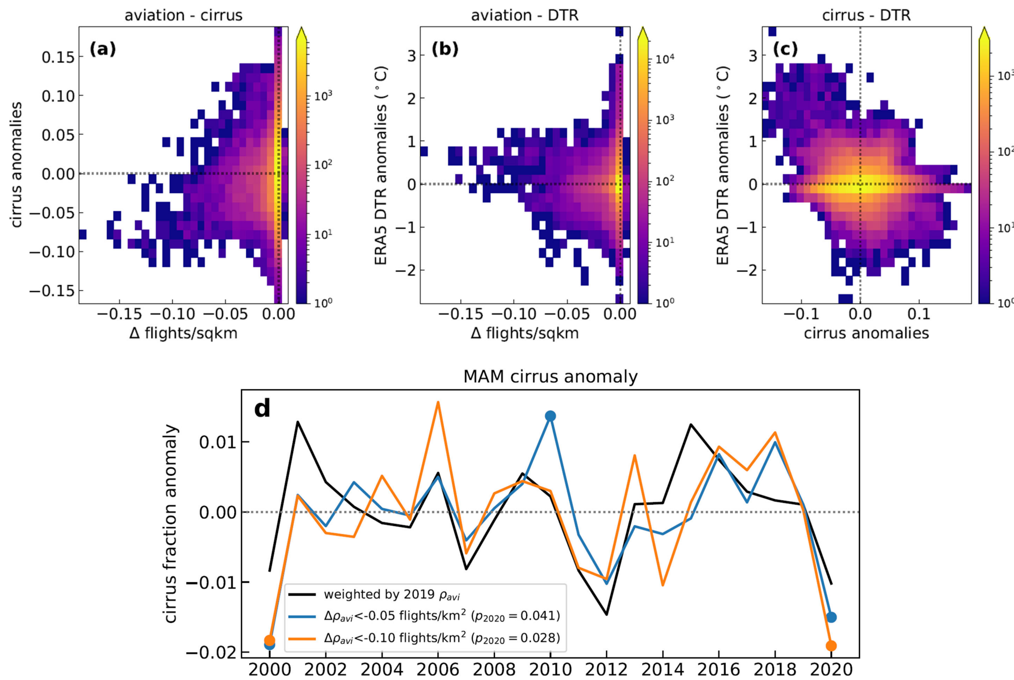


Figure 2.A.3: Histogram estimates of joint distributions of gridded (a) global aviation and cirrus anomalies, (b) global aviation and ERA5 DTR anomalies, and (c) global cirrus and DTR anomalies. All anomalies are for March-April-May 2020, and cirrus is the Aqua-Terra average. Panel (d) shows the timeseries of cirrus anomalies in cells with $\Delta\rho_{avi,2020} < -0.05$ flights/km$^2$ (blue) and $< -0.10$ flights/km$^2$ (orange), with the aviation-weighted global mean shown in black for reference. Circles indicate anomalies that are statistically significant at the 95% level. Cirrus measurements prior to 2003 are from Terra only; those from 2003-2020 are the Aqua-Terra average. Note that although the 2020 excursion is statistically significant under this test, so are the 2000 and 2010 excursions. We also emphasize that the substantial majority of this high-anomaly tail comes from Europe, which experienced record-breaking solar irradiance for reasons unrelated to the pandemic van Heerwaarden et al. (2021).

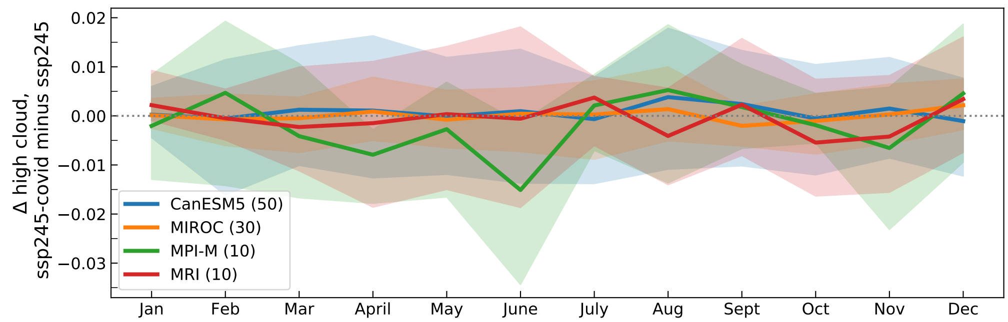


Figure 2.A.4: Difference between ensemble-mean high cloud changes in ssp245-covid (which simulates emission reductions associated with the COVID-19 pandemic) and ssp245 (baseline scenario). For each scenario we calculate an ensemble- mean anomaly in 2020 relative to the preceding 5 years. The difference between these anomalies shows the impact of emission reductions on high cloud cover. As there is little or no difference between the scenarios, we can conclude that changes in surface emissions during COVID-19 did not impact high-altitude cloud, and that any changes in observed cirrus are due to changes in aviation only. Shaded regions indicate the 16-84th percentile ranges across the model ensembles, and the numbers next to each model name in the legend indicate the ensemble sizes.

sions during COVID-19 did not impact high-altitude cloud, and that any changes in observed cirrus are due to changes in aviation only. Although there may be mechanisms of cirrus response to surface aerosols that are not represented in these models, they remain our best available tool for constraining non-aviation-related high cloud changes.

### Sensitivity to assumptions of cirrus overlap

Our comparison between observed and simulated cirrus responses to changes in aviation will depend on the amount of simulated contrail cirrus which is assumed to contribute to an increase in cirrus cover. As described in Sec. 3.2, we have accounted for overlap with natural cirrus using the fraction of contrail cirrus which contributes to an increase in *total* cloud cover, taken from BB16's Fig. 6b. This value will by definition be less than or equal to the fraction of contrail cirrus contributing to an increase in *cirrus* cloud cover, since the latter also allows for contrail cirrus which overlays low cloud. Using a low estimate for the 2006 simulated contrail cirrus results in a conservative estimate for the discrepancy between observed and simulated cirrus changes, and inflates the estimated value of $c_a$.

As a sensitivity test, we replace the above scale factor by $(1-\bar{c})$, where $\bar{c}$ is the 2000-2020 mean total cirrus fraction in each grid cell. This factor describes the typical fraction of each grid cell which is cirrus-free, such that the addition of contrail cirrus would increase total cirrus cover. However, contrail cirrus is more likely to form in regions which already contain natural cirrus than in regions which do not, since natural and contrail cirrus require similar synoptic conditions for formation. The factor $(1-\bar{c})$ is therefore an overestimate for the amount of detectable contrail cirrus in each grid cell, and will artificially suppress our estimate of $c_a$. Using MODIS-mean cirrus, our results are $c_a = 0.12\,(-0.06,\, 0.35)$ and $c_a = 0.18\,(-0.12,\, 0.47)$ for the Global and NAm-Eur domains respectively. Compared to our reference values of $c_a = 0.21\,(-0.09,\, 0.61)$ and $c_a = 0.30\,(-0.19,\, 0.79)$, it is clear that the choice of scale factor does not materially change our conclusions.

### 2.A.4 Deriving a quantitative estimate for the ERF from AIC

A detailed assessment of the radiative impact of AIC is beyond the scope of this paper, but we present a first estimate here based on several simplifying assumptions.

Our work looks exclusively at changes in cirrus extent. ERF depends also on the cirrus' optical thickness Kärcher (2018); Burkhardt and Kärcher (2011) and on what surface the cirrus overlays Yang et al. (2010). Optical thickness is in turn a function of ice crystal properties (shape, size, and number) and of ambient conditions (e.g. temperature, humidity, wind shear) Kärcher et al. (2009); Yang et al. (2010); Bock and Burkhardt (2016a); Kärcher et al. (2021). The net effect of these properties may not be independent of cirrus coverage.

If we assumed that the ERF from AIC *was* linearly dependent on AIC coverage, then our observations would imply

$$\mathrm{ERF}_{2006,\,\tau>0.05,\,\mathrm{obs}} = c_a \times \mathrm{ERF}_{2006,\,\tau>0.05,\,\mathrm{BB16}} \tag{2.A.2}$$

where $\mathrm{ERF}_{2006,\,\tau>0.05,\,\mathrm{obs}}$ is the observational estimate for the 2006 ERF contribution from AIC with optical depths $\tau > 0.05$ and $\mathrm{ERF}_{2006,\,\tau>0.05,\,\mathrm{BB16}}$ is the estimate of this quantity predicted by BB16.

However, we are interested in an ERF estimate for all AIC, not only that with $\tau > 0.05$, and for a year more recent than 2006. Furthermore, to enable robust comparison with other literature sources we will need to account for biases introduced by choices of input and methodology as described in L21.

The first condition is readily addressed by making the assumption that all AIC, regardless of optical depth, obeys the same scaling between aviation intensity and coverage. Our calculated value of $c_a$ would therefore apply to the total population of AIC, allowing us to write

$$\mathrm{ERF}_{2006,\,\mathrm{obs}} = c_a \times \mathrm{ERF}_{2006,\,\mathrm{BB16}} \tag{2.A.3}$$

To facilitate comparison with the current literature best estimate, and to scale our results to a 2018 ERF, we can simply calculate

$$\mathrm{ERF}_{2018,\,\mathrm{obs}} = c_a \times \mathrm{ERF}_{2018,\,\mathrm{BB16}^*} \tag{2.A.4}$$

where $\mathrm{ERF}_{2018,\,\mathrm{BB16}^*}$ is the value of ERF for 2018 obtained in L21 by first calibrating the BB16 RF for 2006 to a standardized set of assumptions and inputs, then converting it from an RF to an ERF, and finally scaling the result to account for the increase in air traffic from 2006 to 2018. This process is described in detail in the appendices and supplementary material of L21; the value of $\mathrm{ERF}_{2018,\,\mathrm{BB16}^*} = 37\,\mathrm{mWm}^{-2}$ is available in the supplement.

With these simplifying assumptions our MODIS-mean, global-domain observations therefore imply an effective radiative forcing from AIC of $8\,(-3,\,22)\,\mathrm{mWm}^{-2}$ for the year 2018, which is substantially lower than the L21 multimodel best estimate of $57\,(17,\,98)\,\mathrm{mWm}^{-2}$. Reassuringly, however, the uncertainty ranges of these two estimates do overlap. We emphasize that this is a highly simplified approximation of a highly nuanced calculation, which warrants a more detailed analysis.

### 2.A.5 Tabulation of regression results

This section contains Figure 2.A.5 showing an equivalent analysis to that presented in Figure 2.3 but calculated using the annual number of flights instead of total kilometres flown to represent aviation intensity, and Table 2.A.1 summarizing the regression coefficient $c_a$ for all combinations of spatial domain, cirrus dataset, and aviation dataset.

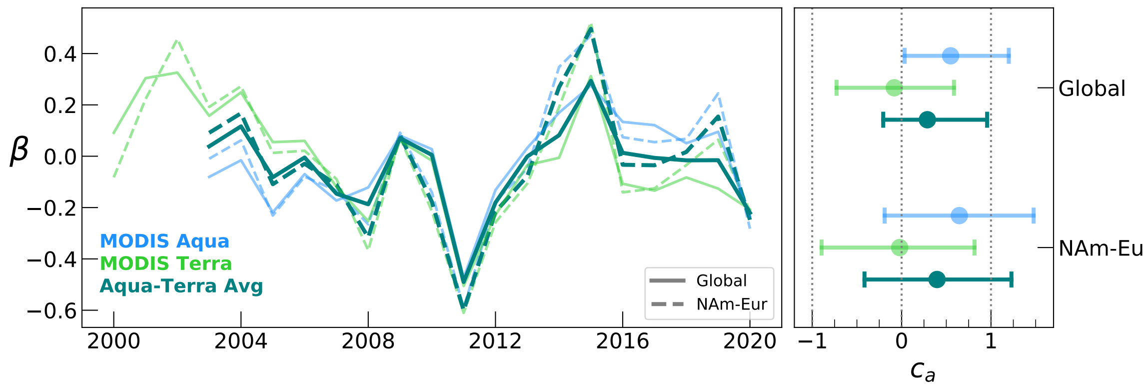


Figure 2.A.5: As Figure 2.3, but with aviation characterized by the annual number of flights instead of total kilometres flown. This quantity is less physically relevant for AIC formation but more easily compared with available data on month-by-month aviation changes through 2020 (Figure 2.2). Compared with our remain results, the confidence intervals on $c_a$ are larger in all cases, and some now intersect 1 (i.e., results are consistent with the simulated magnitude of response). The numerical values of $c_a$ for all combinations of aviation dataset, cirrus dataset, and spatial domain are summarized in Table 2.A.1. Flight numbers for 2019-2020 are taken from publicly available FlightRadar24 data on commercial aviation FlightRadar24 (2021). Those for 2000-2018 are taken from A4A and scaled by the ratio of the two datasets in 2019 to account for the subset of commercial aviation not included in A4A records.

Table 2.A.1: Regression coefficient $c_a$ for all combinations of spatial domain (Global or NAm-Eur), cirrus dataset (observations from Aqua, Terra, or their average), and aviation dataset (flight kms as shown in Figure 2.3, or flight numbers as shown in Figure 2.A.5). Uncertainty ranges indicate bootstrapped 5-95% confidence intervals.

| Domain | Satellite | $c_a$, flight kms | $c_a$, flight numbers |
|---|---|---|---|
| Global | Aqua | 0.36 (0.05, 0.75) | 0.55 (0.03, 1.21) |
| | Terra | 0.03 (-0.37, 0.43) | 0.08 (-0.73, 0.59) |
| | Average | 0.21 (-0.09, 0.61) | 0.29 (-0.21, 0.96) |
| NAm-Eur | Aqua | 0.44 (-0.06, 0.93) | 0.65 (-0.18, 1.47) |
| | Terra | 0.10 (-0.44, 0.62) | -0.02 (-0.89, 0.82) |
| | Average | 0.30 (-0.19, 0.79) | 0.40 (-0.41, 1.23) |

# Chapter 3

# Aerosol Emissions during COVID-19

The Spring 2020 COVID-19 lockdowns led to a rapid reduction in aerosol and aerosol precursor emissions. These emission reductions provide a unique opportunity for model evaluation, and to assess the potential efficacy of future emission control measures. We investigate changes in observed regional aerosol optical depth (AOD) during the COVID-19 lockdowns, and use these observed anomalies to evaluate Earth system model simulations forced with COVID-19-like reductions in aerosols and greenhouse gases. Most anthropogenic source regions do not exhibit statistically significant changes in satellite retrievals of total or dust-subtracted AOD, despite the dramatic economic and lifestyle changes associated with the pandemic. Of the regions considered, only India exhibits an AOD anomaly that exceeds internal variability. Earth system models reproduce the observed responses reasonably well over India but initially appear to overestimate the magnitude of response in East China and when averaging over the Northern Hemisphere (0°N-70°N) as a whole. We conduct a series of sensitivity tests to systematically assess the contributions of internal variability, model input uncertainty, and observational sampling to the aerosol signal, and demonstrate that the discrepancies between observed and simulated AOD can be partially resolved through the use of an updated emissions inventory. The discrepancies can also be explained in part by characteristics of the observational datasets. Overall our results suggest that current Earth system models have potential to accurately capture the effects of future emission reductions.

The contents of this chapter appeared in Atmospheric Chemistry and Physics as *How well do Earth system models reproduce the observed aerosol response to rapid emission reductions? A COVID-19 case study* (Digby et al., 2024).

## 3.1 Introduction

The emergence and rapid spread of COVID-19 in early 2020 had profound impacts on both individual behaviour and the large-scale economy. Following the detection of the first cases in Wuhan, China in December 2019 (World Health Organization, 2020a), and its categorization as a global pandemic in March 2020 (World Health Organization, 2020b), countries around the world began to implement a range of public health measures to limit the virus' spread. In many regions these included restrictions on public and private gatherings, domestic or international travel bans, curfews, and in some cases, stay-at-home orders.

One consequence of these dramatic economic and lifestyle changes was a rapid reduction in the emissions of aerosols and their precursors. This reduction has been widely reported on, with the majority of studies falling into one of two categories.

The first, more extensive category consists of studies investigating changes in local (predominantly urban) air quality during the pandemic. As summarized by Gkatzelis et al. (2021), more than 200 papers on air quality changes were published in the first 7 months of 2020 alone. These papers reported substantial reductions in major pollutants including $NO_2$, $NO_x$, $O_3$, $SO_2$, and particulate matter in cities around the globe. The spread in estimates varied dramatically within and between geographic regions. The intra-regional spread can be attributed in part to city- or nation-scale heterogeneity and in part to methodological differences between studies. Notably, Gkatzelis et al. (2021) found that approximately two thirds of these works did not account for interannual or in some cases even seasonal variability in aerosol levels; the importance of accounting for meteorological changes is emphasized in several recent works (Deroubaix et al., 2021; Diamond and Wood, 2020; Goldberg et al., 2020; Ordóñez et al., 2020). There have, however, been many rigorous studies of air quality changes (Chang et al., 2020; Jia et al., 2021; Ordóñez et al., 2020; Siciliano et al., 2020; Venter et al., 2020; Al-Abadleh et al., 2021; Liu et al., 2021; Sokhi et al., 2021; Wyche et al., 2021; Zhou et al., 2022; Kong et al., 2023).

The second category of COVID-19-based aerosol studies consists of model simulations of regional or global climate responses to this reduction in emissions. These studies, which include both idealized and proxy-based emission reduction scenarios for 2020, have reported weak to negligible climate responses, with top of atmosphere radiation changes comparable to interannual variability and changes in temperature or precipitation unlikely to be detectable in observations (Fasullo et al., 2021; Fiedler et al., 2021; Forster et al., 2020; Fyfe et al., 2021; Gettelman et al., 2021; Jones et al., 2021; Weber et al., 2020). These studies generally report reductions in zonally averaged aerosol optical depth (AOD) at ~30°N in March 2020, and small or non-detectable changes in global aerosol optical depth. The magnitudes of these reductions are model-dependent and in some cases only detectable in the ensemble mean.

Few studies have bridged these categories, comparing the observed and simulated responses to the COVID-19 aerosol emission reductions. Among those studies that have incorporated both observations and simulations, the simulations have generally been used to help explain the observed changes by predicting control conditions in the absence of a COVID-19 perturbation (Goldberg et al., 2020; Griffin et al., 2020; Le et al., 2020; Hammer et al., 2021; Huang et al., 2021; Mashayekhi et al., 2021; Li et al., 2022). No studies have yet leveraged the observed aerosol response to the COVID-19 lockdowns for model evaluation purposes.

Reliable model simulations of the direct and indirect responses to a reduction in aerosol emissions are crucial for policy development. The Shared Socioeconomic Pathways (SSPs; Riahi et al., 2017) and Representative Concentration Pathways (RCPs; van Vuuren et al., 2011; Lamarque et al., 2011) all include a reduction in aerosol emissions over the coming decades. Because aerosols are often co-emitted with greenhouse gases (GHGs), some of these reductions will be the result of targeted air quality legislation and some will be a side effect of climate policies. Depending on the sectors targeted by these policy measures, and the resulting cocktail of aerosol species that are affected, such reductions may lead to climate co-benefits or climate penalties (von Salzen et al., 2022). These uncertainties are compounded by the fact that aerosol-climate interactions remain one of the largest sources of uncertainty in future climate projections (Szopa et al., 2021). Predictions of future air quality changes are also highly uncertain (Szopa et al., 2021). The opportunity for model evaluation afforded by the COVID-19 pandemic is thus invaluable. In particular, the COVID-19 pandemic demonstrates the impacts of a rapid emission reduction, whereas previous observational constraints have been based on slower (e.g. decadal) emission trends (e.g. Ramachandran et al., 2022; Lund et al., 2023). There are both practical and scientific motivations for studying a rapid emission reduction. On the practical front, a short-but-strong signal is easier to disentangle from other sources of variability; we have continuous satellite observations that cover the entire study period; and the period is short enough the instrument drift is unlikely to be a concern. Scientifically, model simulations indicate that the presence and severity of potential climate penalties, including changes in mean and extreme temperatures and precipitation, may be proportional to the rate at which emissions are reduced (Acosta Navarro et al., 2017; Hienola et al., 2018; Samset et al., 2020; Shindell and Smith, 2019; Shindell et al., 2012; Sillmann et al., 2013). Although we do not investigate the climate response to COVID-19 in this work, understanding the aerosol response itself is an important first step.

Both the air quality and climate impacts of a reduction in emissions depend on the response of atmospheric aerosol concentrations to emission changes, which is in general a complex and nonlinear dependence (Szopa et al., 2021; Kroll et al., 2020). The climate effect further depends on the resulting changes in scattering and absorption, which can be quantified in terms of aerosol optical depth. In this work we consider changes in AOD, rather than concentration, since it is more readily available from both model simulations and remotely sensed observations.

The models used in this work are taken from the COVID-19 Model Intercomparison Project (CovidMIP; Jones et al., 2021), which was developed to investigate the effects of a COVID-19-like reduction in aerosols and greenhouse gases. Although Jones et al. (2021) present an initial analysis of changes in aerosol optical depth, their primary foci were the radiative and climatic responses to the COVID-19 perturbation, and the drivers of the simulated aerosol changes were not investigated. Our analysis provides the first detailed investigation of aerosol changes in the CovidMIP models, as well as the first comparison between observed and CovidMIP-simulated changes.

In order to disentangle the signal of COVID-19 from other sources of AOD variability and model-observation discrepancy, we first derive a basic analytic framework consisting of three assessment metrics, and then systematically assess the influence of potential confounding factors on our results. This assessment is done by either correcting for these factors directly or conducting sensitivity tests to quantify their impacts on our metrics. The factors we assess are discussed in Section 3.2. Our datasets are described in Section 3.3 and the metrics by which we assess them are described in Section 3.4. Section 3.5.1 presents the results of our basic analysis, and Section 3.5.2 describes our sensitivity tests. The implications of these results are discussed in Section 3.6.

## 3.2 Components of the AOD signal

Disentangling the signal of COVID-19 emission reductions from other sources of variability in an observed AOD field is a complex and nuanced task. Conducting robust comparisons between observed and simulated responses is yet more involved. We begin by highlighting the major considerations that need to be addressed in an analysis of this type: sources of AOD variability; factors that contribute to discrepancies between simulated and observed AOD fields, no matter the quality of the atmospheric model or satellite retrieval; and finally, the impacts of observational uncertainty.

### 3.2.1 AOD variability

Aerosol optical depth is determined by natural and anthropogenic emissions, the chemical production of secondary aerosol species in the atmosphere, transport, and microphysical processes. All of these processes are affected to various degrees by meteorological conditions. Collectively, physical and chemical processes determine not only the distribution of atmospheric aerosols, but the optical depth that results from this aerosol burden.

Because these processes are highly interdependent, we simplify matters by grouping the drivers of AOD variability into three categories: variability in anthropogenic emissions, natural emissions, and meteorological conditions. Anthropogenic emissions vary over different timescales, including diurnal (e.g. weekday/weekend cycles of traffic emissions), seasonal (e.g. with changing heating/cooling requirements) and annual to decadal (e.g. due to socioeconomic changes and direct legislation). Natural emissions also differ substantially from one year to the next: mineral dust and sea salt emissions are strongly influenced by surface wind stress, and biomass burning emissions vary with storm activity (wildfire ignition by lightning) and aridity (soil moisture content, fuel availability). Once aerosols are in the atmosphere, their transport is affected by atmospheric circulation, and their removal by precipitation and dry deposition depends on hydrometeorological conditions, atmospheric stability, and winds.

The above processes determine aerosol burden. The AOD that results from this burden depends on the intrinsic characteristics of the aerosol (e.g. refractive index and particle morphology, which can change in response to variations in emission source, and whether components are internally or externally mixed) and on the ambient conditions (e.g. via hygroscopic growth). Because these microphysical characteristics ultimately depend on the changes in emission and meteorological processes listed above, we will consider them under the umbrella of those categories.

The observed AOD anomaly from Spring 2020 will combine these different factors, with the reduction in anthropogenic emissions due to COVID-19 making up an unknown fraction of the total. Our analysis must therefore account for these different sources of variability when assessing both the observed and simulated AOD signals. In the following sections, we describe first the differences that would be expected even if both models and observations were perfectly accurate, and then the impacts of observational uncertainty.

### 3.2.2 Differences between observed and simulated AOD in the absence of model error or observational uncertainty

Even given a hypothetical model that perfectly simulated atmospheric aerosol processes, and perfectly accurate satellite retrievals, differences would still arise between the observed and simulated AOD fields. These differences can be grouped into three main categories. First, a freely running model would produce a different realization of meteorological conditions than occurred in the real world, and so aerosols would be subject to different emission, transport, and depositional processes. Second, any errors in the model inputs (e.g. in the size of perturbation applied to represent COVID-19) would translate into biased simulations. Finally, the simulated and observed AODs would be recorded with different spatiotemporal sampling. Before any differences between the observed and simulated responses to COVID-19 can be attributed to model biases, then, these factors must be accounted for. (We discuss the role of observational uncertainty separately, in Section 3.2.3.)

We address AOD differences stemming from the differences in the observed and simulated realizations of the climate system in two ways. First, we compare AOD anomalies during COVID-19 to the scale of internal variability, both by looking at observed interannual variability over the reference period and by running ensembles of simulations to sample the models' internal variability. If an AOD anomaly is well outside of typical interannual variability, then it is likely to have been caused by more than just meteorological conditions. Equivalently, if the observed AOD change is well outside of typical interannual variability but the simulated AOD change is not, or vice versa, then the difference between these two responses is unlikely to be caused by differences in the simulated and observed meteorological conditions. Second, we can run simulations nudged to meteorological fields taken from reanalyses to constrain the simulated meteorological realization to be close to observations.

AOD differences arising from biases in the model input can be assessed by running simulations where the input emission inventories are varied. In this work we assess the sensitivity of our results to uncertainties in both the reference and COVID-19-perturbed aerosol emissions in one model, and discuss the extension of these results to the other models in our sample.

AOD differences can also arise from discrepancies between the spatial and temporal sampling of the different datasets. A simulated monthly-mean AOD value is the mean over all times of day and night, in all weather conditions. A satellite's monthly-mean AOD retrieval is the mean of AOD values collected at the satellite's particular overpass time, in clear-sky conditions (if it is a passive sensor), and at times when the retrieval was successful and not prevented by a myriad of potential limitations such as sun glint or complex terrain. We conduct a detailed assessment of these sampling differences (Appendix 3.A.1) and demonstrate that in our data, the discrepancies caused by sampling differences are much smaller than those due to systematic biases between observed data products.

### 3.2.3 Observational uncertainty

The three categories of difference discussed in Section 3.2.2 would occur even if both the model and satellite were perfect. However, satellite retrievals are characterized by both systematic and random measurement errors (Povey and Grainger, 2015; Sayer et al., 2020).

Estimation of retrieval biases and uncertainties is further complicated when considering quantities averaged in space and time. The degree to which individual retrieval errors are reduced by averaging depends on the relative contributions of random and systematic components, which will vary both spatially and temporally (e.g. Povey and Grainger, 2015; Young et al., 2018). Even if the uncertainty was due entirely to random error, the effects of averaging would not be straightforward, since there is no reason to expect that the retrievals would be independent or identically distributed. Further complication arises when considering dust-subtracted aerosol optical depths, since the task of discriminating between aerosol species is separate from the determination of total AOD (Omar et al., 2009; Gkikas et al., 2021; Song et al., 2021), and it is not obvious how the respective uncertainties would be propagated even if they could be individually constrained. Given these limitations, spatial averages of remotely-sensed AOD are generally published without quantitative uncertainty estimates.

Considering the above complications, we do not provide uncertainty estimates for individual observational measurements. Instead we use the spread between observational products as an overall estimate of the uncertainty in the true AOD. As Appendix 3.A.1 demonstrates, this spread is due primarily to systematic biases between products and not to differences in their spatiotemporal sampling. As Appendix 3.A.1 further demonstrates, however, agreement between datasets is substantially improved when data are expressed as anomalies rather than absolute values.

## 3.3 Datasets

### 3.3.1 Model simulations

The COVID-19 Model Intercomparison Project (CovidMIP; Jones et al., 2021) was developed to investigate the effects of a COVID-19-like reduction in aerosols and greenhouse gases. It includes contributions from twelve Earth system models, all of which had previously participated in the 6th Phase of the Coupled Model Intercomparison Project (CMIP6; Eyring et al., 2016).

The CovidMIP scenarios, detailed in (Forster et al., 2020), include the control scenario, a “two-year blip” experiment, and three long-term recovery scenarios. The two-year blip, which is the focus of this work, estimates aerosol and greenhouse gas emission reductions from mobility data (Forster et al., 2020; Le Quéré et al., 2020) for the period of Jan-June 2020; 66% of the June restrictions are then assumed to persist until the end of 2021, after which emissions recover linearly to the baseline. We limit our analysis to Jan-June 2020, for which the simulated emissions changes are based on observational proxies rather than projections. Further details on the calculation of these reductions, and an assessment of the sensitivity of our results to uncertainties in their estimation, are presented in Section 3.5.2.

The control scenario used in CovidMIP is SSP2-4.5 (Riahi et al., 2017), a middle-of-the-road scenario developed for the Scenario Model Intercomparison Project (ScenarioMIP, O’Neill et al., 2016) as part of CMIP6. The implications of this choice of reference are explored in Section 3.5.2. Throughout this work, SSP2-4.5 is stylized *ssp245* when we are referring to a model simulation experiment, and written

Table 3.3.1: CovidMIP models used in this chapter (in alphabetical order). "Published *od550dust*?" column indicates whether mineral dust optical depths were available on ESGF for each model.

| Model | Realizations | Published *od550dust*? | References |
|---|---|---|---|
| ACCESS-ESM1.5 | 30 | no | Ziehn et al. (2020) |
| CanESM5.0 | 50 | yes | Swart et al. (2019) |
| MIROC-ES2L | 30 | yes | Hajima et al. (2020) |
| MRI-ESM2.0 | 10 | yes | Yukimoto et al. (2019) |
| NorESM2-LM | 10 | yes | Seland et al. (2020) |
| UKESM1-0-LL | 16 | no | Sellar et al. (2019) |

as SSP2-4.5 when we are discussing the scenario more generally. The COVID-19-perturbed experiment is referred to as *ssp245-covid*. We additionally use the terms *reference*, *control*, and *perturbed* to refer to the 2015-2019 *ssp245*, 2020 *ssp245*, and 2020 *ssp245-covid* simulations respectively.

We use only those CovidMIP models for which aerosol concentrations were not prescribed, and for which data were available on the Earth System Grid Federation (ESGF; `https://esgf-node.llnl.gov/search/cmip6/`). For the control experiment *ssp245*, this requirement applies to the reference period (2015-2019) as well as to the 2020 experiment period. In addition, much of our analysis utilizes dust-subtracted optical depth, which is calculated by subtracting the aerosol optical depth due to dust (CMIP variable name *od550dust*) from the total AOD at 550nm (*od550aer*); however, *od550dust* is not published for all models. In total, four CovidMIP models met the data availability requirements for both total and dust aerosol optical depths, and an additional two models met the above criteria for total aerosol optical depth only. These six models, summarized in Table 3.3.1, sample the range of global AOD anomalies and climatic responses simulated by the full CovidMIP suite (Jones et al., 2021).

The most obvious outlier among these models is CanESM5.0, which exhibits an exceptionally large ensemble spread in AOD. This variability is caused by the production of spurious tropospheric dust storms, which have been attributed to errors in the tuning of mineral dust tracer parameters (Sigmond et al., 2023). Fortunately, only the dust tracers were affected, and the dust-subtracted AOD is consistent with that simulated by other CMIP6 models. This issue has since been corrected and will not be present in CanESM5.1. For the purposes of this analysis, CanESM5.0 is excluded from some analyses of total AOD.

Throughout this analysis, model results are described in terms of an ensemble median and 5th-to-95th percentile range. When results are presented as spatially averaged timeseries, the percentile range is calculated across the ensemble of spatially-averaged values.

### 3.3.2 Remotely sensed observations

This work incorporates remotely sensed observations of both total and mineral dust aerosol optical depths. The datasets used in our analysis are summarized in Table 3.3.2 and described in Sections 3.3.2 and 3.3.2 respectively.

| Dataset Name | AOD | DSAOD | Instrument | Satellite | Type | Conditions | EOT | References and Notes |
|---|---|---|---|---|---|---|---|---|
| MODIS-Aqua | x | - | MODIS | Aqua | passive | cloud-free | 1:30pm | (King et al., 2013; Platnick et al., 2017) |
| MODIS-Aqua-MIDAS | - | x | MODIS | Aqua | passive | cloud-free | 1:30pm | AOD from MODIS-Aqua; DOD from MIDAS (see Section 3.3.2; Gkikas et al., 2021) |
| MISR | x | - | MISR | Terra | passive | cloud-free | 10:30am | (Diner et al., 1998) |
| CALIOP-AllSky-Night | x | x | CALIOP | CALIPSO | active | all-sky | 1:30am* | (Winker et al., 2009) (CALIPSO official product) |
| ACROS-C | x | x | CALIOP | CALIPSO | active | cloud-free | 1:30am* | (Song et al., 2021; Yu et al., 2015) (Developed by ACROS group) |

Table 3.3.2: Observational datasets used in this chapter. Columns "AOD" and "DSAOD" indicate whether this dataset is used in our analyses of total and dust-subtracted optical depths respectively. "EOT:" Equatorial overpass time (local time). *: orbit changed in Sept 2018.

Satellite observations of total AOD are taken from the Moderate Resolution Imaging Spectroradiometer (MODIS; King et al., 2013; Platnick et al., 2017), Multi-angle Spectral Radiometer (MISR; Diner et al., 1998), and the Cloud-Aerosol Lidar with Orthogonal Polarization (CALIOP; Winker et al., 2009). Level 3 gridded, monthly mean products are used from all three instruments. We additionally include an AOD estimate derived from CALIOP data by the Aerosol, Cloud, Radiation - Observation and Simulation (ACROS) group at the University of Maryland, Baltimore County (ACROS-C; Song et al., 2021), described further in Section 3.3.2.

There are two MODIS instruments, mounted on the Aqua and Terra satellites. We use MODIS Aqua data in our main analysis, due to an identified high bias in the MODIS Terra calibration (Levy et al., 2018), but compare with MODIS Terra data in Appendix 3.A.1. The MISR instrument is mounted on Terra, and observes a smaller swath within the footprint of MODIS-Terra. As passive sensors, both MODIS and MISR observe only during the day and in cloud-free conditions. In contrast, CALIOP – onboard the Cloud-Aerosol Lidar and Infrared Pathfinder Satellite Observation (CALIPSO) platform – is an active lidar sensor and so can take measurements during the day or night. Because the absence of a solar background means that CALIOP's AOD has lower uncertainties at night (Young et al., 2018), we use the all-sky nighttime product in our main analysis. This product is compared with the cloud-free daytime product in Appendix 3.A.1 to help quantify the effects of sampling differences between different datasets. Terra and Aqua have daytime equatorial overpass times of 10:30am and 1:30pm respectively. CALIPSO initially orbited in the same satellite constellation as Aqua, but in September 2018, moved to a lower orbit to maintain coincident measurements with CloudSat (ASDC, 2018).

AOD retrieved from MODIS is generally biased high relative to ground-based AERONET measurements (Wei et al., 2020; Levy et al., 2018), while AOD from MISR and CALIOP is generally biased low (Kahn et al., 2009; Schuster et al., 2012); AERONET is widely considered the gold standard for the evaluation of satellite AOD retrievals, despite limitations in its spatial representativity (Schutgens et al., 2020), because AERONET uncertainties are substantially lower than those from satellites. MODIS is also generally biased high, and MISR and CALIOP biased low, when comparing with other remotely sensed and reanalysis datasets that are available for shorter periods of time (Vogel et al., 2022). As demonstrated in Appendix 3.A.1, the spread in AOD estimates retrieved from these three datasets is dominated by systematic biases and not by sampling differences. Thus the spread between these datasets, which spans the range of AOD available from ground- and space-based instruments, provides a reasonable estimate of current observational uncertainty.

### Dust optical depth

Much of this analysis considers dust-subtracted aerosol optical depths. Neither MODIS nor MISR produce a dust-specific product. However, other research groups have combined MODIS retrievals with auxiliary data to derive estimates of dust optical depth. In this work we use the ModIs Dust AeroSol (MIDAS; Gkikas et al., 2021) product, which combines total AOD from MODIS Aqua with an estimate of the dust-to-total ratio from the MERRA-2 reanalysis, to estimate the dust optical depth from MODIS Aqua. MIDAS also publishes a total optical depth estimate, which applies additional filters to the MODIS dataset. Our results are insensitive to the choice of MIDAS or MODIS total aerosol optical depth; we use MODIS Aqua in the analysis presented here.

CALIOP determines the composition of aerosol layers using a combination of retrieval information (depolarization ratio, integrated attenuated backscatter, layer height) and information about the underlying surface (Omar et al., 2009; Kim et al., 2018). The aerosol subtyping algorithm identifies seven tropospheric aerosol types, including dust, polluted dust, and dusty marine. However, these are separate classifications (e.g. "dust" refers only to clean dust, whereas "polluted dust" refers to dust mixed with urban pollution or biomass burning smoke) and there is no estimate of the total dust optical depth (Omar et al., 2009). We present results using the "dust" product ($AOD\_Mean\_Dust$) but acknowledge that it does not capture the entire contribution of dust to AOD, particularly in heavily polluted regions.

The ACROS-C dataset is included in our analysis to provide a secondary estimate of dust optical depth from CALIOP retrievals. ACROS-C uses the lidar depolarization ratio to distinguish dust by shape (Yu et al., 2015; Song et al., 2021). The ACROS group also publishes a MODIS-based dust optical depth product, but this dataset is not available for 2020 so is excluded from our analysis.

## 3.4 Methods: quantifying the impacts of COVID-19

In the Introduction, we presented two motivating questions for this work: First, do observations exhibit a detectable response to the COVID-19 emissions reductions?

And second, how well do current models reproduce this response? Here we present the quantitative metrics by which these questions are addressed. Throughout, anomalies are calculated relative to the 2015-2019 March-April-May (MAM) mean.

For the models, we consider a COVID-19 response to be "statistically significant" if there is a statistically significant difference between the control and COVID-19-perturbed ensemble means in 2020, based on a two-sided Students t-test. Because the only difference between the control and perturbed ensembles is the absence or presence of a COVID-19 perturbation, we can compare the ensembles directly and avoid the challenge of disentangling year-to-year changes in the underlying anthropogenic emissions from internal variability between realizations. Note, however, that this test is sensitive to ensemble size and that a larger ensemble will be more likely to yield a significant response.

Defining detectability for the observations is more challenging, because there is no "control observation" from which to estimate the AOD that would have been measured in 2020 had COVID-19 not occurred. It would not be sufficient to use the mean and variance calculated from the reference period as a control: using the mean would neglect the impacts of underlying trends in the emissions, and a five-year reference period is too short to provide a robust estimate of the variance. Instead we borrow an approach from the field of detection and attribution (Eyring et al., 2021) and compare the ensemble of observed anomalies to a multimodel control ensemble (MMEc) constructed by randomly drawing an equal number of control simulation anomalies from each model. This comparison relies upon two assumptions: that the models realistically simulate internal variability, and that they capture any underlying trends in AOD over the reference period. These assumptions determine the spread and best estimate, respectively, predicted by the MMEc.

We assess the first of these assumptions by comparing observed and simulated variability over the reference period in our regions of interest. We calculate the variance of the region-mean AOD field over the reference period for each simulated ensemble member, the MMEc, and the observational datasets, and compare the spread in these estimates of variance. Although individual models may over- or underestimate the interannual variability in some regions, we cannot reject the null hypothesis that the MMEc and observations have the same interannual variability, based on a two-sided Welch's t-test. The only exception is for India, where the MMEc overestimates the variability in total and dust-subtracted aerosol optical depth; as a result, estimates of observational detectability will be conservative (i.e., anomalies are less likely to be found to be statistically significant). In a similar analysis of the variability over a longer baseline (2007-2019), using a subset of models for which these data were available, the total-AOD variability of the MMEc is consistent with that of the observations in all four regions.

Having determined that it is reasonable to treat the simulations and observations as having similar internal variability, we derive a statistical test with which to compare observed and simulated AOD anomalies. We use a modified Welch's t-test of the form

$$t = \frac{\bar{X}_1 - \bar{X}_2}{s_{\bar{\Delta}}} \qquad \text{where} \qquad s_{\bar{\Delta}} = \sqrt{\frac{s_1^2}{n_1} + \frac{s_2^2}{n_2}} \tag{3.4.1}$$

where $s_1^2$ and $s_2^2$ are unbiased estimators of the variance in the simulations and observations respectively. As outlined above we assume that the observations and simulations have the same variance due to internal variability, $s_1^2$, which we calculate from the simulated ensemble spread in the year under consideration. The observations additionally have a contribution to their variance due to observational uncertainty, $s_0^2$, calculated from the spread in observational estimates in that year. The total variance in the observations is then $s_2^2 = s_0^2 + s_1^2$. We use this t-test to determine whether the observed anomaly is statistically significant, through comparison with the MMEc, and to determine whether the individual models' simulated anomalies are consistent with the observed anomaly, by comparison with the control and perturbed experiments in turn. We present results for t-tests performed on region-mean values; using spatially-resolved comparisons adds little information and does not change our results.

The second assumption, that the models capture any trends in AOD over the reference period, may break down in some geographic regions. However, although some regions have nonstationary anthropogenic emissions over the 2015-2019 reference period, we do not detrend our datasets. With only a five-year baseline, the observed timeseries is heavily influenced by interannual variability which masks underlying trends in anthropogenic emission changes. With a longer baseline, the assumption of a linear trend would be unfounded; China, for example, had steadily-increasing anthropogenic aerosol emissions until their implementation of the Action Plan on the Prevention and Control of Air Pollution in 2013, since which emissions have been rapidly declining (Zheng et al., 2018). Given these limitations we work with anomalies calculated relative to the 2015-2019 mean but discuss the impacts of underlying trends on our results throughout.

## 3.5 Results

### 3.5.1 Comparison between observations and CovidMIP models

We begin with an assessment of the changes in total and dust-subtracted AOD during the COVID-19 lockdown periods. Four regions are selected for analysis: the Northern Hemisphere (restricted to 0-70°N), and three major anthropogenic aerosol source regions, namely East China (100-122°E, 20-40°N), India (70-90°E, 5-30°N), and Europe (10°W-35°E, 35-70°N). East China and India were defined following Wang et al. (2021), with the India domain extended south to include all of Sri Lanka, and the European domain was selected to maximize (minimize) the land (ocean) enclosed. The Northern Hemisphere domain was restricted to 0-70°N to enable comparison with observations. The boundaries of these regions are illustrated in Figure 3.A.7.

The timing of the strictest lockdowns, as defined by the Oxford Stringency Index (Hale et al., 2021), varies between these regions but occurs for all between March and May of 2020. To aid in inter-region comparisons, and to increase the signal-to-noise ratio over what would be obtained from analyses of single months, we evaluate the MAM-mean anomaly in all four regions.

#### Response of total AOD to the COVID-19 emission reductions

The observed and simulated total AOD anomalies over 2015-2020 are summarized in Figure 3.5.1. Of the four regions assessed, only India exhibits a statistically significant observed response to the COVID-19 lockdowns. In East China and Europe, the observed anomalies are clearly within the range of interannual variability over the reference period. In the Northern Hemisphere, two of the four observational products suggest anomalously low AOD compared to the preceding 5 years, although this excursion is less clearly anomalous when considering the apparent negative trend in AOD; the other two data sources do not show particularly large anomalies.

Simulated results vary from model to model. In the Northern Hemisphere, two of the six models exhibit statistically significant differences between the control and perturbed anomalies, but in most cases, both the control and perturbed ensembles are consistent with the observed anomalies in this region. In East China, four of the six models exhibit a statistically significant COVID-19-perturbed anomaly, which in general appears to be over-estimated: in these models, there is a statistically sig-

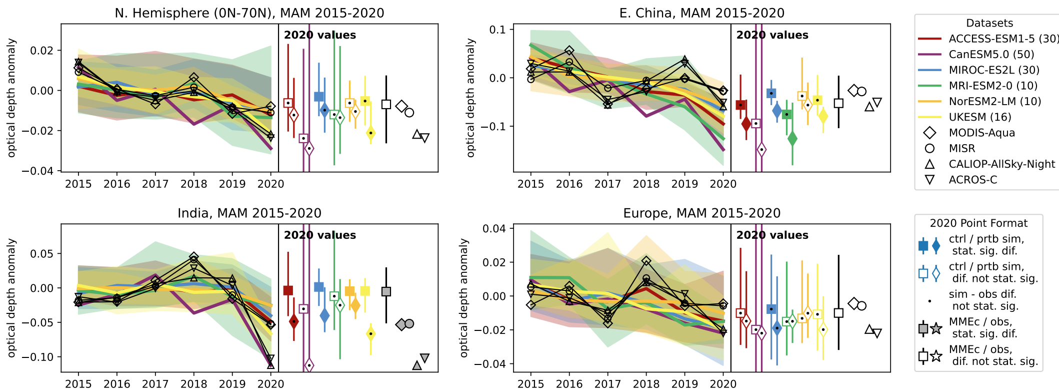


Figure 3.5.1: MAM-mean AOD anomalies in CovidMIP models (colour, ensemble sizes noted in parentheses) and in remotely-sensed observations (black), in the Northern Hemisphere and in 3 major source regions. The left-hand portion of each panel shows timeseries of AOD anomalies over 2015-2020, with datasets denoted as per the upper legend. For the simulations, lines and shaded envelopes indicate ensemble medians and 5th to 95th percentile ranges respectively. The right-hand portion of each panel plots the 2020 AOD values: two points for each model, corresponding to the control and COVID-19-perturbed simulations (square and diamond markers respectively, with error bars showing the 5-95% ensemble range), and one point for each observational data product (black outlines, no error bars). These points are formatted according to the results of our statistical comparisons, as summarized in the lower legend. In this legend, the blue-coloured and star-shaped markers represent simulated and observed datasets respectively, each of which is plotted with a different colour/marker as indicated in the upper legend. Model simulations that exhibit a statistically significant COVID-19 response (i.e., separation between control and perturbed ensembles) are plotted with filled symbols, and those that do not are plotted with open symbols. Black dots indicate simulated anomalies that are not significantly different from the ensemble of observed anomalies. The single, black-outlined square with error bars, plotted between the simulated and observed anomalies, shows the MMEc against which observations are compared. If there is statistically significant separation between the MMEc and observations (i.e., a detectable observed response), then both the MMEc and observations' markers have a solid fill. Note that the 4 panels have different vertical scales. Note also that because of the spuriously large AOD spread in CanESM5.0, only the ensemble median is shown in the timeseries; the 2020 ensemble ranges extend beyond the limits of the figure.

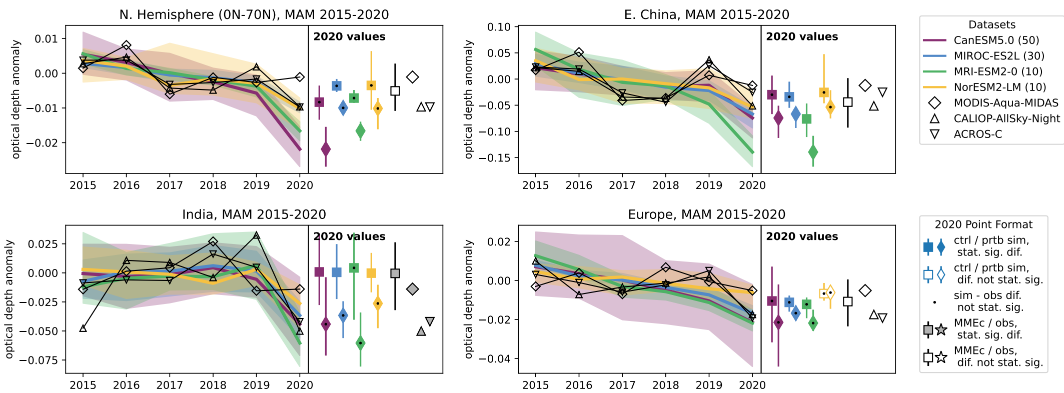


Figure 3.5.2: As Figure 3.5.1, but with the dust contribution removed from the optical depth. The ensemble spread is shown for CanESM5.0 here, unlike in Figure 3.5.1, since subtracting off the dust component removes the spuriously high AOD variability in this model.

nificant between the observations and the perturbed ensemble, but not between the observations and the control. In India, like East China, four of the six models simulate statistically significant separation between the control and perturbed ensembles. Unlike in East China, however, these responses are in good agreement with the observed anomalies: four of the perturbed ensembles are consistent with the magnitude of the observed ensemble, whereas only two of the control ensembles are. Finally, there is also good agreement between the observed and simulated anomalies in Europe: only one model shows a statistically significant perturbation, and in all models, both the control and perturbed ensembles are consistent with the observed anomalies.

The existence of some disagreement between the observed and simulated responses is not unexpected. As outlined in Section 3.2, the total-AOD signal is influenced by many factors beyond the changes in anthropogenic emissions. The impacts of these factors are assessed in the following sections.

**Response of dust-subtracted AOD to the COVID-19 emission reductions**

We next investigate the AOD signal when the contribution from mineral dust has been removed (dust-subtracted AOD, or DSAOD). In our regions of interest, the variability in total aerosol optical depth is dominated by the variability in mineral dust, which was not directly impacted by COVID-19 lockdowns. Its presence may thus substantially mask any anthropogenically-driven AOD changes. Although dust emission could have been indirectly affected via, e.g., changes in temperature or precipitation induced by $CO_2$ or aerosol changes during the COVID-19 lockdowns, we expect these effects to have been small; as described above, simulations suggest only weak climate responses to the COVID-19 emission changes.

Figure 3.5.2 reproduces Figure 3.5.1 but for DSAOD, showing results from the four CovidMIP models for which dust optical depths were available. As with the total AOD, an observed response is only detectable in India. Accounting for the role of dust improves model-observation agreement in this region, with all four models assessed exhibiting significant COVID-19 responses that agree with the magnitude of the observed anomaly. This improvement is partially due to the fact that the observed dust optical depth was anomalously low in 2020, as seen in our results and as reported elsewhere (Smith et al., 2022; Wei et al., 2022). Because the simulations were allowed to evolve freely, they would not in general have reproduced the meteorological conditions that led to this anomaly.

Because we are using CALIOP's clean dust product, the DSAOD we calculate still contains contributions from dust that is mixed with pollution or marine aerosol. The negative 2020 anomaly observed in India by CALIOP may thus be due in part to the anomalously low dust optical depth noted above. If this is the case, the fact that the simulations are in qualitatively better agreement with the CALIOP anomaly than the MODIS anomaly might suggest that the simulations are overestimating the "true" DSAOD reduction. Reassuringly, however, the ACROS estimate is in good agreement with both the CALIOP estimate and the observations, despite using an independent method to estimate dust optical depth.

Good agreement between the observations and simulations is also found in Europe. Despite model-to-model differences in the DSAOD trend over the reference period, all models simulate both control and perturbed ensembles that are consistent in magnitude with the ensemble of observations. Although three of the four models simulate statistically significant perturbations, whereas the observations do not show a statistically significant response, the magnitudes of the simulated perturbations are very small (indeed, smaller than the spread in observed anomalies).

Models appear to overestimate the DSAOD response to COVID-19 in the East China and Northern Hemisphere domains. The overestimation is more ubiquitous in East China, where only NorESM2-LM simulates a COVID-19 perturbation consistent in magnitude with the observed anomaly. CanESM5.0 and MIROC-ES2L simulate somewhat larger (more negative) anomalies in this region. The fourth model, MRI-

ESM2-0, exhibits substantially different behaviour than the others due to a much steeper trend through the reference period. When the Northern Hemisphere (0°N-70°N) is considered as a whole, two of the models simulate perturbations consistent with the observed anomaly, and two overestimate the AOD reduction. The spatial origins of these overestimations differ: in MRI-ESM2-0, the Northern Hemisphere-averaged anomaly is due almost entirely to the strong negative anomaly over Asia; in CanESM5.0, ensemble-median anomalies are negative throughout the entire region (Figure 3.A.8).

Given the short reference period and substantial interannual variability of the observations, it is challenging to identify whether the simulated trends are representative of those observed. In East China there is some indication that the models may simulate marginally more negative trends than the observations (more visible in the raw data shown in Figure 3.A.6, and when the 2020 anomaly is not included in the timeseries, and consistent with the results of (Lund et al., 2023) for trends over 2005-2017), which could imply that the MMEc may inadequately represent the range of plausible "control observations." However, this discrepancy – if it exists – does not appear sufficient to explain the absence of a statistically significant anomaly in the observations. Visual inspection suggests that the observed 2020 anomalies are consistent with DSAOD excursions measured over the preceding 5 years, even taking any potential trends into account, whereas the simulations show an obvious decrease in 2020. This behaviour is particularly clear when considering the raw data shown in Figure 3.A.6.

### 3.5.2 Sensitivity tests

Having established the magnitude of the observed optical depth anomaly in Section 3.5.1, and identified a number of discrepancies between this anomaly and those simulated by the CovidMIP models, we now conduct a series of sensitivity tests to probe the influence of potential confounding variables on the above results. These sensitivity tests are conducted using CanAM5 (Cole et al., 2023), the atmospheric component of CanESM5. Specifically we use CanAM5.1, a version of the model in which the spurious dust storms have been corrected through retuning of the hybrid tracer parameters (Sigmond et al., 2023). The complete details of these tests are provided in Appendix 3.A.3.

### Sensitivity to control emissions

In CovidMIP, the COVID-19 perturbation was applied to the SSP2-4.5 baseline. This inventory was developed in the 2010s as a projection for the years 2015-2100 (starting from proposals by (Krieler et al., 2012) and (van Vuuren et al., 2012)), and has known differences from the true emissions that have occurred since its development. In particular, it did not account for recent clean air legislation in China, which has substantially reduced the emission of aerosols and their precursors since the early 2010s (e.g. Wang et al., 2021; Zheng and Unger, 2021; Paulot et al., 2018). Furthermore, biomass burning emissions in SSP2-4.5 are described by a linear projection which does not capture the high interannual variability of these sources.

We investigate the sensitivity of our results to biases in the baseline emissions inventories by constructing updated inventories for both anthropogenic and biomass-burning aerosol emissions, and using these inventories to run 10-member ensembles in CanAM5.1. Anthropogenic emissions are based on the 2021-04-21 release of the Community Emissions Data System (CEDS) emission inventory (Smith et al., 2021), which provides emissions estimates up to 2019, and year-specific biomass burning emissions are taken from the Global Fire Emissions Database (GFED v4.1s). Details of the inventory construction and model configuration are provided in Appendix 3.A.3.

These simulations ("CanAM-new-emis") are compared to the original CanESM5.0 ensemble in Figure 3.5.3, which shows dust-subtracted aerosol optical depths as in Figure 3.5.2. In all regions except India, updating the baseline emissions inventory reduced the median separation between control and perturbed ensembles, because the COVID-19 perturbation was applied as a percent change to a smaller initial value (Figures 3.A.9, 3.A.11). The effects of this reduction vary: in East China, the update is sufficient to bring the simulated COVID-19 signal into agreement with the observed anomaly (i.e., the separation between observed and simulated ensembles is no longer statistically significant), whereas in the Northern Hemisphere the simulated response is brought somewhat closer to the observations but the difference remains significant. In Europe the main effect of the update is to remove the simulated trend over the 2015-2019 reference period, bringing the simulations into qualitatively better agreement with the observations over this period and reducing the 2020 anomalies to which the trend had contributed. In India, emissions were largely unaffected by the update, so the results do not change except for the loss of the large-negative-anomaly tail on the perturbed distribution. This change could be due either to the updated

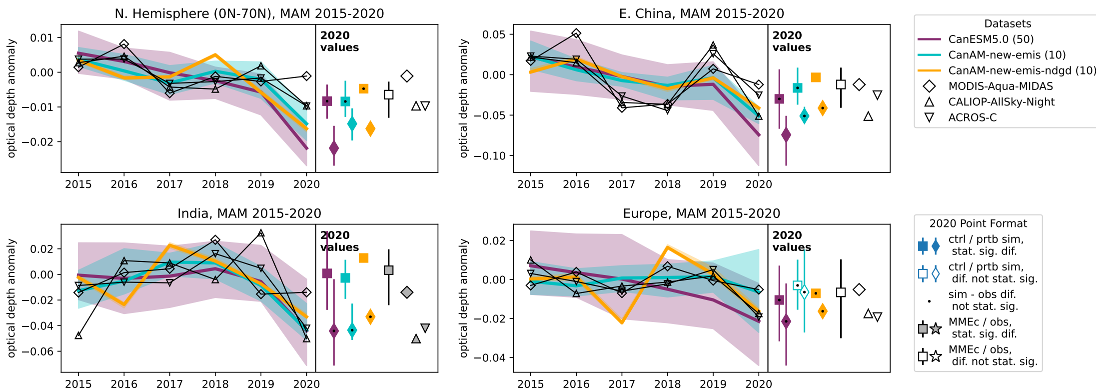


Figure 3.5.3: As Figure 3.5.2, but comparing dust-subtracted AOD in the 3 CCCma simulations: CanESM5.0 (the original CovidMIP implementation), CanAM-new-emis (an atmosphere-only simulation with updated anthropogenic and biomass-burning aerosol emissions; Section 3.5.2), and CanAM-new-emis-ndgd (as CanAM-new-emis, but nudged to meteorological fields taken from ERA5 reanalysis; Section 3.5.2). The MMEc in this figure is drawn from CanESM5.0, CanAM-new-emis, and CanAM-new-emis-ndgd; using the MMEc from Figure 3.5.2 does not change the statistical significance of the observed anomaly.

inventory or to the reduced ensemble size.

These results suggest that in India, inferences drawn from the other CovidMIP models will likely not be affected by biases in the underlying baseline inventory as long as the applied perturbation is realistic. In the Northern Hemisphere, East China, and Europe, the apparent overestimation of the COVID-19 response identified in CanESM5.0, MIROC-ES2L, and MRI-ESM2-0 may have been partially caused by overestimates of the control emissions and thus of the absolute magnitude of the COVID-19 disruption. Confirming this hypothesis is beyond the scope of this work. The changes in DSAOD magnitude through the reference period which occur as a result of the updated emissions are explored in Section 3.6 and Appendix 3.A.3.

### Sensitivity to meteorological conditions

Once aerosols have been emitted, the aerosol burden that remains in the atmosphere and the optical depth that this burden produces are determined by the meteorological conditions. We assess the degree to which meteorological conditions impacted the magnitude of the apparent COVID-19 response using a second CanAM5.1 experiment, CanAM-new-emis-ndgd.

CanAM-new-emis-ndgd simulations were nudged to temperature, wind, and humidity fields taken from the European Centre for Medium-Range Weather Forecasts (ECMWF) 5th Generation Reanalysis (ERA5; Hersbach et al., 2020); details of this nudging process are described in Appendix 3.A.3. Anthropogenic and biomass burning aerosol emissions in CanAM-new-emis-ndgd were taken from the same updated inventories as were used in CanAM-new-emis.

A comparison between the absolute AOD simulated by CanESM5.0, CanAM-new-emis, and CanAM-new-emis-ndgd is provided in Appendix 3.A.3. The degree to which updating the inventory and nudging towards ERA5 reanalysis improves the agreement of CanAM5.1 with the observed AOD fields (in terms of both average magnitude and the pattern of interannual variability) varies from region to region and, in the Northern Hemisphere region, depends on which satellite dataset is considered as reference. In general the nudged simulations exhibit higher interannual variability than the free-running simulations do, although this variability generally falls within the envelope of the larger coupled ensemble. In Europe, the nudged ensemble exhibits substantially higher interannual variability than do either of the free-running ensembles or the observations, indicating that the model may underpredict the variability of and AOD sensitivity to temperature, winds, and/or humidity in this region.

Results from CanAM-new-emis-ndgd are compared with CanAM-new-emis and CanESM5.0 in Figure 3.5.3. Because the ensemble spread in CanAM-new-emis-ndgd is negligible, we can assume that any difference between the control and perturbed ensembles is due to the signal of COVID-19 and not to internal variability. It is worth noting that the meteorological fields towards which the simulations were nudged may themselves have been impacted by the COVID-19 emission reductions. For instance, a reduction in scattering aerosols could have resulted in local warming. The control and perturbed CanAM-new-emis-ndgd simulations are therefore not fully independent. However, in all regions except Europe, the separation between the control and perturbed CanAM-new-emis-ndgd ensembles is large enough that this effect is unlikely to materially affect our conclusions.

The 2020 anomalies in the nudged simulations, considered in the context of the variability differences between datasets, are largely consistent with those from the free-running simulation CanAM-new-emis. In East China, both CanAM-new-emis-free and CanAM-new-emis-ndgd simulate lower interannual variability than do the observations; the pattern of variability is perhaps somewhat improved in the nudged ensemble. In the previous section we found that updating the emissions inventory substantially reduced the magnitude of the perturbed anomaly, bringing it into agreement with the observed anomaly. In that model configuration, both control and perturbed ensembles simulated 2020 anomalies that were consistent with the observations. Nudging results in a small positive shift in both the control and perturbed anomalies, such that the control moves just outside the range of the observed ensemble. However, since the difference between the control and the observations is substantially smaller than the spread in observational estimates, it is reasonable to describe the nudged control ensemble as still qualitatively agreeing with the observations.

In India, the nudged control ensemble exhibits a positive anomaly suggesting that meteorological conditions may in fact have partially masked the strength of the COVID-19 response. Because the observed interannual variability is reproduced less well in the nudged than the free-running simulations, detailed comparisons between the observed and simulated 2020 anomalies would not be robust; however, it is reassuring to note that the 2020 perturbed anomaly is in excellent agreement with the observations, and the results of our statistical comparisons remain unchanged.

In Europe the nudged ensemble exhibits higher interannual variability than do either of the free-running simulations. The pattern of positive and negative anomalies is consistent with, although substantially amplified relative to, observations from MODIS-Aqua; however, this pattern of variability is not reproduced in the two CALIOP-derived datasets. The simulated COVID-19 perturbation is small relative to this variability and, as in all previous ensembles, the control and perturbed 2020 anomalies are both consistent with the observed ensemble.

When averaged over the entire Northern Hemisphere (0°N-70°N), neither the free-running nor nudged ensembles reproduce well the observed pattern of interannual variability. Overall, our results here are unaffected by nudging: the control ensemble is consistent with the observed anomalies, and the perturbed ensemble values are too negative.

In all regions, the separation between the control and perturbed CanAM-new-emis-ndgd ensembles is on the order of the spread in observational estimates, suggesting that further observationally-based model evaluation may not be feasible given current observational uncertainties. Improving observational constraints beyond this point would require substantially reducing the differences between remotely sensed products retrieved using different instruments and algorithms.

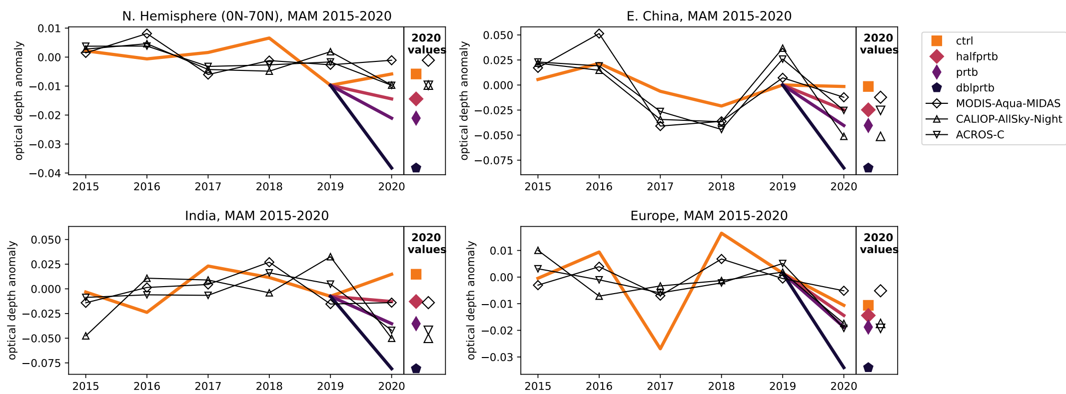


Figure 3.5.4: Effects of varying the magnitude of the simulated COVID-19 perturbation in CanAM5.1. The control simulation, nudged to ERA5 fields, is shown in orange. The remaining symbols show simulations forced with COVID-19 perturbations half, one, and two times the magnitude of the original CovidMIP perturbation. All simulations use the updated baseline inventory introduced in Section 3.5.2.

### Sensitivity to perturbation size

Finally, in this section we address the potential impact of uncertainties in the perturbation applied to simulate COVID-19. Although as stated above our observational constraints of model performance are limited by observational uncertainty, it is still informative to understand how sensitive our comparisons are to uncertainties in the perturbation size.

The aerosol emission reductions used in the simulations considered to this point were estimated from mobility data by (Forster et al., 2020) and gridded for use in CovidMIP by (Lamboll et al., 2021). In brief, the reductions were determined as follows. Google mobility data were used to estimate the country-by-country reduction in activity at transit stations and at residential, workplace, retail, and recreation locations, with Apple mobility data used as a secondary check. These reductions were then used to estimate sector-by-sector $CO_2$ emission reductions following the methodology of (Le Quéré et al., 2020) but using the mobility-data-derived estimates of activity changes in each sector. The original (Le Quéré et al., 2020) estimates, derived from an estimate of "confinement level" on a scale of 1-3 based on government and media reporting, were used for countries for which mobility data were unavailable (notably for our analysis, this includes China) and for aviation and shipping sectors. Non-$CO_2$ emissions for 2020 were then determined by scaling each species'

2015 emissions by the ratio of $CO_2$ emissions in 2015 and 2020. This scale factor was determined uniquely for each country and sector.

This approach has the advantage of being self-consistent and bottom-up, but does come with a number of limitations. Notably, mobility data may not be a good proxy for emission changes in all sectors (e.g. some industries may have background emission even in the absence of active production), and changes in Apple or Google mobility data may overestimate the actual reduction in traffic (e.g. there may be a correlation between the subset of the population who have smartphones and those who have the opportunity to work from home, particularly in less-affluent nations). (Gensheimer et al., 2021) measured differences of up to 60% between mobility data and local traffic changes, and could not determine a unique functional relationship between these quantities that applied in all regions. Finally, $CO_2$ and non-$CO_2$ species have not evolved in tandem at the country/sector level over 2015-2020 (Smith et al., 2021), so scaling all species by changes in $CO_2$ introduces further error to the analysis. There is thus substantial uncertainty in the CovidMIP emission reductions.

We perform a sensitivity test by running nudged, baseline-corrected CanAM5.1 simulations with a range of perturbation strengths: no perturbation (the control), and perturbations of half, one, and two times the original CovidMIP experiment. We simulate only a single realization of each because, as demonstrated in Figure 3.5.3, nudging effectively removes all ensemble spread in AOD.

Given the uncertainty in the observations, and the fact that nudging does not result in particularly good agreement with the observations (Figures 3.A.11 and 3.A.12), it is not constructive to directly compare the magnitude of the observed and simulated AOD anomalies as a function of perturbation strength. However, comparing the spread in the observations to the spread in simulated responses to different perturbation strengths can indicate whether or not uncertainties in the perturbation would affect our model evaluation results (i.e. whether they would be visible over the observational uncertainty).

The results of these simulations are presented in Figure 3.5.4. In all regions, the spread in the observed anomalies is larger than the separation between the control and half-strength, or half- and full-strength, simulated perturbations. So although a doubling of the perturbation strength is clearly inconsistent with the observations, uncertainties of up to $\sim$50% would not impact our model evaluation assessment. In Europe, the perturbation strength could be very nearly doubled without the spread exceeding observational uncertainties. In conclusion, modest uncertainties in the perturbation size are unlikely to have impacted our results in the preceding sections.

## 3.6 Discussion and conclusions

### 3.6.1 Summary and synthesis

In this work we have used remotely-sensed observations of AOD changes from the spring of 2020 to evaluate the response of aerosol optical depth to emission changes in CMIP6-class models from the CovidMIP project. We then performed sensitivity tests in CanAM5, the atmospheric component of CanESM5, to assess the influence of model inputs and meteorological variability on our comparison.

The response of total aerosol optical depth to the COVID-19 emission reductions is, unsurprisingly, very small and not statistically detectable in most regions. Aerosols are characterized by substantial interannual variability, many drivers of which were not affected by the COVID-19 lockdowns. Detection of a response is further hampered by biases in model inputs and by uncertainty in the observations.

When the mineral dust component has been removed from aerosol optical depth measurements, good agreement between the observed and simulated responses is found in India (where both exhibit a significant COVID-19 response) and in Europe (where a difference can only be detected in the simulated ensemble means, and where both control and perturbed anomalies are consistent with the observations). Models appear to overestimate the COVID-19 response in the Northern Hemisphere generally and in East China specifically, although our results suggest that a more accurate emissions inventory can reduce this discrepancy. Our conclusions appear to be insensitive to modest uncertainties in the magnitude of the simulated COVID-19 perturbation, in part because of the large spread in observational estimates of the COVID-19 response. This spread, which is caused by systematic biases between the different datasets, prohibits a more detailed evaluation of the simulated response.

The sensitivity studies presented here incorporate aerosol emission inventories which have been updated from the SSP2-4.5 scenario used in the original CovidMIP experiment. As well as altering the magnitude of the COVID-19 perturbation, these updates cause important changes in the magnitude of DSAOD simulated through the reference period. In Appendix 3.A.3 we decompose simulated changes in the magnitude of DSAOD over 2015-2019 into reductions caused by changes in anthropogenic emissions, biomass burning emissions, and model configuration (coupled vs atmosphere-only). In all regions, DSAOD was reduced in CanAM-free from the original CanESM5.0 CovidMIP simulation, but the relative contributions to this reduction varied. In East China, the reduction in anthropogenic emissions dwarfed other changes, causing a 30% decrease in DSAOD over the reference period compared to only an 8% reduction from model configuration. Emission- and configuration-induced changes were comparable in India, and model configuration had a larger effect in Europe. Averaged over 0-70°N, emission inventory and model configuration caused comparable reductions in simulated DSAOD; increased boreal latitude (50-60°N) biomass burning partially compensated for decreases in anthropogenic emissions. We emphasize that the changes in DSAOD stemming from model configuration led mainly to a systematic offset and had little impact on the anomalies considered in our main analysis.

The impact of anthropogenic emission inventory on total AOD and aerosol radiative forcing have been recently investigated by Lund et al. (2023), who compare simulations using the two CEDS inventories analyzed here, as well as emissions from ECLIPSE v6. Although they do not assess the impacts of biomass burning emissions and they look at total rather than dust-subtracted AOD, their findings are generally consistent with those presented here. In particular they identify a reduction in AOD and improved agreement with observational trends over 2005-2017, dominated by reductions in emissions over East Asia.

There exist substantial differences in biomass burning emissions between different inventories (Pan et al., 2020). We have used GFED v4.1s, which is among the low-emission datasets; it is possible that a different biomass burning inventory may have been more accurate. However, since in three of our four regions the MAM biomass burning emissions are small compared to anthropogenic emissions, this choice is unlikely to affect our results. If an underestimation of biomass burning emissions or their variability did impact our results, it would likely be in the Northern Hemisphere domain. Not only does the Northern Hemisphere as a whole contain a higher proportion of biomass burning to anthropogenic emissions, but emissions are poorly constrained in the boreal latitudes due in part to a scarcity of observational data (Pan et al., 2020).

In East China, discrepancies between observed and simulated anomalies may also be due in part to processes that were not captured in the models. It has been well documented that a combination of stagnant meteorological conditions, including an unusually weak East Asian winter monsoon, and a highly polluted background resulted in haze production when emissions decreased (Gao et al., 2022; Chang et al., 2020; Huang et al., 2021; Kong et al., 2023; Le et al., 2020; Li et al., 2021; Shi and Brasseur, 2020; Wang et al., 2020; Xu et al., 2020; Zhao et al., 2022). Similar local enhancements in pollution levels were identified in a number of polluted regions around the globe (Balamurugan et al., 2021; Gaubert et al., 2021; Sicard et al., 2020; Venter et al., 2020). These enhancements occur because, in $NO_x$-saturated regions, the reduction of $NO_x$ emissions (largely due to decreased vehicle traffic) led to increased ozone production, which in turn increased the oxidative capacity of the atmosphere and resulted in enhanced secondary aerosol formation (Kroll et al., 2020). These unusual meteorological conditions, and the resulting complex and nonlinear chemical reactions, are not well represented by the CovidMIP models. Indeed, of the models considered here, only MRI-ESM2-0 includes an interactive ozone scheme; the other models used a prescribed perturbation (Lamboll et al., 2021). Disagreement between the observed and simulated responses is therefore unsurprising. Conducting a similar analysis in models that simulate more complex chemistry would be a valuable direction for follow-up analysis, and the inclusion of a prognostic ozone scheme will be critical for representing the climate and air quality effects of future emission reductions in polluted regions.

Interpretation of the results for East China is further complicated by the presence of spatial structure in both the magnitude and tendency of aerosol emissions in this region, with urban areas characterized by high baseline emissions but negative trends whereas rural areas have lower emissions with positive trends. Modest differences in the relative magnitudes of these components of the signal could likely have substantial impacts on the area-averaged mean responses derived from different datasets.

We have assessed aerosol changes averaged over fairly large geographic regions, and this decision will influence our results. Selecting a smaller box, centred over the most populated urban areas, would likely yield a larger COVID-19 signal. On the other hand, the selection of a larger domain allows us to average over different potential trajectories, so we do not need to worry about signals appearing and disappearing by being advected in or out of our analysis regions. Furthermore, while local AOD changes are relevant when studying air quality, the regionally-averaged aerosol response to an emission reduction is more relevant for understanding potential climate impacts.

This analysis assesses the capability of models to realistically simulate the *net* effect of emission changes on aerosol optical depth. As described in Section 3.2.1, the focus on AOD folds in the effects of many different processes. In order to help disentangle the different drivers of model performance, future analyses would benefit from studies of aerosol concentrations, which are an intermediate stepping point between emission and optical depth. Additional insight could be gained through an investigation of individual aerosol species; sulfate, for example, would exhibit a stronger COVID-19 signal than total AOD does. We have not conducted such an analysis due to the limited availability of speciated data amongst the CovidMIP models.

### 3.6.2 Comparison to previous studies

We have taken the approach of applying a single consistent framework to all four analysis regions. There is also much to be learned from bespoke analyses of the observed changes in each individual region, and indeed numerous such analyses have been conducted.

In India, AOD reductions have been reported by Acharya et al. (2021); Gouda et al. (2022); Ranjan et al. (2020); Rani and Kumar (2022); Smith et al. (2022), and Wei et al. (2022). The magnitude of reduction has been found to vary regionally and with the period of 2020 considered, and for relative changes, on the choice of baseline; in general it is reported to be on the order of 10-15% when averaged over India as a whole. These reductions are comparable to those we find from MODIS and MISR (-13% and -14% respectively) but somewhat smaller than those returned by CALIOP and ACROS-C (-24% and -21%). We emphasize that, as highlighted above and also by Smith et al. (2022) and Wei et al. (2022), a substantial portion of the observed reduction is due to anomalously low dust optical depth.

In China, the measured AOD response depends sensitively on the choice of reference period, since the trend in aerosol emissions reversed in or around 2013 (Zheng et al., 2018). When underlying trends are accounted for, the 2020 AOD anomalies are not significant, although species including $NO_2$, $SO_2$, and $SO_4$ do exhibit substantial changes (Diamond and Wood, 2020; Field et al., 2021; Smith et al., 2022). When trends are not accounted for, AOD reductions in Central Eastern China range from -14% to -30% depending on the choice of reference period; compared to the 2016-2019 mean (similar to our 2015-2019 reference period), AOD in this region was reduced 14-17% (Field et al., 2021). AOD increased in South China (Field et al., 2021; Diamond and Wood, 2020; Acharya et al., 2021), possibly as a result of biomass burning in Thailand, Myanmar, and Laos (Field et al., 2021). In comparison, we find an observed decrease of 4-13% relative to the 2015-2019 mean, when averaging over a domain that contains both these areas of positive and negative anomalies.

In Europe, Smith et al. (2022) report detectable changes in the summer and autumn of 2020, but not in the spring which is our focus in this work. Springtime changes may be detectable when smaller averaging boxes are used: Ibrahim et al. (2021) report an AOD reduction in Central Europe but an increase around the edges of the domain, which when averaged together would be consistent with our non-detection. It has been demonstrated that this reduction is driven by an increase in the number of moderately-low AOD hours, as opposed to a few extremely low hours (van Heerwaarden et al., 2021).

As highlighted in the introduction, model-based studies have predominantly been focused on the climate response to aerosol emission reductions, rather than the AOD change itself. However, they generally report modest decreases in zonal average AOD over $\sim$30°N in the spring, particularly March, of 2020 (Fasullo et al., 2021; Fiedler et al., 2021; Forster et al., 2020; Fyfe et al., 2021; Gettelman et al., 2021; Jones et al., 2021; Weber et al., 2020). In many cases this reduction is only detectable in the ensemble mean. We find similar behaviour in the CovidMIP models (not shown); as expected, the observed signal is less clear.

### 3.6.3 Conclusions

The reduction in aerosol emissions associated with the COVID-19 pandemic provided a unique opportunity for Earth system model evaluation. We have investigated changes in total and dust-subtracted aerosol optical depth during MAM 2020 in order to assess the AOD sensitivity of CMIP6-class Earth system models. The impacts of internal variability, background emissions levels, and simulated perturbation size on our results have been assessed with a series of sensitivity tests.

Despite the dramatic economic and lifestyle changes associated with the COVID-19 lockdowns, a statistically significant reduction in observed aerosol optical depth is only identified over India. CovidMIP models reproduce the observed responses reasonably well over India and Europe but appear to over-estimate the magnitude of response in East China and the Northern Hemisphere (0°N-70°N). We demonstrate that this discrepancy can be partially resolved in CanAM through the use of an updated emissions inventory; investigating whether the other models would show similar improvement is an avenue for further study. The substantial uncertainty in remotely-sensed observations of AOD precludes a detailed assessment of the relative biases in different models. As such, this analysis motivates future research into the drivers of the systematic biases in satellite retrievals of aerosol fields, particularly in the context of monitoring future emission reductions which are expected to take place over the coming decades.

AOD sensitivity is critical for the prediction of short-term climate impacts to emission reductions, and our results will provide important context for interpreting the simulated climate impacts of proposed mitigation pathways of both aerosols and co-emitted greenhouse gases.

Table 3.A.1: Mean AOD over reference period (2015-2019) from different satellites, and the spread in these estimates. The relative spread is calculated with respect to the mean of the highest and lowest AOD estimates in each region.

| Region | MODIS Aqua | MISR | CALIOP ASN | ACROS-C | absolute spread | relative spread |
|---|---|---|---|---|---|---|
| N. Hemis | 0.231 | 0.190 | 0.178 | 0.181 | 0.053 | 26% |
| E. China | 0.483 | 0.331 | 0.445 | 0.451 | 0.152 | 30% |
| India | 0.402 | 0.365 | 0.459 | 0.477 | 0.112 | 27% |
| Europe | 0.157 | 0.125 | 0.127 | 0.124 | 0.033 | 23% |

# 3.A Appendix to Chapter 3

## 3.A.1 Observational uncertainties and sampling differences

This work is based on comparisons between observed and simulated anomalies of AOD. In order to draw meaningful conclusions from these comparisons we need to assess how much of the difference between our datasets comes from differences in sampling, and how much can be attributed to uncertainties or biases in the products themselves. Here we assess the role of sampling differences in explaining the considerable spread between AOD estimates from different satellites, which can differ by 20-30% (Table 3.A.1).

Our main analysis used monthly and regional mean data products. For the simulations, these means are spatiotemporally complete; the observed means use retrievals obtained at the satellite's particular overpass time, in clear-sky conditions (for the passive sensors), when the retrieval was successful and not prevented by a myriad of potential limitations such as sun glint or complex terrain. Here we conduct a systematic intercomparison between pairs of observational data products, with each pairing selected to isolate the effect of a particular sampling effect. Discrepancies that cannot be attributed to sampling differences are then used to estimate the degree of uncertainty in our observed AOD responses. Throughout, figures that do not require gridcell-to-gridcell comparisons (spatial-mean timeseries, histograms) are generated at the products' native resolutions, and figures that do require gridcell-to-gridcell comparisons (scatter plots, calculation of correlation between datasets) are generated on fields that have been interpolated to a common $1°\times1°$ resolution.

### Temporal sampling

We first assess the effects of temporal sampling on our comparison between satellite observations, which are sampled only at a particular overpass time, and model simulations, which are integrated over the full diurnal cycle. Figure 3.A.1 compares three-hourly, daily, and monthly AOD values for MAM 2004 from a sample CanAM5 simulation. Timeseries plot the evolution of AOD over the three-month period in each of our analysis regions, with blue, orange, and green lines corresponding to the different averaging timescales. A dotted black line indicates the diurnally-integrated, MAM-mean AOD. For all regions except the Northern Hemisphere, blue horizontal lines additionally show the mean of AOD for MAM 2004 sampled only at our satellites' overpass times: dash-dot for the Aqua daytime overpass (MODIS-Aqua and CALIOP daytime product), dotted for the Aqua nighttime overpass (CALIOP nighttime product), and dashed for the Terra daytime overpass (MODIS-Terra, MISR). Local satellite overpass times were estimated from Figure 5 of Levy et al. (2018). These overpass times were converted to UTC and the closest 3-hour timestamp was selected from the model output. The MAM-mean AODs obtained by sampling at each overpass time, and their biases relative to the diurnally-integrated values, are summarized in Table 3.A.2.

The MAM-mean AODs of the diurnally-integrated and overpass-sampled products are very similar, especially compared to the spread in AOD from different instruments (Table 3.A.1). This fact is unsurprising given that the three-hourly and daily time series demonstrate that the magnitude of the simulated diurnal cycle is negligible compared to the weekly- and monthly-scale variability. Subject to the accuracy of CanAM5's simulated diurnal cycle, then, we do not expect differences between the observed and simulated AOD samples to be caused by differences in the temporal sampling frequency.

Even though the above results indicate that simulated AOD does not vary substantially throughout the day, other factors affecting the retrieved AOD may. These factors include the possibility of a diurnal cycle in cloud cover (which would introduce sampling differences between the products), or in retrieval uncertainty (such as the increased uncertainty in daytime CALIOP retrievals due to the solar background). We assess this possibility by comparing sets of observations taken by instruments with the same algorithms but different overpass times: MODIS Aqua and MODIS Terra in Figure 3.A.2 and CALIOP AllSkyDay and CALIOP AllSky Night in Figure 3.A.3.

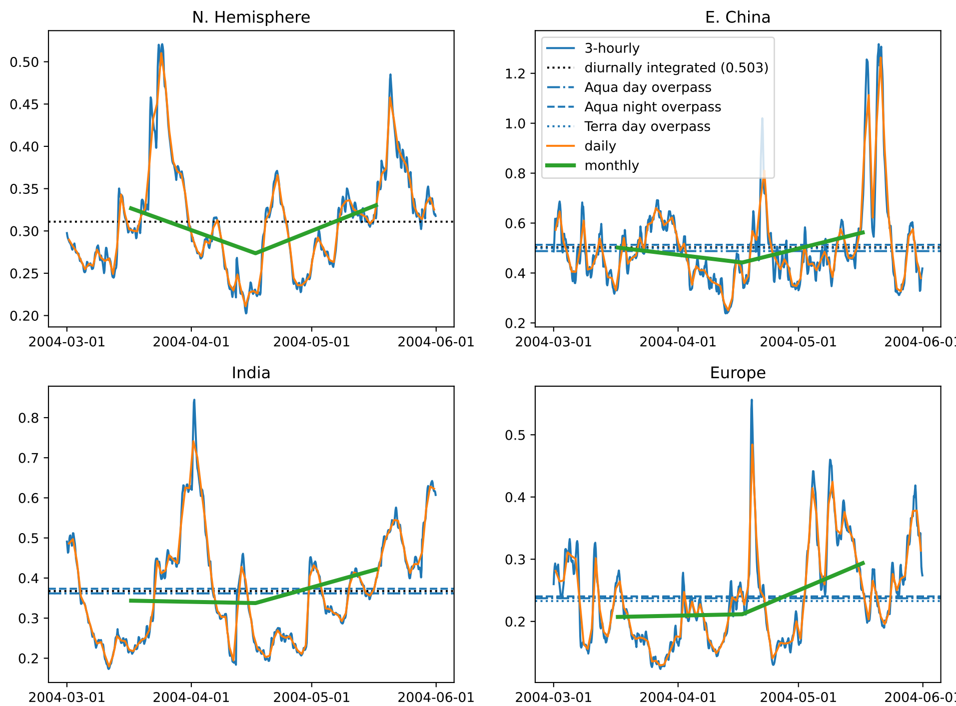


Figure 3.A.1: The impacts of temporal averaging and sub-daily sampling demonstrated with CanAM5. Timeseries show 3hr, daily, and monthly AOD (blue, orange, and green lines respectively) through MAM 2004 in our 4 analysis regions. Horizontal lines show the mean AOD when averaged over the full time period from March 2004 to June 2004 (black) and when sampled only at satellite overpass times (blue); these values are tabulated in Table 3.A.2.

Table 3.A.2: Mean AOD values obtained from 3-hourly CanAM output, when averaged over all of MAM 2004 ("full day") and when sampled only at satellite overpass times. Values in parentheses indicate the percent change in AOD when sampled at a particular overpass time as compared to the diurnally-integrated value. These relative differences are an order of magnitude smaller than the spread between region-mean AOD from different satellites (Table 3.A.1).

| Region | Full Day | Aqua Day Overpass | Aqua Night Overpass | Terra Day Overpass |
|---|---|---|---|---|
| N. Hemis | 0.311 | - | - | - |
| E. China | 0.503 | 0.488 (-3.0%) | 0.513 (+2.0%) | 0.499 (-0.8%) |
| India | 0.368 | 0.362 (-1.6%) | 0.373 (+1.3%) | 0.362 (-1.6%) |
| Europe | 0.239 | 0.237 (-0.8%) | 0.240 (+0.4%) | 0.233 (-2.5%) |

MODIS Terra crosses the equator from North to South at 10:30 local time, and MODIS Aqua crosses from South to North at 13:30. For regions near the equator (e.g. India), their overpass times thus differ by roughly three hours; further poleward (e.g. Europe) the difference is larger. There is a known offset of $\sim$0.02 ($\sim$13%) between the global, monthly-mean AOD values retrieved by the two MODIS instruments, with Aqua in better agreement with AERONET measurements and Terra biased higher (Levy et al., 2018; Schutgens et al., 2020). A detailed assessment of the Level 2 daily aerosol products, incorporating ground-based AERONET observations and the Goddard Earth Observing System (GEOS-5) Earth system model, has demonstrated that this offset is not due to diurnal cycles in either aerosols or clouds, but likely to a calibration or algorithmic bias (Levy et al., 2018).

The Levy et al. assessment investigated global AOD biases. It is possible that diurnal cycles could lead to significant biases on a regional scale. Overall, however, Figure 3.A.2 suggests that the Aqua and Terra products are in good agreement and the effect of differing overpass times on MAM-mean AOD is small.

Figure 3.A.3 undertakes a similar comparison between CALIPSO's all-sky day and night products. Because these products are produced by a single instrument, calibration drift is not a concern. Using the all-sky product eliminates the sampling effects that could be introduced by diurnal cycles in cloud cover. It is worth noting, however, that CALIPSO's daytime products have higher uncertainty due to the presence of a solar background which reduces the signal-to-noise ratio (Young et al., 2018). There are appreciable differences between the distributions of daytime and nighttime AOD retrievals over East China and Europe, with the nighttime product being skewed to larger values than the daytime one. Reassuringly, however, the distributions of anomalies are in good agreement. The low correlations in the scatter plots of these anomalies are not concerning, since aerosols may have advected over the 12 hours between overpasses, so we would not necessarily expect gridcell-by-gridcell agreement between the two products. The important metric in this comparison is that the aggregate distribution of anomalies is similar.

In principle, instrument-to-instrument spread in the amount of dependence on overpass time could indicate the presence of diurnally-varying biases in the various products. However, because there is different spacing between the overpass times of the two instrument sets considered here, the existence of these biases cannot be disentangled from a true diurnal cycle in AOD. For the purposes of this analysis, however, the impact of temporal sampling on spatiotemporally-aggregated AOD anomalies is

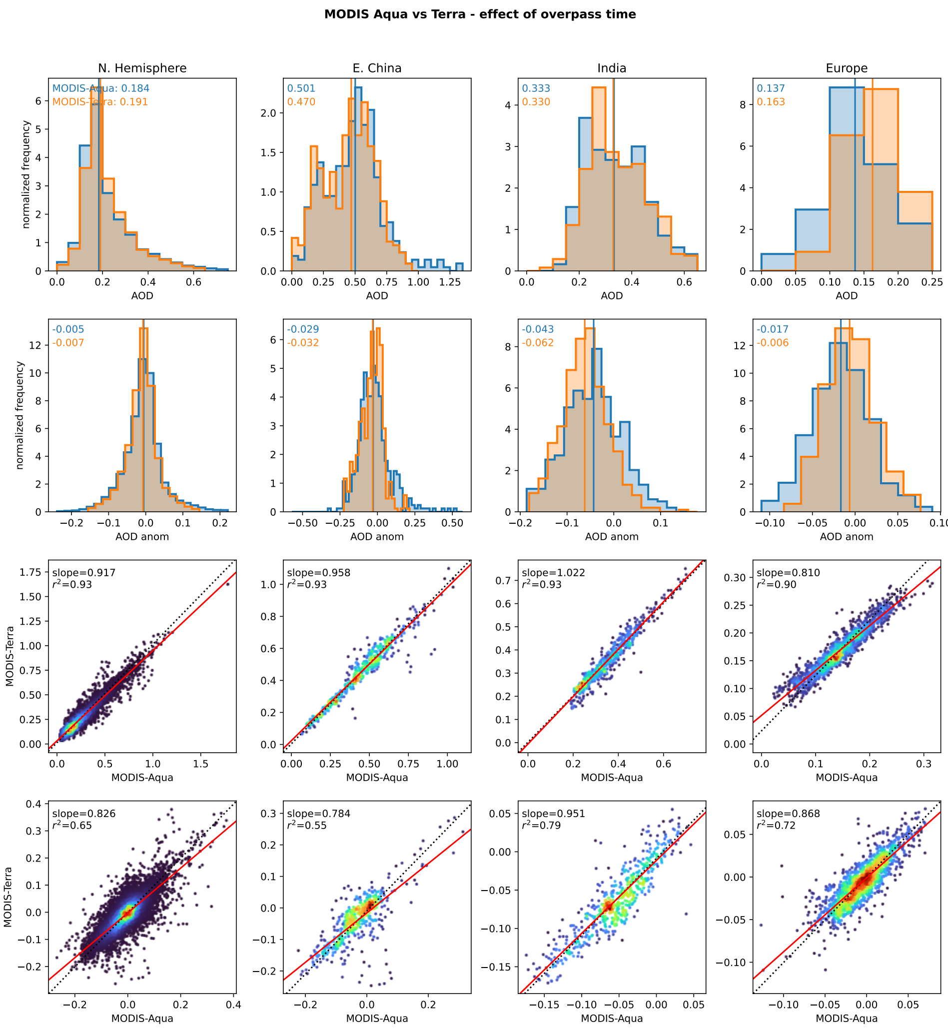


Figure 3.A.2: Investigation of the effects of overpass time on observed AOD, by comparing retrievals from MODIS-Terra (equatorial overpass 10:30 local time descending) and MODIS-Aqua (equatorial overpass 13:30 local time ascending). Histograms show the distributions of MAM 2020 AOD values (top row) and anomalies (bottom row) at the grid cell level in our 4 analysis regions, with blue and orange corresponding to MODIS- Aqua and MODIS-Terra respectively. Note that the bin width in each panel is the same: 0.05 for raw AOD values, and 0.02 for AOD anomalies. Text in the upper left corner of each panel lists the median value in each distribution (blue and orange for Terra and Aqua respectively). Scatter plots show these same distributions plotted against each other, again with AOD values in the top row and anomalies in the bottom. Red lines show a linear fit to the scatter, dotted black lines show 1:1 to guide the eye, and colour indicates normalized point density. Because these are both MODIS instruments they share the same algorithm, cloud mask, etc. and only differ in overpass time.

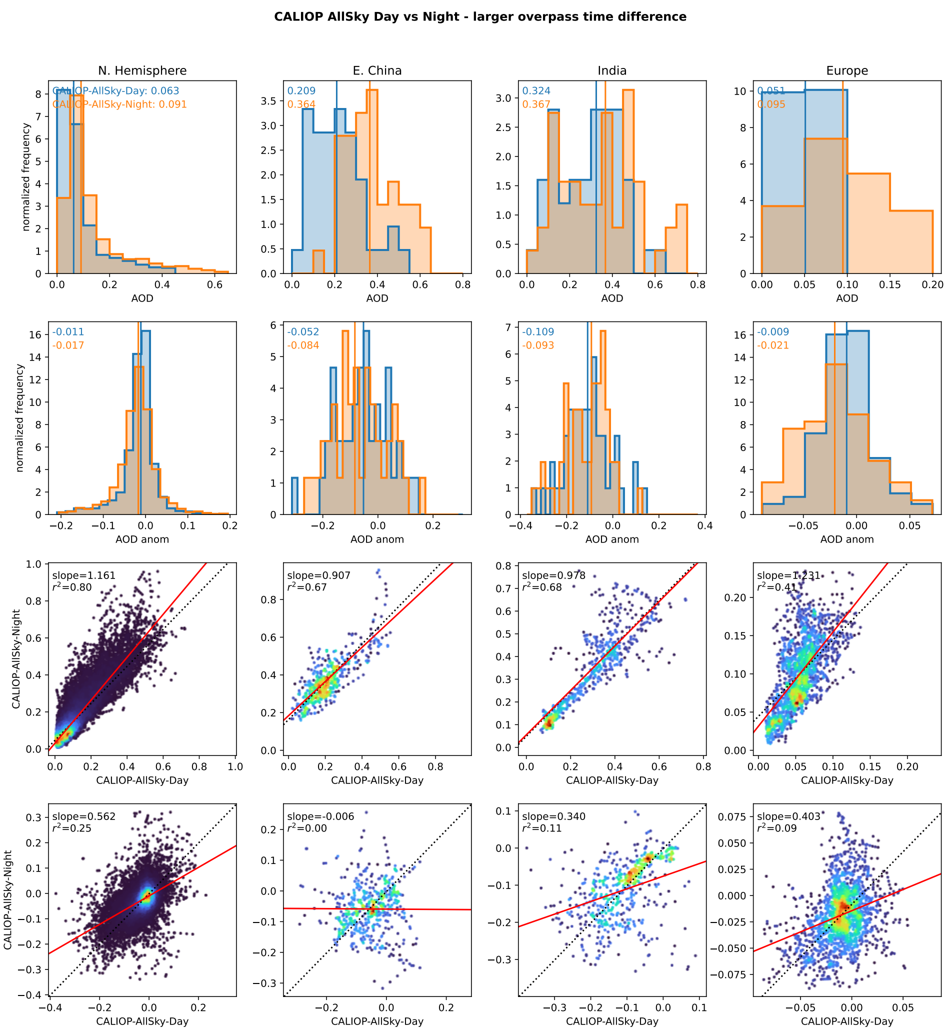


Figure 3.A.3: As Figure 3.A.2 but comparing CALIPSO all-sky measurements made during the day and night overpasses (blue and orange histograms; 13:30 and 01:30 equatorial crossings respectively). Because CALIPSO is a single satellite it is not subject to calibration drift the way that MODIS-Aqua and -Terra are. Further, using the all-sky product eliminates the potential sampling differences that could be induced by diurnal cycles in cloud cover. Although differences are seen in the distributions of daytime and nighttime AODs, particularly over East China and Europe, the distributions of anomalies are in good agreement. The low correlations may be the result of advection, since aerosols may have moved about the region during the 12 hours between overpasses. Of greater importance in this comparison is the overall distribution shapes, which we find to be similar.

found to be small and is unlikely to be a dominant contributor to the spread between datasets seen in the main analysis.

### Cloud masking

We next compare the all-sky and cloud-free CALIPSO products to isolate the impacts of cloud masking, another difference between the sampling of the models and the passive satellites. We use the daytime CALIPSO product as it is expected to be most similar to the passive sensors, which can only observe in cloud-free conditions.

As Figure 3.A.4 demonstrates, the differences between all-sky and cloud-free AOD retrievals measured simultaneously by the same instrument are small when spatially aggregated and averaged over a three-month time period. Cloud-masking-induced spatiotemporal sampling differences between the observed and simulated datasets are thus unlikely to contribute substantially to the differences between datasets in our analysis.

### Instrument-to-instrument differences

Having established that overpass time and cloud masking have small effects on the 3-month spatiotemporal means considered in this work, particularly when considering anomalies, we next compare the AOD retrieved by two different instruments that are orbiting on the same satellite. Comparing MODIS-Terra and MISR, both onboard the Terra satellite, is the closest we can come to isolating the effect of retrieval algorithm on AOD estimates. We use "algorithm" here in the broadest sense, to include not only differences in the AOD retrieval process but also differences in cloud masking, differing susceptibility to effects like sun glint, and the impacts of product resolution. Note that despite being mounted on the same satellite, the two instruments are not viewing the same scene: MISR's field of view is much smaller than, and embedded within, MODIS's.

Numerous comparisons between MODIS Terra and MISR exist in the literature. These include both retrieval-level assessments and comparison of the resulting spatiotemporally aggregated products. When MODIS Terra and MISR conduct simultaneous retrievals of the same scene, the resulting optical depth measurements are in reasonably good agreement. In an assessment of previous versions of the algorithms (MODIS C5 and MISR v22; our analysis uses MODIS C6.1 and MISR v23), Kahn et al. (2009) report correlations of $\sim 0.9$ over ocean and $\sim 0.7$ over land. However,

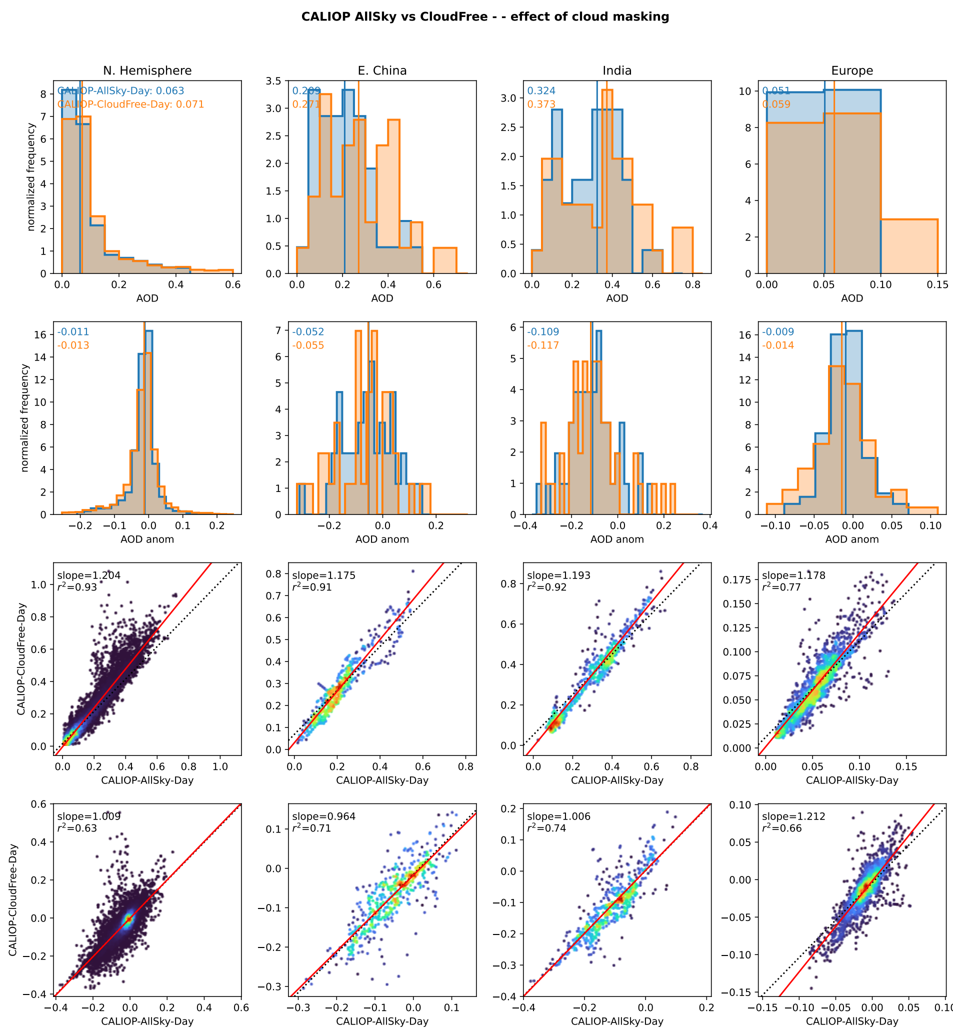


Figure 3.A.4: As Figure 3.A.2 but comparing CALIPSO all-sky (blue) and cloud-free (orange) data products to isolate the sampling effects of cloud masking.

these coincident retrievals are comparatively rare. Factors limiting the attainment of coincident retrievals include differences in the instruments' cloud masking algorithms, and the susceptibility of MODIS to sun glint which MISR can avoid using its off-axis cameras. When AOD retrievals are aggregated into gridded monthly products, the agreement is noticeably worse, with MODIS Terra biased high and MISR biased low relative to ground-based AERONET measurements (Wei et al., 2019; Sogacheva et al., 2020; Vogel et al., 2022; Mangla et al., 2020). These biases vary regionally and seasonally, with MISR biased especially low over East Asia and MODIS Terra biased especially high over North America and the Middle East (Wei et al., 2019).

For our analysis regions, the MAM 2020 AOD of these two products differ far more than any of the preceding comparisons between products with shared algorithms (Figure 3.A.3 - Figure 3.A.5). Notably, the differences are characterized not only by systematic offsets (e.g. with MODIS consistently reading higher than MISR) but by different distribution shapes. Furthermore, the characteristics of these discrepancies vary from region to region, supporting previous reports of spatially-dependent systematic differences between the datasets.

Comparing Figure 3.A.5 with the preceding figures suggests that the bulk of the difference between different data products' raw AOD values results from systematic biases rather than to differences in sampling. Reassuringly, however, the anomalies in Figure 3.A.5 are substantially more robust than the raw values, and exhibit agreement comparable to any of the pairs of datasets with shared algorithms. Deseasonalizing effectively removes a majority of the systematic difference between datasets. This observation largely motivates our use of deseasonalized products in the main analysis.

### 3.A.2 Extended figures: dust-subtracted aerosol optical depth

This section includes supplementary figures to support the discussion in Sections 3.5.2 and 3.6. These figures include a timeseries showing the magnitude of dust-subtracted AOD in the CovidMIP models over 2015-2020 (Figure 3.A.6), and maps of the observed (Figure 3.A.7) and simulated (Figure 3.A.8) DSAOD anomalies in MAM 2020.

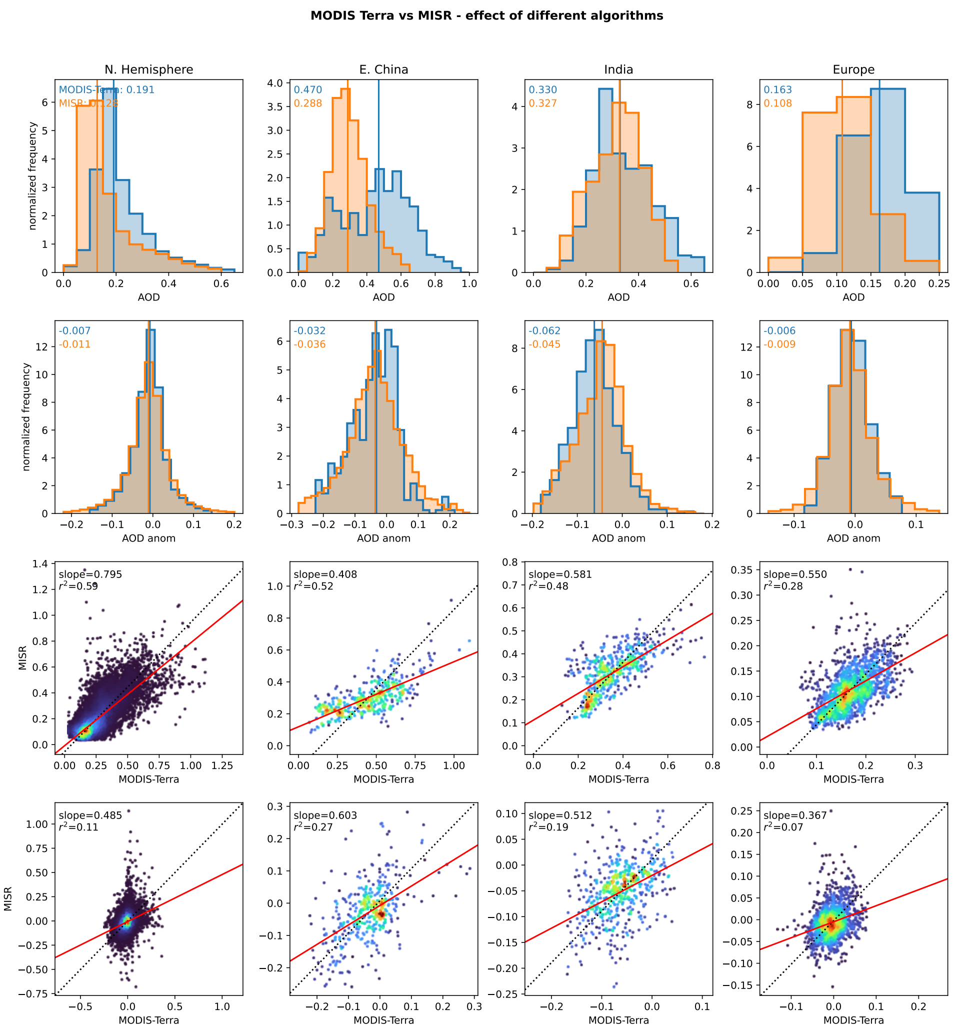


Figure 3.A.5: As Figure 3.A.2 but comparing MODIS-Terra (blue) and MISR (orange). MODIS and MISR are both on board the Terra satellite. Differences between the products therefore result from differences in detection and retrieval algorithms, as well as in the field of view.

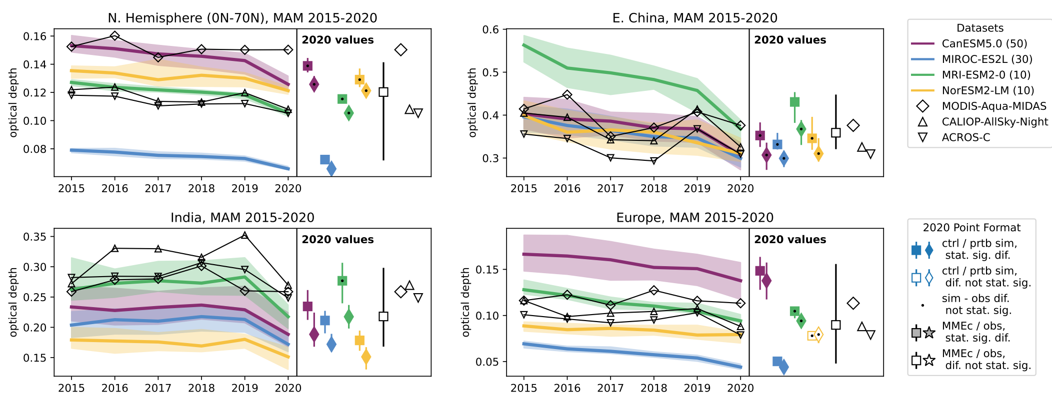


Figure 3.A.6: As Figure 3.5.2 but showing the magnitudes, not anomalies, of the dust-subtracted aerosol optical depth.

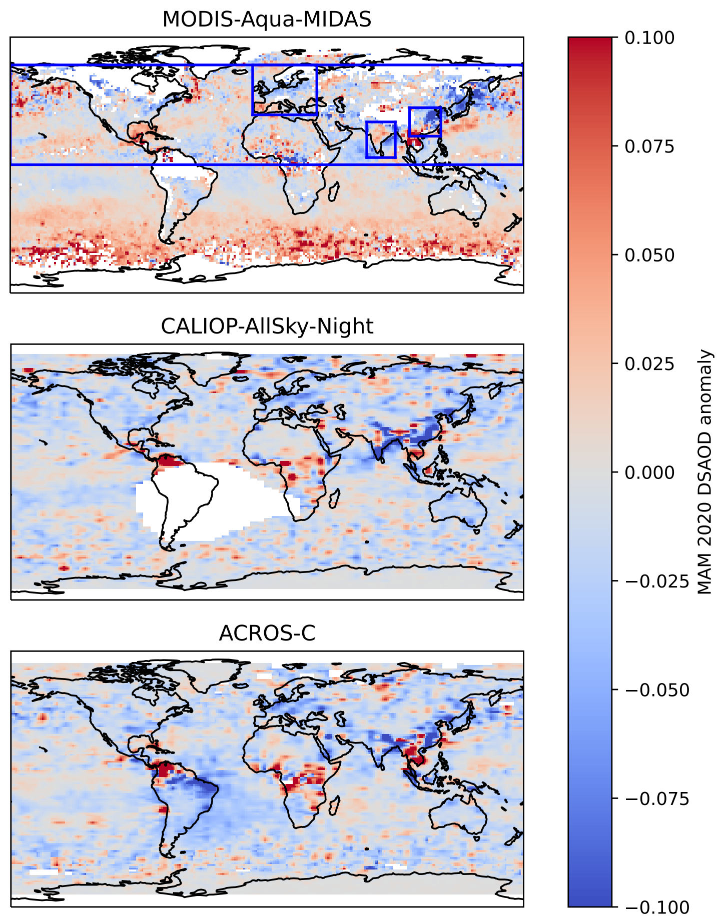


Figure 3.A.7: Observed MAM 2020 dust-subtracted AOD anomalies, relative to the 2015-2019 mean. *Top:* Total AOD from MODIS Aqua, dust from MIDAS. *Middle:* Total and dust optical depths from CALIOP AllSky Night. *Bottom*: Total and dust optical depths from ACROS-CALIOP. All maps have been interpolated to 1x1° resolution. Blue boxes in the first panel indicate the boundaries of our four analysis regions. The positive AOD anomalies over the Southern Hemisphere which are visible in the MODIS observations are due, at least in part, to the 2019/2020 Australian bushfires. CALIOP is less sensitive than MODIS to elevated smoke.

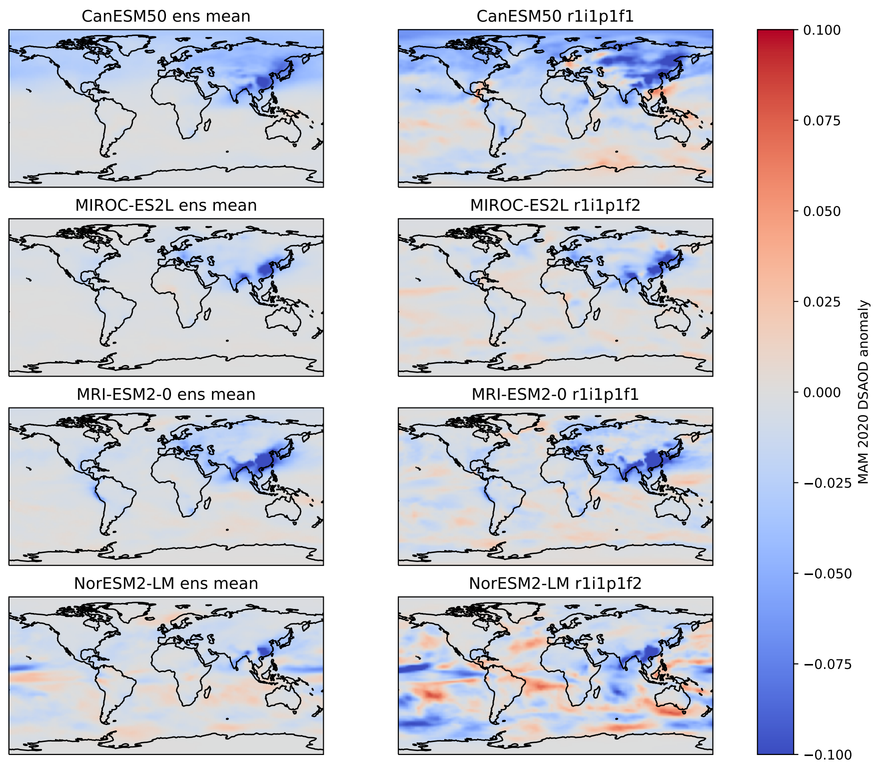


Figure 3.A.8: Simulated MAM 2020 dust-subtracted AOD anomalies, relative to 2015-2019 mean. Left-hand column shows ensemble means and right-hand column shows the first realization of each ensemble. Rows correspond to the four CovidMIP models from our main analysis. All maps have been interpolated to 1x1° resolution. Note that even single realizations are smoother than the observed optical depth fields (Figure 3.A.7), as discussed in Section 3.6.

### 3.A.3 Sensitivity tests: technical details and further analysis

#### Construction of aerosol emission inventories

We construct updated aerosol emission inventories for both anthropogenic and biomass-burning emissions of black carbon (BC), organic carbon (OC), and sulfur dioxide ($SO_2$), for the period 2013-2020. Gridded monthly anthropogenic emissions for 2013-19 were taken from the 2021-04-21 release of the Community Emissions Data System (CEDS) emission inventory (Smith et al., 2021); the 2016-07-16 release, described in Hoesly et al. (2018), was used for the historical period in CMIP6. For 2020, we set control emissions to repeat the 2019 emissions, and create a COVID-19-perturbed dataset by applying the same percentage reduction to these control emissions as was applied to the SSP2-4.5 emissions in the original CovidMIP experiment. For simplicity we do not perturb the aviation emissions. Although aviation was dramatically reduced during COVID-19, the aviation emissions simulated in CanAM5 contain minimal aerosol content. We also do not account for the reduction in sulfur oxide emissions from shipping which followed regulations introduced by the International Maritime Organization (IMO) in 2020 (IMO). Although the signal of this reduction has been identified in ship tracks (Watson-Parris et al., 2022), a corresponding AOD signal is not evident in our data.

Biomass burning emissions for 2013-2020 were taken from the Global Fire Emissions Database (GFED). GFED observations were used in CMIP6 from 1998 to 2014 (van Marle et al., 2017), and extending the dataset to 2020 provides a more realistic estimate than the linear projection used in SSP2-4.5.

The change in accumulated aerosol emissions over the 2015-2019 reference period between the original and updated inventories is shown in Figure 3.A.9. Reductions in anthropogenic emissions are dominated by changes prior to 2015 [1]. Following 2015, emissions of anthropogenic BC and OC follow similar or somewhat less negative trends to those from SSP2-4.5, albeit at a lower magnitude. In East China, SO2 emissions decrease more rapidly over 2015-2017 in the updated inventory than in SSP2-4.5, but then flatten out over the remainder of the reference period. Because all three species' emission changes are dominated by reductions in China, this same behaviour is seen in Northern Hemispheric and global mean SO2 emissions. The impacts of these reduced emissions on total AOD and aerosol radiative forcing over 1990-2019

[1] https://github.com/JGCRI/CEDS/blob/master/documentation/Version_comparison_figures_v_2021_02_05_vs_v_2016_07_16(CMIP6).pdf

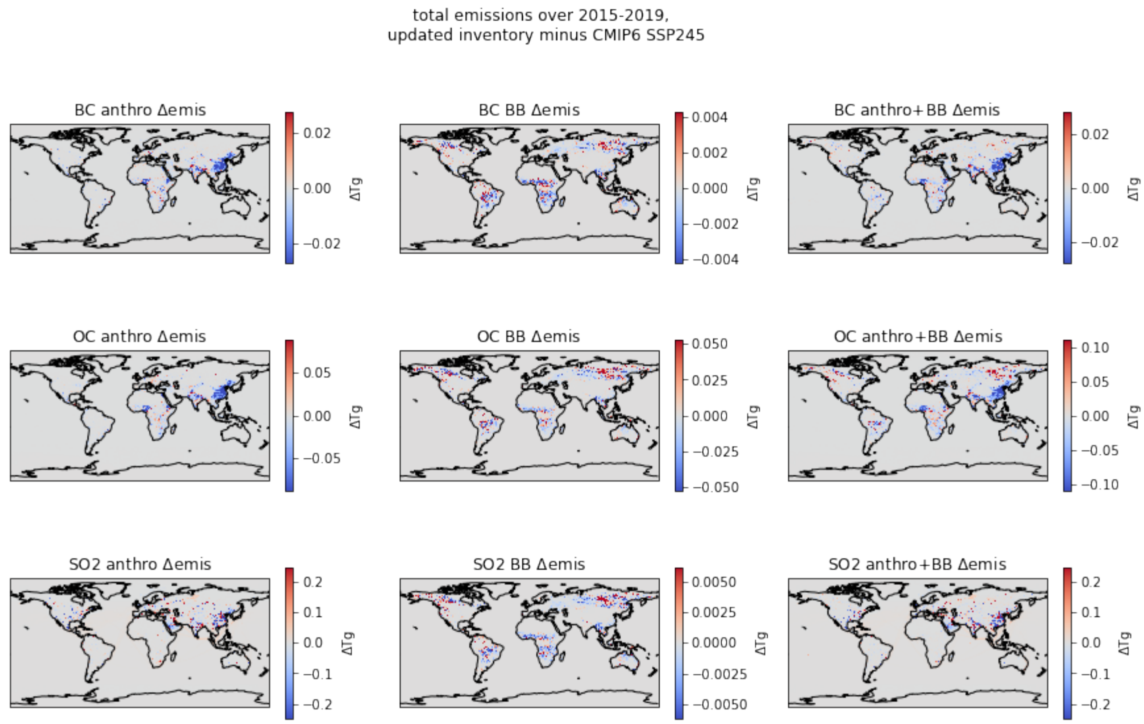


Figure 3.A.9: Changes in the accumulated emissions of BC, OC, and SO2 over 2015-2019 when updating from SSP2-4.5 emissions to the latest CEDS historical emissions (v2021-04-21) and GFED biomass burning emissions, decomposed into the changes in anthropogenic, biomass burning, and total emissions. Of our four analysis regions, only in the Northern Hemisphere and only for OC are biomass burning emissions comparable in magnitude to those from anthropogenic sources.

have been recently investigated by Lund et al. (2023), who identify decreased AOD and improved agreement with observations over this time period when using the more recent inventories.

**Model description: CanAM-new-emis and CanAM-new-emis-ndgd**

CanAM-new-emis and CanAM-new-emis-ndgd were set up identically except that CanAM-new-emis-ndgd was nudged to ERA5 reanalysis (details below). The two sets of simulations are in most ways identical to the original CanESM5 experiment, except for ensemble size (10 realizations instead of 50), the updated emissions inventories, a tracer-transport tuning correction which prevents the formation of spurious dust storms (Sigmond et al., 2023), and the fact that CanAM5 is not a coupled model. Instead, sea surface temperatures and sea ice concentrations are specified using the NOAA OI SST V2 High Resolution Dataset (Reynolds et al., 2002), and sea ice masses for the Northern and Southern Hemispheres are taken from PIOMAS (Zhang and Rothrock, 2003) and ORAP5 (Zuo et al., 2017) respectively.

The control ensembles were initialized in 2013 and run until 2020, with the first two years discarded as spin-up, and the COVID-19-perturbed simulations were branched in January 2020 as was done in the original CovidMIP experiment.

In CanAM-new-emis-ndgd, the simulated temperature, wind, and humidity fields were nudged toward the corresponding reanalysis fields using first order relaxation with a nudging timescale of 24 hours. As a result, the simulation closely reproduces the observed variation in these variables (although other parameters continue to evolve freely) and meteorologically-driven variability between the ensemble members is substantially reduced.

We additionally consider a 3-member ensemble of atmosphere-only, free-running CanAM simulations with the original SSP2-4.5 emissions ("CanAM-old-emis") in order to disentangle the effects of model configuration and emission inventory when comparing CanESM5 and CanAM-new-emis (Figure 3.A.10).

The effects of model configuration, emissions inventory, and nudging to ERA5 reanalysis on DSAOD magnitudes are illustrated in Figure 3.A.11 (MAM means) and Figure 3.A.12 (annual means). We do not show the change in total AOD due to the aforementioned issue with mineral dust in CanESM5. Because this issue was corrected in the CanAM5 runs shown here, there is a substantial difference between the total AOD simulated by CanESM5 and CanAM-new-emis which is unrelated to the updated emissions inventories.

In all regions, both springtime and annual-mean DSAOD are lower in CanAM-new-emis than in the original CanESM5 CovidMIP ensemble. In China the emission reductions dominate the difference, whereas model configuration has a larger effect in Europe. The changes are overall small in India in the spring, resulting in the similarity between 2020 anomalies simulated by CanESM5 and CanAM-new-emis that was seen in Figure 3.5.3, but emission reductions are more important when considering annual means. When the Northern Hemisphere is considered as a whole, emission reductions and model configuration have similar impacts on DSAOD magnitude. Analysis of both these simulations and a larger ensemble of historical simulations (averaged over 2000-2014, not shown) indicates that the reduction caused by model configuration is systematic, and so AOD anomalies can be directly compared between model configurations. The results of nudging to ERA5 reanalyses are mixed, but generally the magnitude of the simulated AOD is either unaffected or somewhat increased relative to CanAM-new-emis. The interannual variability tends to increase as well, in some cases beyond the ensemble spread simulated by CanAM-new-emis.

Whether changes to the inventory and/or simulated meteorological conditions improve agreement between the magnitude or variability of the observed and simulated optical depth fields depends on the region in question and, for the Northern Hemisphere, on which satellite is considered. The existing discrepancies likely stem from errors in both the observed and simulated fields, and the relative magnitudes of these biases will change from region to region. It is also important to note that CanAM5 does not have a separate set of parameter tunings for use with nudged simulations. Model parameters are tuned to produce realistic climatological aerosol properties in the free-running simulation. If there are typically biases in the free-running temperature, wind, or humidity fields, the tuning will compensate for these. As a result the model may simulate unrealistic aerosol properties when presented with a more realistic meteorological field.

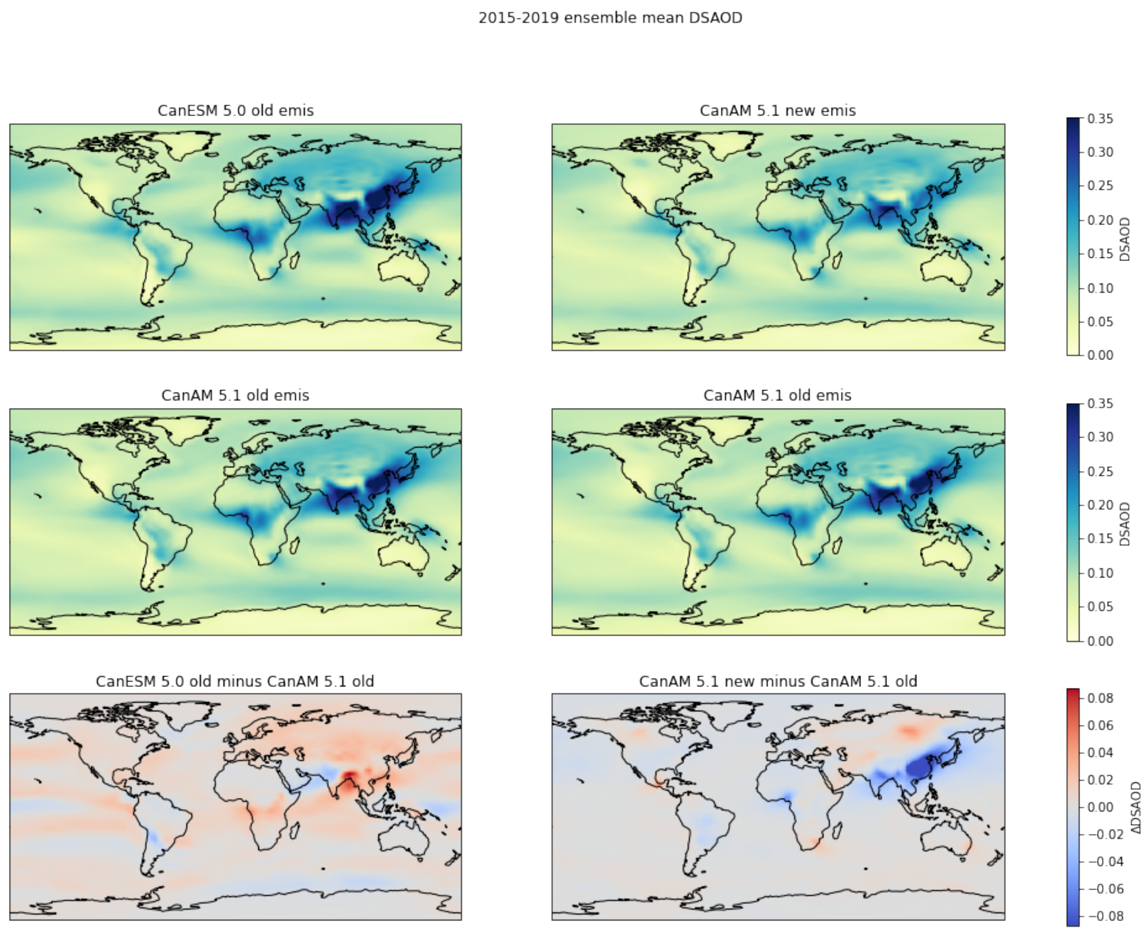


Figure 3.A.10: Comparison between ensemble-mean DSAOD, averaged over the 2015-2019 reference period, in three sets of simulations: CanESM5 (upper left), CanAM-new-emis (upper right), and CanAM-old-emis (centre row, both columns). The bottom row shows the DSAOD differences between pairs of ensembles, demonstrating the effects of model configuration (coupled vs atmosphere-only, left column) and emission inventory (SSP2-4.5 vs CEDS v2021-04-21 and GFED biomass burning, right column) on simulated DSAOD.

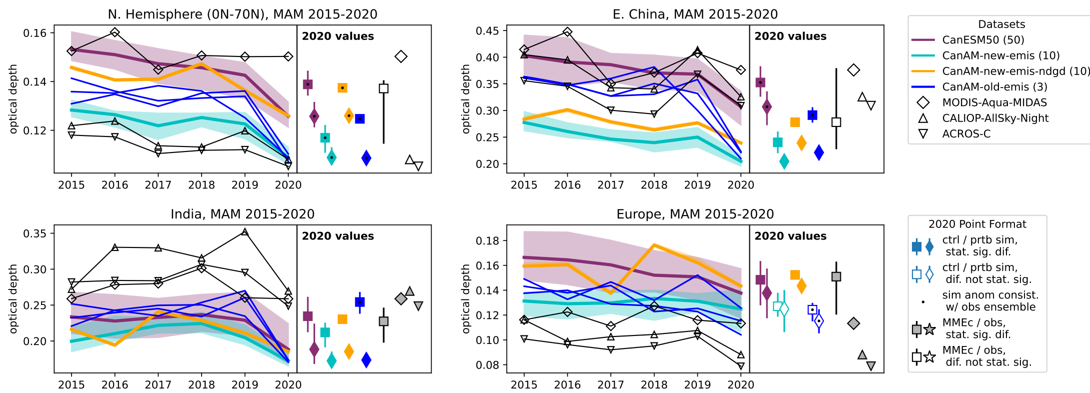


Figure 3.A.11: Comparison between the dust-subtracted AOD values (not anomalies) over MAM 2015-2020 as simulated by CanESM5, CanAM-old-emis (atmosphere-only, original emissions inventories), CanAM-new-emis (atmosphere-only, updated emissions inventories), and CanAM-new-emis-ndgd (atmosphere-only, updated inventories, and nudged to ERA5 temperature, wind, and humidity fields). Because there are only 3 realizations of CanAM-old-emis, they are shown as individual lines instead of an ensemble median and 5-95% spread as for the other simulations.

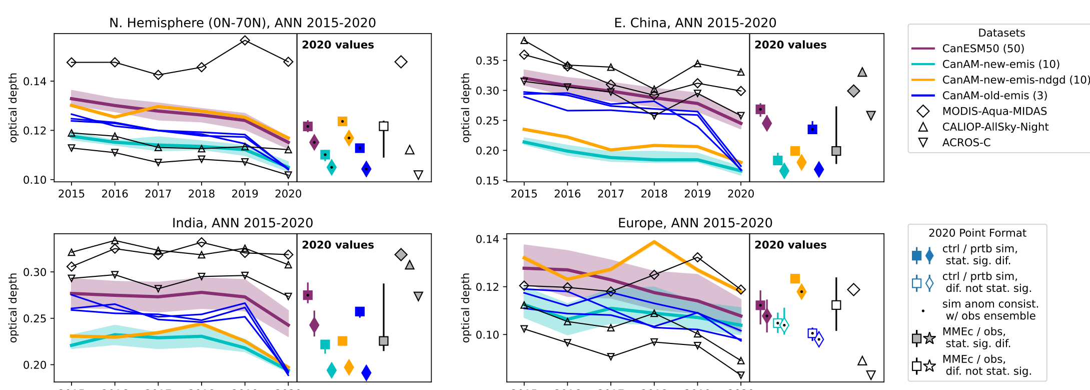


Figure 3.A.12: As Figure 3.A.11 but for annual means.

# Chapter 4

# The Refractive Index of Black Carbon

The radiative forcing of black carbon (BC) is subject to many complex, interconnected sources of uncertainty. Here we isolate the role of the refractive index, which determines the extent to which BC absorbs and scatters radiation. With other parameterizations held constant, varying BC's refractive index from $m_{550nm} = 1.75-0.44i$ to $m_{550nm} = 1.95-0.79i$ increases simulated absorbing aerosol optical depth (AAOD) by 42% and the effective radiative forcing from BC-radiation interactions (BC ERFari) by 47%. The AAOD increase is comparable to that from recent updates to aerosol emission inventories, and in BC source regions, a third as large as the difference in AAOD retrieved from MISR and POLDER-GRASP satellites. The BC ERFari increase is comparable to the scale of the uncertainty in recent literature assessments. Although model sensitivity to the choice of BC refractive index is modulated by other parameterization choices, our results highlight the importance of considering refractive index diversity in model intercomparison projects.

The contents of this chapter have been submitted for consideration in Geophysical Research Letters as *The impact of uncertainty in black carbon's refractive index on simulated optical depth and radiative forcing.*

## 4.1 Introduction

Black carbon (BC), formed as a result of incomplete combustion, is the most strongly warming of the aerosols (Szopa et al., 2021), with particularly important impacts in the Arctic (AMAP, 2021; Sand et al., 2016; von Salzen et al., 2022). Although its effective radiative forcing (ERF; Boucher et al. (2013)) is understood to be positive, the magnitude of this forcing remains uncertain (AMAP, 2021; Bond et al., 2013; Szopa et al., 2021; Thornhill et al., 2021).

This uncertainty stems from many sources, including uncertainty in the optical properties of freshly emitted BC (Bond and Bergstrom, 2006; Bond et al., 2013; Liu et al., 2020) and the changes in these properties as BC ages (Hu et al., 2023; Peng et al., 2016; Taylor et al., 2020); in the total burden and vertical distribution of BC (Gliß et al., 2021; Samset et al., 2013; Sand et al., 2021), which are themselves complicated by uncertainties in the emissions (Bond et al., 2013; Hoesly et al., 2018; Wang et al., 2021) and lifetime (Gliß et al., 2021; Hodnebrog et al., 2014; Lund et al., 2018) of BC; and uncertainty in the details of BC-cloud interactions (Koch and Del Genio, 2010; Szopa et al., 2021; Zanatta et al., 2023).

Constraining these uncertainties is complicated by the fact that models and observations frequently disagree, but it is not always clear which – if either – is correct (Samset et al., 2018b). For example, models tend to simulate lower absorption aerosol optical depth (AAOD) than is measured by AERONET stations (Bond et al., 2013; Samset et al., 2018b; Sand et al., 2020). This can be interpreted to mean that models underestimate AAOD, perhaps because of too-low emissions or too-vigorous removal (Bond et al., 2013) or because the simulated aerosols are insufficiently absorbing (Bond and Bergstrom, 2006; Liu et al., 2020). Alternatively it could indicate that AERONET overestimates AAOD, as suggested by Andrews et al. (2017) based on comparisons between AERONET and in-situ aircraft measurements. It is also possible that both models and observations are reasonably accurate, and that the apparent discrepancy comes from comparing point-source measurements of a very spatially heterogeneous quantity against model grid cell averaged fields (Schutgens et al., 2021; Wang et al., 2016, 2018).

In this work we investigate the sensitivity of BC AAOD and radiative forcing to one key source of uncertainty: the complex refractive index, which determines the degree to which an aerosol absorbs and scatters radiation. Lab-based estimates of the BC refractive index (BCRI) show remarkable diversity (Bond and Bergstrom, 2006) and this diversity is reflected in the range of values commonly used in Earth system models (Table 4.2.1). Recent studies (Sand et al., 2021; Gliß et al., 2021) suggest that uncertainty in the choice of BCRI may, along with uncertainties in the treatment of mixing and ageing, contribute to the diversity in BC absorption simulated by Earth system models; however, no study has to date isolated the impact of BCRI on key BC fields in a single model with other aerosol treatments held constant. Here we select three values of the BCRI commonly used in Earth system models, summarized below, and use them to run otherwise-identical ensembles of simulations in the atmospheric model CanAM5.1-PAM. We then contextualize the resulting spread in climate-relevant quantities including AAOD and the effective radiative forcing from aerosol-radiation interactions (ERFari) by comparing with a sample of other known uncertainties.

## 4.2 Parameterizations of the Refractive Index

The refractive index $m = n - ik$ is a complex, wavelength-dependent parameter that determines the extent to which an aerosol absorbs or scatters radiation. It cannot be measured directly but is inferred by fitting laboratory measurements to an assumed optical model, such as Mie theory or Rayleigh-Debye-Gans theory, that describes the optical properties of an aerosol as a function of refractive index. For BC, these may be measurements of the scattering and absorption of light by flame-generated BC particles or of the reflectance at different angles by a compressed BC sample (Bond and Bergstrom, 2006). In either case, measurements are typically taken at only one or a few wavelengths, so additional assumptions are required to extrapolate the full spectrally-dependent refractive index.

Uncertainty can arise from the measurements themselves, from the applicability of the assumed optical model to the BC sample being measured, and from the representativity of this BC sample to the BC which one aims to describe. For instance, measurements of scattering and absorption by flame-generated particle may be fit to Mie theory (assuming spherical particles) or Rayleigh-Debye-Gans theory (assuming aggregates). If the particles being measured are aggregates but Mie theory is assumed, not only will the scattering and absorption be underpredicted, but the inferred BCRI will be for a combination of pure BC and the air contained within the aggregates' voids (Bond and Bergstrom, 2006). Furthermore, the inferred BCRI will be for BC generated by a simple, clean laboratory flame, which likely has a different temperature history – and thus, generates BC particles with different optical and structural properties – than the more complex sources that generate most atmospheric BC (Bond and Bergstrom, 2006). To complicate matters further, there is ambiguity in what precisely constitutes BC: for instance, some authors use the terms *BC* and *soot* interchangeably while others consider them to be separate materials. An extensive review of these uncertainties is provided by Bond and Bergstrom (2006).

In this work we select three values of the BCRI from the literature, quoted here at 550 nm: $m_{550nm} = 1.75 - 0.44i$ (d'Almeida et al., 1991), $m_{550nm} = 1.75 - 0.63i$ (Bond and Bergstrom, 2006), and $m_{550nm} = 1.95 - 0.79i$ (Bond and Bergstrom, 2006), described below. We will refer to these selections as the *low, medium,* and *high* BCRI respectively, based on their values of the absorption function $E(m)$ at 550nm:

$$E(m) = \mathrm{Im}\left(\frac{m^2 - 1}{m^2 + 2}\right) \tag{4.2.1}$$

(Bohren and Huffman, 1983). Higher values of $E(m)$ indicate an increased tendency for absorption, and the mass absorption cross section of an aerosol is a linear function of $E(m)$ although the details of this relationship depend on aerosol morphology (Liu et al., 2020). The three BCRI used here have $E(m_{550nm})$ of 0.177, 0.248, and 0.255 respectively. Their absorption functions are approximately constant through the mid-visible range and increase to both the ultraviolet and infrared, with the difference in absorption between the three BCRI increasing in both directions (d'Almeida et al., 1991; Chang and Charalampopoulos, 1990).

**Low BC Refractive Index:** $m_{550nm} = 1.75 - 0.44i$

Use of the "low" BCRI can be tracked to back to the 1970s at least. d'Almeida et al. (1991) tabulated the refractive indices of dust-like, water-soluble, soot, oceanic, sulfate, and mineral aerosol components at wavelengths from 0.300-40 microns. The refractive indices of soot, which is frequently used as interchangeable with BC, were drawn from the tabulation of Shettle and Fenn (1979) which itself compiled data from pre-existing measurements.

More recent evidence (Bond and Bergstrom, 2006; Liu et al., 2020) suggests that the BCRI proposed by d'Almeida et al. (1991) is inconsistent with observations, and that the corresponding absorption is too low. Nevertheless, this BCRI has been very widely used in the climate modeling community (Table 4.2.1) and it is the default BCRI in CanAM5.1-PAM, described below.

**Medium and High BC Refractive Indices:** $m_{550nm} = 1.75 - 0.63i$ **and** $m_{550nm} = 1.95 - 0.79i$

Bond and Bergstrom (2006) compiled and reviewed laboratory measurements of the optical properties of BC, and from these data, proposed a range of BCRI values lying along the so-called "void fraction line." These BCRI describe the effective refractive indices of BC with varying degrees of air included within its structure. We select $m_{550nm} = 1.75 - 0.63i$ and $m_{550nm} = 1.95 - 0.79i$, the lowest and highest values proposed by Bond and Bergstrom (2006), for this analysis.

Unlike d'Almeida et al. (1991), Bond and Bergstrom (2006) only provide estimates of the BCRI at 550nm. Flanner et al. (2012) obtained full spectral information for $m_{550nm} = 1.95 - 0.79i$ using the expressions derived by Chang and Charalampopoulos (1990). We use this dataset for our "high" BCRI, and apply an equivalent scaling to the equations of Chang and Charalampopoulos (1990) to obtain the spectrally varying "medium" BCRI for $m_{550nm} = 1.75 - 0.63i$.

The "high" BCRI is used by a number of aerosol schemes. To our knowledge, no schemes currently use our "medium" BCRI, although some use intermediate values from Bond and Bergstrom (2006), most commonly $m_{550nm} = 1.85 - 0.71i$ (Table 4.2.1). Nevertheless we select $m_{550nm} = 1.75 - 0.63i$ as our intermediate BCRI in order to span the range of estimates from Bond and Bergstrom (2006).

## 4.3 Methods

Simulations are conducted with the Canadian Atmospheric Model version 5.1 (CanAM5.1; Cole et al. (2023); Sigmond et al. (2023)) using the Piecewise Lognormal Approximation (PLA) Aerosol Model (PAM; von Salzen (2006)). A detailed description of CanAM5.1-PAM can be found in Appendix 4.A.1.

We simulate three sets of "core ensembles": one control ensemble and one perturbed ensemble for each of the BCRI described above. Each ensemble consists of nine short simulations (2014-2019) and one long simulation (1949-2019). The first year of each is discarded as spinup. In the control ensemble, all emissions of aerosols and greenhouse gases are transient; in the perturbed ensemble, all emissions are transient except for BC which is set to 1850 levels. ERF is then calculated from the difference in top of atmosphere flux between pairs of control and perturbed runs, following the "ERF_trans" method of Forster et al. (2016). Finally, the total BC

| Aerosol scheme | Host model | References |
|---|---|---|
| Low RI ($m_{550nm} = 1.75 - 0.44i$) | | |
| AM4.0 | GFDL | Zhao et al. (2018) |
| CLASSIC | ACCESS-ESM1-5, HadGEM2-ES | Bellouin et al. (2011); Ziehn et al. (2020) |
| GOCART | GEOS | Chin et al. (2002); Colarco et al. (2010) |
| SPRINTARS | MIROC-ES2L | Takemura et al. (2002); Hajima et al. (2020) |
| (unnamed) | OsloCTM3 | Myhre et al. (2009a) |
| PAM | CanAM5.1-PAM | von Salzen (2006); Cole et al. (2023) |
| High RI ($m_{550nm} = 1.95 - 0.79i$) | | |
| ATRAS | CAM5-ATRAS | Matsui (2017) |
| MAM4 | CESM1, E3SM-1-1 | Liu et al. (2012); Wang et al. (2019) |
| MASINGAR | MRI-ESM2-0 | Yukimoto et al. (2019) |
| OsloAero6 | NorESM2-LM | Seland et al. (2020) |
| Alternate recommendation from Bond and Bergstrom (2006) ($m_{550nm} = 1.85 - 0.71i$) | | |
| GLOMAP | UKESM | Sellar et al. (2019) |
| HAM-M7 | ECHAM-HAM | Tegen et al. (2019) |
| SALSA | ECHAM-SALSA | Bergman et al. (2012) |
| TM5-mp3.0 | EC-Earth3-AerChem | van Noije et al. (2021)) |

Table 4.2.1: Illustrative sample of aerosol schemes that use our selected BCRI; see **??** for descriptions of the indices. To the best of our knowledge no aerosol schemes currently use our intermediate-absorption BCRI ($m_{550nm} = 1.75 - 0.63i$), the lowest value recommended by Bond and Bergstrom (2006). However, a number of aerosol schemes use $m_{550nm} = 1.85 - 0.71i$, an alternate recommendation from Bond and Bergstrom (2006) that falls between our intermediate and high BCRI, and we include a selection of those schemes here.

ERF is decomposed into contributions from aerosol-radiation (ERFari), aerosol-cloud (ERFaci), and albedo (ERFalb) interactions following Ghan (2013). In this work we exclusively consider shortwave ERF. Longwave BC ERF is small in CanESM5.1-PAM, consistent with previous findings for models that do not parameterize aerosol impacts on ice and mixed phase clouds (Heyn et al., 2017). Although PAM includes representations of the albedo effects on BC deposited on snow and ice (Namazi et al., 2015) and absorption of solar radiation by BC-containing cloud droplets (Li et al., 2013), in this work we only vary the refractive index of atmospheric BC. ERFaci and ERFalb are thus expected to be similar between the three core ensembles.

The influence of the BCRI on AAOD, ERFari, and tropospheric temperature are quantified by comparing these fields between the three core ensembles. We then compare the changes in ensemble-median AAOD and ERFari that arise from the choice of BCRI to the variation that can be obtained from other uncertain factors. This comparison is not intended as a comprehensive analysis of BC uncertainties, but rather presents an illustrative sample of relevant uncertainties other than BCRI.

Our first comparison investigates the impact that recent updates to aerosol emission inventories have on simulated AAOD. In the core ensembles, anthropogenic aerosol emissions are taken from the Community Emissions Data System (CEDS) 2021-04-21 release (Smith et al., 2021). CEDSv2021 emissions not only extend the historical emissions used in CMIP6 to more recent years but also include several back-corrections, most notably reducing the emissions of BC, organic carbon, and sulfur dioxide over China (Smith et al., 2021; Wang et al., 2021). Biomass burning emissions in the core ensembles are taken from the CMIP6 historical inventory for 1950-2014 and the Global Fire Emissions Database (GFED v4.1s; van der Werf et al., 2017) for 2015-2019. To investigate the impact of these selections, we run a single simulation forced with the more commonly used CMIP6 historical and SSP2-4.5 anthropogenic and biomass burning emissions, otherwise identical to the low-absorption core ensemble. We compare the AAOD from this simulation against each realization of the low-absorption ensemble in turn, yielding a 9-member ensemble of differences. We emphasize that this comparison does not represent the total uncertainty in either anthropogenic or biomass-burning aerosol emissions, as we are comparing two versions of the same anthropogenic emissions inventory and extending the biomass burning emissions with the same observational product as was used in the creation of the CMIP6 historical and SSP inventories. Instead this comparison shows the sensitivity of AAOD to recent improvements in both sets of emissions.

Our second comparison considers observational uncertainty. We compare estimates of AAOD from the Multi-angle Imaging SpectroRadiometer (MISR, Diner et al. (1998)) and the Polarization and Directionality of the Earth's Reflectances instrument with the Generalized Retrieval of Atmosphere and Surface Properties algorithm (POLDER-GRASP, Dubovik et al. (2011)), selected for their availability in Level 3 gridded format. MISR and POLDER-GRASP bracket the range of AAOD simulated by current Earth system models (Figure 4.A.1). We consider satellite observations rather than ground-based or in-situ measurements due to the challenge in comparing point-source data against gridded model results (Wang et al., 2016, 2018; Schutgens et al., 2021). POLDER-GRASP data are not available for the 2015-2019 study period, so we instead compare these satellites over the 5-year period 2007-2011. The difference between MISR results for 2015-2019 and 2007-2011 is substantially smaller than the difference between MISR and POLDER-GRASP data for 2007-2011, indicating that use of these alternate years is unlikely to affect our conclusions. This comparison is not intended to be a detailed evaluation of the uncertainty in remotely-sensed AAOD; such assessments can be found in, for example, Schutgens et al. (2021). Instead it provides an estimate of the range of AAOD that can be obtained from different instruments. As such it does not account for differences in sampling between the two satellites or between the observed and simulated AAOD fields.

Our final comparison considers the range of AAOD and ERFari reported in recent multimodel assessments from the literature. This comparison folds in many sources of model uncertainty, including differences in the treatment of mixing state which has been shown to have substantial impact on simulated BC absorption (Sand et al., 2021; Glıß et al., 2021), as well as differences in the parameterization of aerosol transport and deposition. The individual assessments are described in Section 4.4.

## 4.4 Results

### 4.4.1 Absorption Aerosol Optical Depth

Modifying the BCRI directly modifies BC absorption, and we thus begin by assessing the its impact on AAOD (Figure 4.4.1). By changing from the low to medium (high) BCRI, global-mean 2015-2019 AAOD increases by $8.09 \times 10^{-4}$ or 27% ($1.26 \times 10^{-3}$ or 42%). Absolute increases are, unsurprisingly, largest over major source regions, but

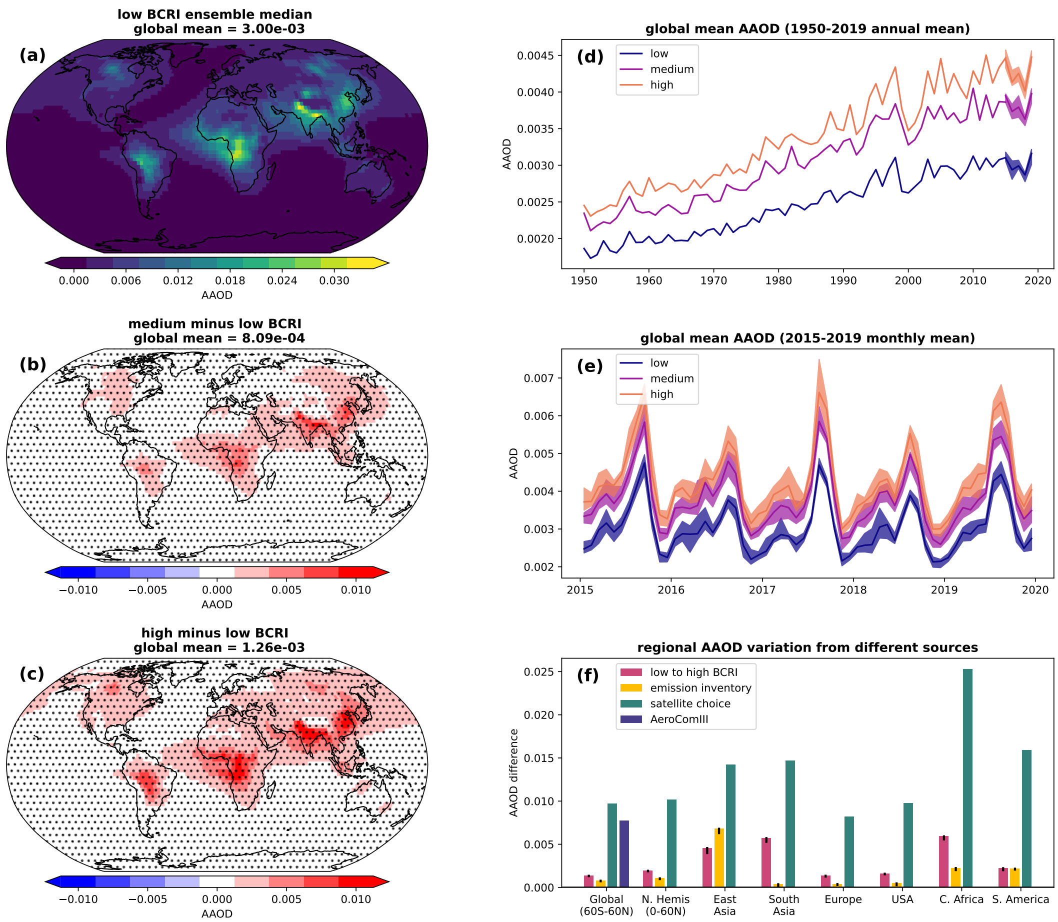


Figure 4.4.1: Maps show ensemble-median, 2015-2019 mean AAOD in **(a)** the low-absorption ensemble, **(b)** medium minus low absorption ensemble, **(c)** high minus low absorption ensemble. Stippling in **(b)** and **(c)** indicates regions where the difference between time-averaged ensembles is statistically significant at the 5% level according to a two-sided Students t-test; the global-mean AAOD difference is statistically significant for both medium- and high-absorption ensembles. Timeseries show global-mean AAOD in the low (purple), medium (magenta), and high (orange) absorption ensembles, over **(d)** 1950-2019 and **(e)** 2015-2019. Panel **(f)** compares the difference in ensemble-median, 2015-2019 mean AAOD between low and high absorption ensembles (dark pink) to the spread in AAOD obtained from simulations using different emission inventories (gold) and to the range in remotely-sensed AAOD from different satellites (teal) in 8 different geographic regions, and to the overall range in AAOD from AeroCom Phase III models (Sand et al., 2021) for the near-global region only (indigo). Shaded envelopes in panels **(d)** and **(e)**, and error bars in panel **(f)**, denote the 5th-95th percentile range across ensembles.

both medium- and high-absorption ensembles are statistically significantly different from the low-absorption ensemble everywhere (Figure 4.4.1b, c). There is no overlap between the low- and medium- or high-absorption ensembles of global-mean AAOD (Figure 4.4.1d,e), and as absorption increases, so too does the magnitude of the trend in AAOD over 1950-2019 (Figure 4.4.1d).

Figure 4.4.1f compares the regional increases in AAOD from varying the BCRI to the increases obtained by varying the aerosol emissions and to the differences in observed AAOD from the MISR and POLDER-GRASP satellites. Region definitions are provided in Table 4.A.1 and Figure 4.A.2. The "near-global" and "Northern Hemisphere" domains exclude latitudes poleward of 60° where the satellite retrievals are poorly sampled. Most of the regional variation in the increase of AAOD caused by varying the BCRI comes from differences in the local BC burden (Figure 4.A.2); the relative increase is fairly consistent, varying from 39-47%.

The choice of aerosol emission inventory has the greatest impact in regions where the two inventories are the most different and where the baseline emissions are high. The largest emissions-based AAOD increase, both in absolute terms and relative to the BCRI increase, occurs in East Asia where both conditions are satisfied; the smallest occurs in South Asia where the two inventories are nearly identical. These increases are a factor of 1.5 larger than, and a factor of 16 smaller than, the BCRI increases respectively; the 60°S-60°N average is approximately 60% of the BCRI increase. Note that these values do not indicate the overall uncertainty in global or local emissions, only the spatial distribution of updates to the inventories being considered. For example, Pan et al. (2020) report a factor of seven difference in Southeast Asian biomass burning emissions from different inventories (a more accurate representation of emission uncertainties in this region), whereas we see almost no change between the inventory versions considered in this assessment.

In all regions the range of AAOD between different satellites is substantially larger than the range of simulated AAOD in CanAM5.1-PAM under different configurations. This is expected given the challenges in constraining remotely sensed AAOD (Samset et al., 2018b). Even so, in regions where the BC burden is high the impact of BCRI on AAOD can be as much as a third as large as the difference between satellites. Averaged over the near-global domain, the inter-satellite discrepancy is a factor of seven larger than the BCRI-based AAOD increase. The satellite differences will be largest in regions where characteristics of the geography increase retrieval uncertainty (e.g. regions with more reflective surfaces) and in regions where the satellites differ in their sensitivity to the dominant aerosol type.

Finally, for the near-global domain only we compare with the spread in global-mean AAOD from AeroCom Phase III models (Sand et al., 2021). AeroCom Phase III estimates of the global-mean AAOD in simulations forced with 2010 emissions range from $2.04 \times 10^{-3}$ to $9.78 \times 10^{-3}$ for an overall range of $7.75 \times 10^{-3}$ or approximately 6 times that obtained by varying the BCRI alone. This is similar to the range of AAOD between satellites, and as shown in Figure 4.A.1, the distribution of zonal-mean AeroCom Phase III AAOD is approximately bracketed by the zonal-mean AAOD from MISR and POLDER-GRASP. The 15 AeroCom models have BCRI spanning between our low and high values, but the BCRI alone does not explain the intermodel spread, as discussed further in Section 4.5.

Overall, the sensitivity of simulated AAOD to the choice of BCRI is comparable to its sensitivity to recent updates to the aerosol emission inventory within the same model. Between models, or between satellites, the AAOD spread is a factor of 6 to 7 larger.

Despite the fact that BC generally makes up a small fraction of total aerosol extinction (Bond et al., 2013), we do see regionally significant increases in total AOD when BC absorption is increased (Figure 4.A.3). These changes are particularly evident in Central and South Africa, South America, and the northern latitudes. These are all regions with high emissions from biomass burning, which are associated with a higher ratio of BC emissions. Heavily polluted regions, such as South and East Asia, do not show an AOD dependence on BCRI, likely because AOD in these regions is dominated by sulfate. There is not a statistically significant difference between globally-averaged AOD in the three core ensembles.

### 4.4.2 Aerosol-Radiation Forcing

The BCRI directly affects the interaction of BC with incoming solar radiation and therefore the aerosol-radiation forcing ERFari. Figure 4.4.2 summarizes the variation in shortwave BC ERFari across our three ensembles.

Changing from the low to medium (high) BCRI increases global-mean BC ERFari from 0.19 W/m$^2$ to 0.25 W/m$^2$ (0.28 W/m$^2$), an increase of 32% (47%). These increases are largely confined to the Northern Hemisphere, and for the high-absorption ensemble, are statistically significant in most regions where the low-absorption BC ERFari is significantly nonzero (Figure 4.4.2c). Global-mean BC ERFari in both

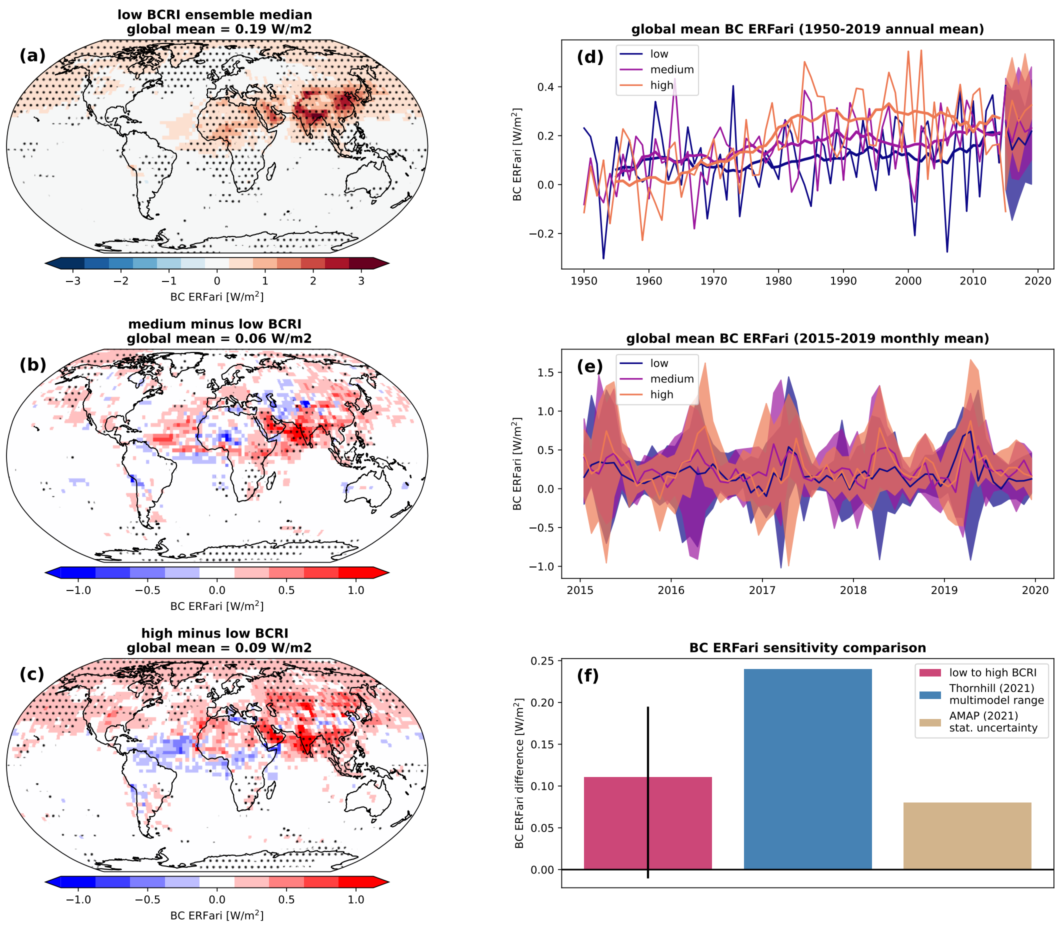


Figure 4.4.2: Panels **(a-e)**: as Figure 4.4.1 but for BC ERFari. Heavy lines in **(d)** show 11-year rolling means. Panel **(f)** compares the difference in BC ERFari between low and high absorption ensembles to the multimodel range from the Thornhill et al. (2021) assessment (blue), and to the statistical uncertainty in the AMAP (2021) assessment (tan). The global-mean increase of 0.09 W/m$^2$ referenced in the title of panel **c** does not match the median increase of 0.11 W/m$^2$ shown in panel **f** because panel **c** shows the difference between ensemble medians, whereas panel **f** shows the ensemble distribution of global-mean differences between individual realizations.

the medium- and high-absorption ensembles are significantly different from the low-absorption level at the 5% level. There is more interannual variability in the timeseries of global-mean BC ERFari than there is in AAOD, likely due to the dependence of ERFari on cloud fields (Figure 4.4.2d,e). Despite this variability, ERFari trends over 1950-2019 increase with BCRI as the AAOD trends do.

The uncertainty in BC ERFari attributable to the choice of BCRI can be compared to results from two recent literature assessments. We first compare with the multimodel range of BC ERFari assessed by Thornhill et al. (2021), and then with the statistical uncertainty in BC ERFari reported by the Artic Monitoring and Assessment Program (AMAP) 2021 report. We emphasize that these are fundamentally different quantities with different interpretations. Furthermore, Thornhill et al. (2021) and AMAP (2021) estimate ERF for different time periods, assuming different emission inventories, and using different methodology in their calculations, so the studies' best estimates are not directly comparable to our results or to each other. The comparisons are nevertheless useful in contextualizing how much of an impact uncertainty in the BCRI has on that of BC ERFari.

Thornhill et al. (2021) calculated ERF for numerous aerosol and greenhouse gas species for 1850-2014 based on results from AerChemMIP (Collins et al., 2017). Eight models provided estimates of total BC ERF but only four decomposed this ERF into contributions from radiation, cloud, and surface albedo forcings. These four models (CNRM-ESM2, MRI-ESM2, NorESM2, and UKESM1) simulated BC ERFari of 0.37 W/m$^2$, 0.13 W/m$^2$, 0.35 W/m$^2$, and 0.26 W/m$^2$ respectively, for an overall range of 0.24 W/m$^2$. This is a factor of 2.5 larger than the difference in ERFari simulated by our low- and high-absorption ensembles. The four models use a narrow range of high-absorption BCRI: $m_{550nm} = 1.95 - 0.79i$ (MRI-ESM2 and NorESM2), $m_{550nm} = 1.85 - 0.71i$ (UKESM), and $m_{550nm} = 1.83 - 0.74i$ (CNRM-ESM2). The assessed range thus did not stem from differences in the BCRI, although differences in the treatment of mixing states could still result in different levels of BC absorption. The results of Thornhill et al. (2021) provide the basis for the assessed BC ERFari in the latest Intergovernmental Panel on Climate Change (IPCC) assessment report, AR6 (Szopa et al., 2021); as AR6 did not itself quote an uncertainty range for BC ERFari, we do not otherwise include it in this comparison.

AMAP (2021) assessed radiative forcing for 1850-2015 using a different aerosol emission inventory than Thornhill et al. (2021). Five models contributed data for BC ERF, but only two provided the decomposition into ERFari: MRI-ESM2 and our own CanAM5-PAM, with BCRI of $m_{550nm} = 1.95 - 0.79i$ and $m_{550nm} = 1.75 - 0.44i$ respectively. The reported ERFari derived from these two models was 0.27 ± 0.04 $W/m^2$. Unlike the Thornhill et al. (2021) and AeroCom results discussed above, this ± 0.04 $W/m^2$ is an estimate of statistical uncertainty rather than a multimodel range. It represents the precision to which ERFari can be determined when derived from 100-year integrations of two Earth system models. The overall uncertainty range of 0.08 $W/m^2$ is ∼80% of the range we obtain by varying the BCRI within one model, suggesting that a different choice of BCRI in either model could have materially impacted the assessed ERFari.

Varying the BCRI, and thus the absorption, of atmospheric BC is found not to have a statistically significant impact on the aerosol-cloud forcing or total BC forcing. This experiment did not vary the BCRI within cloud droplets or when deposited on snow, so the only impact on clouds would be via the impact of changes in atmospheric temperature profiles, discussed below.

### 4.4.3 Temperature and Precipitation

Black carbon influences global and regional temperature (AMAP, 2021; Bond et al., 2013; von Salzen et al., 2022), mean and extreme precipitation (Samset et al., 2016; Samset, 2022; Sand et al., 2020), and the Asian monsoon (Ganguly et al., 2012; Li et al., 2016; Westervelt et al., 2020; Xie et al., 2020). The sensitivity of these fields to the BCRI cannot be assessed in this study as the three ensembles used the same set of prescribed sea surface temperatures. We can, however, examine temperature changes from the radiative heating of the atmosphere by BC in the mid and upper troposphere, and draw on other works to estimate potential precipitation changes.

Figure 4.4.3 illustrates the vertical distribution of temperature changes obtained by varying the BCRI. Although near-surface air temperatures are constrained by the prescribed sea surface temperatures, statistically significant zonal-mean warming is evident over the northern midlatitudes starting at about 850 hPa. At 600 hPa and above, this warming is mostly confined to regions above and downwind of East and South Asia; at lower altitudes, significant warming is also apparent over or downwind of Africa and South America. Large temperature responses are apparent at the poles in Figure 4.4.3a but note that these changes are not statistically significant, and that they correspond to small geographic areas. The mid-tropospheric warming does not appear sufficient to impact local cloudiness in our model: there are not statistically

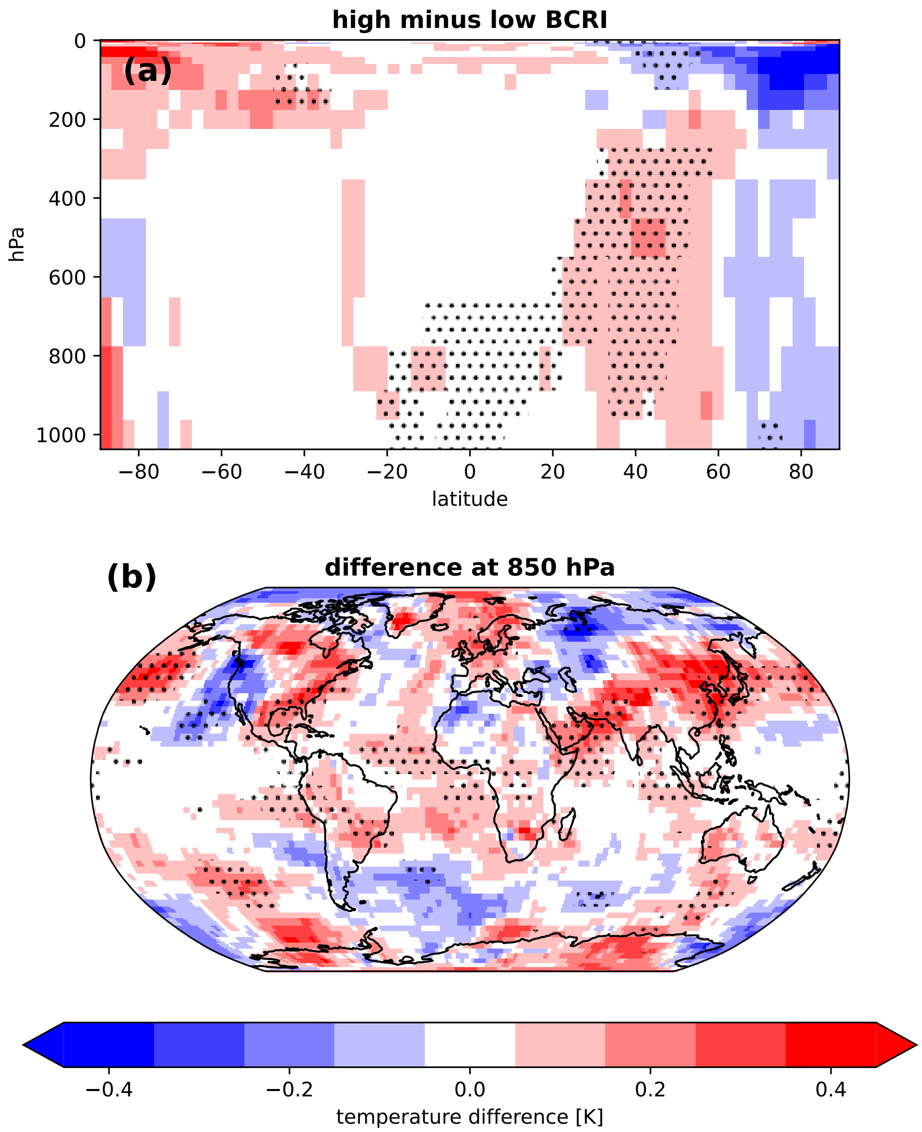


Figure 4.4.3: Difference between tropospheric temperatures in the high- and low-absorption ensembles. **(a)** Vertical profile of zonal-mean temperature differences. **(b)**: spatial distribution of temperature differences at 850 hPa. Stippling indicates statistically significant temperature anomalies.

significant differences between the low- and high-absorption cloud fractions at these levels.

To estimate the potential impact of BCRI on precipitation, we draw on the results of Samset (2022) who derived an expression for global-mean precipitation suppression as a function of changes in AAOD:

$$\Delta P = \frac{dP}{dAbs} \times \frac{dAbs}{dAAOD}\, \Delta AAOD = -4646 \pm 1600\,\mathrm{mm\,y}^{-1}(\mathrm{unit\,AAOD})^{-1} \quad (4.4.1)$$

where $P$ denotes the precipitation rate in mm/year and $Abs$ denotes atmospheric absorption, defined as the difference between top of atmosphere and surface radiative forcings in units of $\mathrm{Wm}^{-2}$. A numerical estimate of the first term in Equation 4.4.1 was derived from historical simulations in AeroCom Phase II and CMIP6 models, and the second term was drawn from the results of Samset et al. (2016) and Persad et al. (2022). Applying Equation 4.4.1 to the global-mean, ensemble-median increase in AAOD obtained by changing from the low to high BCRI yields an estimated precipitation suppression of 5.9 $\pm$ 2.0 mm/year. It is extremely unlikely that this signal would be detectable in the global mean. It is possible, however, that regional changes could be considerably larger.

## 4.5 Discussion

We have demonstrated that increasing the BCRI across the range of values commonly used in the climate modeling literature can increase global-mean AAOD by 42% and BC ERFari by 47%. The resulting increase in the absorption of solar radiation can increase temperatures in the mid and upper troposphere by as much as 0.4°C over major BC source regions, even without considering the potential impacts of BC on sea surface temperatures and sea ice which we have not addressed. For these key BC-relevant fields, therefore, the choice of BCRI is an important and perhaps underappreciated one.

In order to motivate their review on constraining global and regional aerosol absorption, Samset et al. (2018a) briefly explored the effects of modifying the optical properties of BC in CESM1.2. They modified the BCRI by an amount sufficient to increase the resulting AAOD by approximately one standard deviation of the reported AAOD range from AeroCom Phase II (Myhre et al., 2009a). Although they do not report the change in BCRI that was necessary to obtain this increase, the result was an increase in AAOD from $3.0 \times 10^{-3}$ to $4.3 \times 10^{-3}$ ($+1.3 \times 10^{-3}$ or 43%), almost identical to the difference between our low- and high-BCRI ensembles. This increase in absorption led to a global-mean instantaneous ERF of 0.2 W/m$^2$ relative to the control configuration. In our analysis the median increase in total BC ERF was 0.1 W/m$^2$, but was not statistically different from zero.

Diversity in simulated aerosol absorption in AeroCom Phase III models was investigated by Sand et al. (2021). As described in Section 4.4.1, AeroCom Phase III models exhibited a wide range of absorption, with global-mean AAOD attributable to BC ranging from $0.7 \times 10^{-3}$ to $7.7 \times 10^{-3}$. However, they did not display a clear relationship between BCRI and overall absorption. Aerosol absorption is not purely a function of BCRI but rather the result of many competing and uncertain processes (Glià et al., 2021; Koch et al., 2009; Myhre et al., 2009a; Sand et al., 2021). Sand et al. (2021) attribute the AeroCom Phase III spread to three main factors: diversity in the simulated mass load, which ranged from 0.13 to 0.51 mg/m$^2$, driven by differences in deposition processes and thus in aerosol lifetime; diversity in the prescribed density of black carbon, which ranged from 1.0 to 2.3 g/cm$^3$; and diversity in the BCRI, which ranged from 1.75-0.44i to 1.95-0.79i. These three factors contributed similarly to the overall model spread. There was also substantial diversity in the treatment of mixing state, both in terms of the mixing itself and in the calculation of resultant effective optical properties of the mixture, between the participating models. Between the diversity in effective refractive index due to differences in absorption enhancement from mixing, and the diversity of assumed BC density, the correlation between BCRI and mass absorption cross section was found to be low (0.2). Thus while BCRI is an influential parameter choice when all else is held equal, its impact is modulated by the competing effects of other parameterizations.

Although our analysis encompasses the range of BCRI typically used in the climate modelling community, more extreme values may be possible. Bescond et al. (2016) report a value of $m_{532nm} = 1.48 - 0.84i$ derived from observations of ethylene flame. With $E(m_{532nm}) = 0.407$, compared to $E(m_{550nm}) = 0.177$ to 0.255 in our core ensembles, this choice of BCRI indicates far stronger absorption than we have considered in our main analysis. It is likely not representative of the BC being simulated by Earth system models, because most atmospheric BC comes from more complex sources such as coal, propane, or biomass burning, and because BC undergoes rapid morphological transitions after its emission (Ramachandran and Reist, 1995) which alter its optical properties. It nevertheless provides a useful upper limit on the range of plausible BCRI impacts. When used in a fourth ensemble of simulations, the resulting global-mean, ensemble-median AAOD is $7.76 \times 10^{-3}$, an increase of $1.77 \times 10^{-3}$ or 59% over the low-absorption ensemble. BC ERFari increases by 0.19 W/m$^2$ or 100%. Although these increases are substantial, they do not affect our overall conclusions on the importance of BCRI relative to other sources of uncertainty.

## 4.6 Conclusions

The radiative forcing of black carbon is subject to many complex, interconnected sources of uncertainty. We have isolated one key factor, the refractive index (BCRI), and demonstrated its impact on the simulation of several fields. With all other parameterizations held equal, increasing the BCRI from $m_{550nm} = 1.75 - 0.44i$ to $m_{550nm} = 1.95 - 0.79i$ can increase global-mean AAOD by 42% and BC ERFari by 47%. The impacts on AAOD are comparable to the effects of recent updates to anthropogenic and biomass-burning aerosol emission inventories, and in BC source regions, the difference in AAOD between low- and high-absorption ensembles is a third as large as the difference in AAOD retrieved from MISR and POLDER-GRASP satellites. The increase in BC ERFari is comparable to the uncertainty in recent literature estimates. While we do not attribute the spread in model estimates of AAOD and ERFari to diversity in BCRI – rather, the multimodel spread arises from a combination of BC parameter choices including BCRI and density, the treatment of mixing and ageing, and the parameterization of transport and deposition processes, among other factors – the similar magnitude emphasizes the importance of considering BCRI choices in model development and multimodel comparisons.

## 4.A Appendix to Chapter 4

### 4.A.1 CanAM5.1-PAM

The Canadian Atmospheric Model version 5 (CanAM5; Cole et al. (2023)) is the atmospheric component of the Canadian Earth system model CanESM5 (Swart et al., 2019). Here we use CanAM5.1, which contains a number of technical and scientific updates. Most importantly for aerosol modeling, these updates eliminate the occasional formation of spurious tropospheric dust storms seen in CanESM5 (Sigmond et al., 2023).

CanAM5.1 can be run with either of two aerosol schemes: a bulk scheme, which simulates aerosol mass budgets and is typically used for large ensembles, or the PLA Aerosol Model (PAM). PAM uses the Piecewise Lognormal Approximation (PLA; von Salzen (2006)) method to simulate aerosol size distributions using a series of truncated, non-overlapping lognormal modes. Each truncated mode has a specified width; the magnitudes and mode radii are calculated from the predicted mean masses and number concentrations in each section at each timestep.

PAM accounts for internal and external mixing states (Riemer et al., 2019). Black carbon and organic carbon are emitted as externally mixed, hydrophobic aerosol, represented by one mode each. Upon ageing ($\tau$=1h/24h during the day/night) these tracers are merged with pre-existing internally mixed aerosol, which is represented by 3 modes. Dust and sea salt are externally mixed and are represented by two modes each. Sulfate aerosol can form from ternary homogeneous nucleation of water vapour, gaseous sulfuric acid ($H_2SO_4$), and ammonia, after which point it grows by coagulation, or by condensation of water vapour, $H_2SO_4$, and secondary organic aerosol precursor gases (Dunne et al., 2016). All sulfate aerosol is contained within the 3 internally mixed modes and assumed to be fully neutralized by ammonium.

Aerosol sinks in PAM include dry deposition, which depends on ground-surface properties and the near-surface aerosol concentration (Zhang et al., 2001); wet deposition by below-cloud scavenging (Croft et al., 2005); and in-cloud scavenging in convective and layer clouds (Croft et al., 2005; von Salzen et al., 2013). Both below-cloud and in-cloud wet deposition rates are proportional to the precipitation formation rate.

Aerosol activation and cloud droplet growth are determined using pre-calculated solutions to the cloud droplet growth equation for an adiabatically rising air parcel

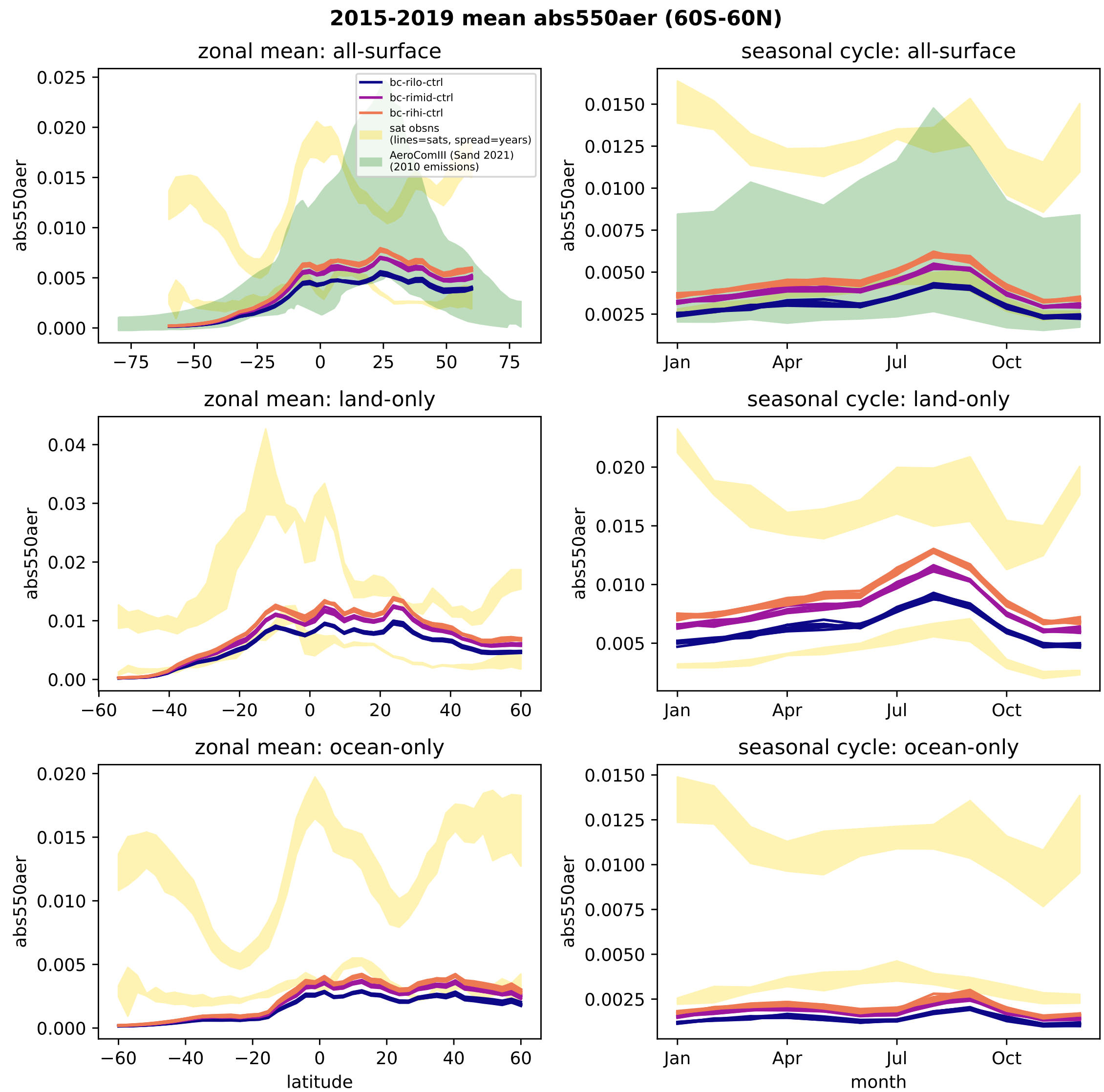


Figure 4.A.1: 2015-2019 zonal mean (left column) and seasonal cycle (right column) of AAOD in PAM ensembles (coloured lines), satellite retrievals (yellow envelopes), and AerCom Phase III models as reported in Figure 2 of Sand et al. (2021) (pink envelope). For PAM models, individual lines denote individual realizations, averaged over 2015-2019. For satellites, the width of the envelope shows the min-max range over the 5 years in question (2015-2019 for MISR, the lower envelope, and 2006-2010 for POLDER-GRASP, the higher envelope). The AeroComII envelope indicates the full min-max range across models, for simulations forced with 2010 emissions. PAM is generally in closer agreement with MISR than POLDER-GRASP, and within the range of both zonal means and seasonal cycles simulated by AeroCom Phase III models.

near the cloud base (Wang et al., 2022). These solutions are stored in lookup tables and referenced using a numerically efficient iterative approach. The simulated cloud droplet number concentration is used to compute the effective radius of the cloud droplets (Peng and Lohmann, 2003) according to the first indirect effect (Lohmann and Feichter, 2005). In the model configuration used here, the second indirect effect is included via autoconversion of cloud to rain droplets (Cole et al., 2023).

Aerosol optical properties in PAM are determined from pre-computed lookup tables, allowing us to generate separate lookup tables for each choice of BCRI. These tables contain optical properties as a function of relative humidity, wavelength, and particle size, calculated using Mie theory. For internally mixed aerosol an effective refractive index is simulated using the Maxwell-Garnett approximation (Wu et al., 2018).

CanAM5.1-PAM's simulated AAOD is in good agreement with other Earth system models and, to the extent that this can be determined given the associated uncertainties, with observations (Figure 4.A.1). The AMAP (2021) report found that CanAM5-PAM was the only model among those assessed that was able to reproduce the observed vertical profile of BC in both the Arctic and northern midlatitudes, although it overestimated BC concentrations near the surface for latitudes north of 60°N.

In this work we only vary the refractive index of atmospheric BC. PAM also includes representations of the albedo effects on BC deposited on snow and ice (Namazi et al., 2015) and absorption of solar radiation by BC-containing cloud droplets (Li et al., 2013), but the optical properties of BC in these settings are not modified in this work.

In the simulations conducted for this analysis, transient historical sea surface temperatures and sea ice concentrations were specified using the PCMDI observational dataset (Taylor et al., 2000) and historical sea ice thickness for the Northern and Southern Hemispheres were taken from PIOMAS (Zhang and Rothrock, 2003) and ORAP5 (Zuo et al., 2017) reanalyses respectively.

### 4.A.2 Region Definitions

The regions used in Figures 4.4.1 and 4.A.3 are defined in Table 4.A.1. Figure 4.A.2 shows these region boundaries overlaid on a map of black carbon burden from the low-BCRI ensemble.

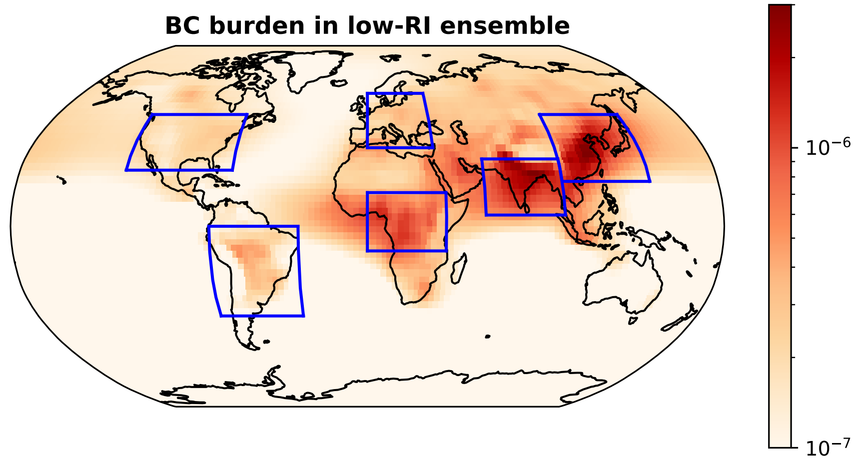


Figure 4.A.2: Black carbon burden (2015-2019 mean, ensemble median) in the low-BCRI ensemble, with analysis regions indicated in blue. Not shown are the near-global (60°S-60°N) and northern hemisphere (0°N-60°N) domains. Region definitions are listed in Table 4.A.1.

| Region | longitude range [°E] | latitude range [°N] |
|---|---|---|
| Near-Global | 0, 360 | -60, 60 |
| Northern Hemisphere | 0, 360 | 0, 60 |
| East Asia | 100, 145 | 20, 50 |
| South Asia | 60, 100 | 5, 30 |
| Europe | 0, 35 | 35, 60 |
| USA | 235, 290 | 25, 50 |
| C. Africa | 0, 40 | -11, 15 |
| S. America | 280, 325 | -40, 0 |

Table 4.A.1: Definitions of the regions used in Figures 4.4.1 and 4.A.3 and shown in Figure 4.A.2. The East Asia and South Asia definitions are taken from the SREX regions used in IPCC AR5, and the C. Africa region combines the SREX regions EAF and WAF (excluding the portion of WAF west of the prime meridian).

## 4.A.3 Total-AOD Results

Figure 4.A.3 reproduces Figure 4.4.1 but for total AOD.

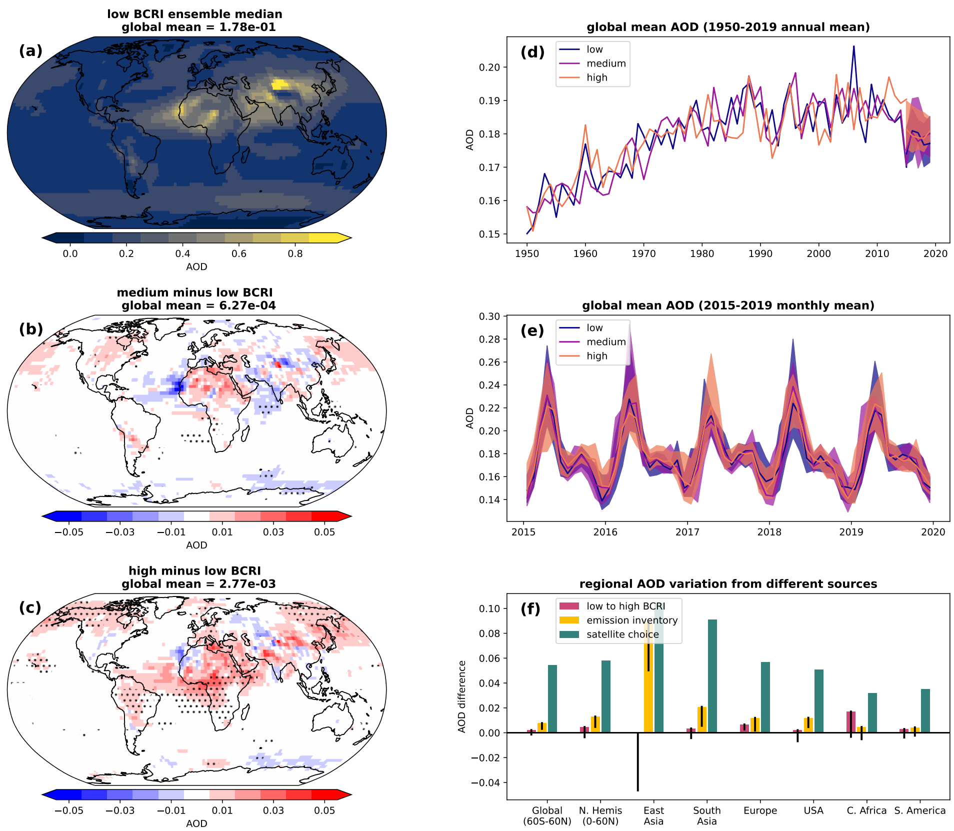


Figure 4.A.3: As Figures 4.4.1 and 4.4.2 but for total aerosol optical depth. BC RI has regionally significant impacts on AOD but the global mean does not differ significantly between low- and high-absorption ensembles. In panel (f), AOD retrievals are taken from MISR, the Moderate Resolution Imaging Spectroradiometer (MODIS; Platnick et al. (2017); King et al. (2013), comparing Aqua and Terra results separately), and the Cloud-Aerosol Lidar with Orthogonal Polarization (CALIOP, Winker et al. (2009)). The AOD range is calculated as the difference between the highest and lowest region-mean values, which in all regions considered turns out to be the difference between MODIS Terra and MISR respectively.

# Chapter 5

# Conclusions

The three projects described in this thesis are united by a common underlying question: how well can we predict the impacts of future emission reductions? But the specific topics which this question were explored are a product of the context in which this thesis was written.

Living in Canada, the first tangible expression of the emerging COVID-19 pandemic was the curtailing of international travel. In March and April of 2020, as I prepared to start my PhD, international borders were closing and domestic travel was being discouraged. As a result, global aviation levels were plummeting at an astonishing rate. As well as being one of the first indications that the international COVID-19 response might have detectable climate impacts, this aviation reduction was one of the first readily available dataset on the topic, with near-real-time updates available through FlightRadar24 (2020a). The climate impacts of aviation, and the changes thereof during COVID-19, were thus a natural place to begin my PhD research. That first project culminated in the publication which now makes up Chapter 2 of this thesis.

In that project, I used the COVID-19 flight reductions to study aviation-induced cirrus (AIC). Despite a sustained global reduction in air traffic, with April 2020 flight numbers less than 40% of their 2019 levels (FlightRadar24, 2020c), aviation-weighted cirrus coverage was not significantly reduced in Spring 2020. A regression model based on the contrail cirrus simulations of Bock and Burkhardt (2016a) did not exhibit a statistically significant dependence of cirrus anomalies on aviation intensity, and suggested that current models may overestimate the impacts of aviation on cirrus. There was also no significant change in diurnal temperature range (DTR) during this period, indicating that apparent DTR changes identified after previous much shorter and more geographically limited flight disruptions (Hong et al., 2008; Sandhu and Baldini, 2018; Travis et al., 2002) were unlikely to have been caused by changes in aviation. Based on these results, I provide the first observationally-constrained estimate of the effective radiative forcing (ERF) from AIC: $8\,(-3,\,22)\,\mathrm{mWm^{-2}}$ for 2018. This estimate relies on many simplifying assumptions, most notably assuming that ERF scales linearly with cirrus coverage. In reality ERF depends on optical thickness, which is a function of ice crystal properties (shape, size, and number) and of ambient conditions (e.g. temperature, humidity, wind shear) Kärcher et al. (2009); Yang et al. (2010); Bock and Burkhardt (2016a); Kärcher et al. (2021), and on what surface the cirrus overlays Yang et al. (2010). These assumptions may explain why my observationally-constrained estimate is so much lower than the Lee et al. (2021) multimodel estimate of $57\,(17,\,98)\,\mathrm{mWm^{-2}}$. Alternatively, if ERF does to first order scale with cirrus coverage, the discrepancy has two plausible interpretations. First, aircraft could produce less AIC than previously thought, such that removing this source of cirrus had little impact on total cirrus coverage. Second, the competition between natural and aviation-induced cirrus could be stronger than predicted by current models, such that more natural cirrus formed to take the place of AIC when the latter was reduced. These two scenarios cannot not be disentangled in the analysis presented here. Future studies could break this degeneracy by looking at changes in the optical properties of cirrus during future flight groundings, for example using observations from the upcoming High-altitude Aerosols, Water, and Clouds (HAWC) mission (Canadian Space Agency, 2023).

As I studied aviation and its impacts on cirrus cloud, the climate modeling community was rapidly cataloguing the broader climate impacts of the COVID-19 lockdowns. Le Quéré et al. (2020) and Forster et al. (2020) used mobility data to estimate the reduction in greenhouse gas and aerosol emissions through the first 6 months of 2020, and from these estimates emerged the COVID-19 Model Intercomparison Project (CovidMIP; Jones et al., 2021). By the time I was completing my first project, CovidMIP had been used to assess the large-scale climate responses to both the COVID-19 lockdowns and a variety of potential recovery scenarios. However, no detailed analysis of the aerosol response had yet been conducted. There was a rapidly expanding literature on the air quality impacts of the COVID-19 emission reductions (Gkatzelis et al., 2021), and a handful of studies estimating simulated aerosol forcings (Fasullo et al., 2021; Fiedler et al., 2021; Forster et al., 2020; Fyfe et al., 2021; Gettelman et al., 2021; Jones et al., 2021; Weber et al., 2020), but no studies had used the observed aerosol responses to COVID-19 to evaluate model simulations. My second project, described in Chapter 3, aimed to fill this gap.

In this project I investigated changes in total and dust-subtracted aerosol optical depth (AOD) in major aerosol source regions. Despite dramatic emission reductions in all of the regions considered, only India experienced a statistically significant reduction in total or dust-subtracted AOD. The signals of more systematic emissions policies, such as clean air legislation in China (Wang et al., 2021; Zheng and Unger, 2021; Paulot et al., 2018), are however visible in the AOD record, suggesting that deliberate air quality policies are more effective at driving large-scale AOD reductions. Earth system models from the CovidMIP project initially appeared to overestimate the dust-subtracted AOD response to COVID-19, but sensitivity tests revealed that a substantial portion of the discrepancy was related to biases in the emission inventory used to construct the COVID-19 scenario (Wang et al., 2021). The CovidMIP experiment was originally developed in terms of fractional emission reductions, and applying these same fractional reductions to a corrected baseline resulted in a smaller perturbation in better agreement with the observations. The impacts of perturbation size and meteorological variability on model evaluation were also investigated, but further assessment of the simulated total and dust-subtracted AOD anomalies were limited by observational uncertainty. The results of this study provide evidence that, given accurate model inputs, current Earth system models can predict the AOD response to other emission reduction scenarios to within observational uncertainty.

Having demonstrated that Earth system models can robustly predict the response of aerosol optical depth to emission reductions, an obvious follow-up question was how well they could predict the resulting climate impact. While finishing the analysis that now comprises Chapter 3, I began contributing to aerosol model development and evaluation with the Canadian Centre for Climate Modeling and Analysis. In the course of this work we had noted that varying the refractive index of black carbon had striking impacts on simulated absorbing aerosol optical depth (AAOD). Given the uncertainty in, and policy relevance of, the climate impacts of black carbon, the sensitivity of these quantities to uncertainty in the refractive index seemed a natural final project. Thus Chapter 4 took shape.

Chapter 4 investigated the sensitivities of AAOD and the effective radiative forcing from black carbon - radiation interactions (BC ERFari) to uncertainty in the refractive index of black carbon (BCRI). This was the first study to isolate the impacts of BCRI in a single atmospheric model, independent of differences in other parameterizations.

I demonstrate that varying the BCRI across values commonly used in the climate modeling community can increase AAOD by 42% and BC ERFari by 47%. Since AAOD is commonly used in observational evaluation of simulated black carbon (e.g. Sand et al., 2021; Gliß et al., 2021), and BC ERFari is key to understanding BC's climate impact (Thornhill et al., 2021; Szopa et al., 2021), these differences have important ramifications for model development and evaluation. Although simulated aerosol absorption is a product of many different interacting parameterizations, the results presented in this chapter clearly demonstrate the importance of considering the BCRI in future model intercomparison projects.

Taken together, these three chapters demonstrate the power of combining observations, multimodel comparison projects, and targeted model sensitivity tests to reduce uncertainty in the impacts of human-climate interactions. COVID-19 in particular provides a unique opportunity to test both our understanding of current anthropogenic impacts on the climate (e.g. via the first observational constraint on the radiative forcing of aviation-induced cirrus) and our ability to predict the impacts of hypothetical future changes (e.g. via observational evaluation of Earth system model simulations of rapid emission reductions). Although the emission reductions associated with the COVID-19 pandemic have proven too short to produce lasting impacts on the climate, it is my sincere hope that the scientific insight gained by studying this period of upheaval will aid in the creation of more lasting change.

# Bibliography

IMO 2020 – cutting sulphur oxide emissions, URL https://www.imo.org/en/MediaCentre/HotTopics/Pages/Sulphur-2020.aspx.

Acharya, P., Barik, G., Gayen, B. K., Bar, S., Maiti, A., Sarkar, A., Ghosh, S., De, S. K., and Sreekesh, S.: Revisiting the Levels of Aerosol Optical Depth in South-Southeast Asia, Europe and USA amid the COVID-19 Pandemic Using Satellite Observations, Environmental Research, 193, https://doi.org/10.1016/j.envres.2020.110514, 2021.

Acosta Navarro, J. C., Ekman, A. M. L., Pausata, F. S. R., Lewinschal, A., Varma, V., Seland, Ø., Gauss, M., Iversen, T., Kirkevåg, A., Riipinen, I., and Hansson, H. C.: Future Response of Temperature and Precipitation to Reduced Aerosol Emissions as Compared with Increased Greenhouse Gas Concentrations, Journal of Climate, 30, https://doi.org/10.1175/JCLI-D-16-0466.1, 2017.

Airlines for America: Airlines for America Data and Statistics: World Airlines Traffic and Capacity, URL https://www.airlines.org/dataset/world-airlines-traffic-and-capacity/, 2021.

Al-Abadleh, H. A., Lysy, M., Neil, L., Patel, P., Mohammed, W., and Khalaf, Y.: Rigorous Quantification of Statistical Significance of the COVID-19 Lockdown Effect on Air Quality: The Case from Ground-Based Measurements in Ontario, Canada, Journal of Hazardous Materials, 413, https://doi.org/10.1016/j.jhazmat.2021.125445, 2021.

AMAP: AMAP Assessment 2021: Impacts of Short-lived Climate Forcers on Arctic Climate, Air Quality, and Human Health, Tech. rep., Arctic Monitoring and Assessment Programme (AMAP), Tromsø, Norway, 2021.

Andrews, E., Ogren, J. A., Kinne, S., and Samset, B.: Comparison of AOD, AAOD and column single scattering albedo from AERONET retrievals and in situ profiling measurements, Atmospheric Chemistry and Physics, 17, 6041–6072, https://doi.org/10.5194/acp-17-6041-2017, 2017.

ASDC, E.: CALIPSO Orbit Change, https://asdc.larc.nasa.gov/news/calipso-orbit-change, last accessed 2023-03-06, 2018.

Balamurugan, V., , Chen, J., Qu, Z., Bi, X., Gensheimer, J., Shekhar, A., Bhattacharjee, S., and Keutsch, F. N.: Tropospheric NO2 and O3 Response to COVID-19 Lockdown Restrictions at the National and Urban Scales in Germany, Journal of Geophysical Research: Atmospheres, 126, https://doi.org/10.1029/2021JD035440, 2021.

Bellouin, N., Rae, J., Jones, A., Johnson, C., Haywood, J., and Boucher, O.: Aerosol Forcing in the Climate Model Intercomparison Project (CMIP5) Simulations by HadGEM2-ES and the Role of Ammonium Nitrate, Journal of Geophysical Research: Atmospheres, 116, https://doi.org/10.1029/2011JD016074, 2011.

Bergman, T., Kerminen, V.-M., Korhonen, H., Lehtinen, K. J., Makkonen, R., Arola, A., Mielonen, T., Romakkaniemi, S., Kulmala, M., and Kokkola, H.: Evaluation of the sectional aerosol microphysics module SALSA implementation in ECHAM5-HAM aerosol-climate model, Geoscientific Model Development, 5, 845–868, https://doi.org/10.5194/gmd-5-845-2012, 2012.

Bickel, M., Ponater, M., Bock, L., Burkhardt, U., and Reineke, S.: Estimating the Effective Radiative Forcing of Contrail Cirrus, Journal of Climate, 33, https://doi.org/10.1175/JCLI-D-19-0467.1, 2020.

Birkmann, J., Liwenga, E., Pandey, R., Boyd, E., Djalante, R., Gemenne, F., Leal Filho, W., Pinho, P., Stringer, L., and Wrathall, D.: Health, Wellbeing, and the Changing Structure of Communities, chapter 8, Cambridge University Press, Cambridge, United Kingdom and New York, NY, USA, https://doi.org/10.1017/9781009325844.010, 2022.

Bock, L. and Burkhardt, U.: Reassessing Properties and Radiative Forcing of Contrail Cirrus Using a Climate Model, Journal of Geophysical Research: Atmospheres, 121, https://doi.org/10.1002/2016JD025112, 2016a.

Bock, L. and Burkhardt, U.: The Temporal Evolution of a Long-Lived Contrail Cirrus Cluster: Simulations with a Global Climate Model, Journal of Geophysical Research: Atmospheres, 121, https://doi.org/10.1002/2015JD024475, 2016b.

Bohren, C. F. and Huffman, D. R.: Absorption and scattering of light by small particles, Wiley, New York, 1983.

Bond, T. C. and Bergstrom, R. W.: Light Absorption by Carbonaceous Particles: An Investigative Review, Aerosol Science and Technology, 40, https://doi.org/10.1080/02786820500421521, 2006.

Bond, T. C., Doherty, S. J., Fahey, D. W., Forster, P. M., Berntsen, T., DeAngelo, B. J., Flanner, M. G., Ghan, S., Kärcher, B., Koch, D., Kinne, S., Kondo, Y., Quinn, P. K., Sarofim, M. C., Schultz, M. G., Schulz, M., Venkataraman, C., Zhang, H., Zhang, S., Bellouin, N., Guttikunda, S. K., Hopke, P. K., Jacobson,

M. Z., Kaiser, J. W., Klimont, Z., Lohmann, U., Schwarz, J. P., Shindell, D., Storelvmo, T., Warren, S. G., and Zender, C. S.: Bounding the Role of Black Carbon in the Climate System: A Scientific Assessment, Journal of Geophysical Research: Atmospheres, 118, https://doi.org/10.1002/jgrd.50171, 2013.

Boucher, O., Randall, D., Artaxo, P., Bretherton, C., Feingold, G., Forster, P., Kerminen, V.-M., Kondo, Y., Liao, H., Lohmann, U., Rasch, P. and. Satheesh, S., Sherwood, S., Stevens, B., and Zhang, X.: Clouds and Aerosols, chapter 7, Cambridge University Press, Cambridge, United Kingdom and New York, NY, USA, 2013.

Brulle, R. and Pellow, D.: nvironmental justice: human health and environmental inequalities, Annual Review of Public Health, 27, 103–124, https://doi.org/10.1146/annurev.publhealth.27.021405.102124, 2006.

Burkhardt, U. and Kärcher, B.: Global Radiative Forcing from Contrail Cirrus, Nature Climate Change, 1, https://doi.org/10.1038/nclimate1068, 2011.

Burkhardt, U., Kärcher, B., and Schumann, U.: Global Modeling of the Contrail and Contrail Cirrus Climate Impact, Bulletin of the American Meteorological Society, 91, https://doi.org/10.1175/2009BAMS2656.1, 2010.

Canadian Space Agency: HAWC mission: Clouds and aerosols to help predict climate change, URL `https://www.asc-csa.gc.ca/eng/satellites/hawc/`, 2023.

Caretta, M., Mukherji, A., Arfanuzzaman, M., Betts, R., Gelfan, A., Hirabayashi, Y., Lissner, T., Liu, J., Lopez Gunn, E., Morgan, R., Mwanga, S., and Supratid, S.: Water, chapter 4, Cambridge University Press, Cambridge, United Kingdom and New York, NY, USA, https://doi.org/10.1017/9781009325844.006, 2022.

Chang, H.-c. and Charalampopoulos, T. T.: Determination of the wavelength dependence of refractive indices of flame soot, Proceedings of the Royal Society of London. Series A: Mathematical and Physical Sciences, 430, 577–591, https://doi.org/10.1098/rspa.1990.0107, 1990.

Chang, Y., Huang, R.-J., Ge, X., Huang, X., Hu, J., Duan, Y., Zou, Z., Liu, X., and Lehmann, M. F.: Puzzling Haze Events in China During the Coronavirus (COVID-19) Shutdown, Geophysical Research Letters, 47, https://doi.org/10.1029/2020GL088533, 2020.

Chin, M., Ginoux, P., Kinne, S., Torres, O., Holben, B., Duncan, B., Martin, R., Logan, J., Higurashi, A., and Nakajima, T.: Tropospheric Aerosol Optical Thickness from the GOCART Model and Comparisons with Satellite and Sun Photometer Measurements, Journal of the Atmospheric Sciences, 59, 461–483, https://doi.org/10.1175/1520-0469(2002)059<0461:TAOTFT>2.0.CO;2, 2002.

Cissé, G., McLeman, R., Adams, H., Aldunce, P., Bowen, K., Campbell-Lendrum, D., Clayton, S., Ebi, K., Hess, J., Huang, C., Liu, Q., McGregor, G., Semenza, J., and Tirado, M.: Health, Wellbeing, and the Changing Structure of Communities, chapter 7, Cambridge University Press, Cambridge, United Kingdom and New York, NY, USA, https://doi.org/10.1017/9781009325844.009, 2022.

Colarco, P., da Silva, A., Chin, M., and Diehl, T.: Online simulations of global aerosol distributions in the NASA GEOS-4 model and comparisons to satellite and ground-based aerosol optical depth, Journal of Geophysical Research: Atmospheres, 115, https://doi.org/10.1029/2009JD012820, 2010.

Cole, J. N. S., von Salzen, K., Li, J., Scinocca, J., Plummer, D., Arora, V., McFarlane, N., Lazare, M., MacKay, M., and Verseghy, D.: The Canadian Atmospheric Model Version 5 (CanAM5.0.3), Geoscientific Model Development, 16, https://doi.org/10.5194/gmd-16-5427-2023, 2023.

Collins, W., Lamarque, J.-F., Schulz, M., Boucher, O., Eyring, V., Hegglin, M., Maycock, A., Myhre, G., Prather, M., Shindell, D., and Smith, S. J.: AerChemMIP: quantifying the effects of chemistry and aerosols in CMIP6, Geosci. Model Dev., 10, 585–607, https://doi.org/10.5194/gmd-10-585-2017, 2017.

Cooley, S., Schoeman, D., Bopp, L., Boyd, P., Donner, S., Ghebrehiwet, D., Ito, S.-I., Kiessling, W., Martinetto, P., Ojea, E., Racault, M.-F., Rost, B., and Skern-Mauritzen, M.: Ocean and Coastal Ecosystems and Their Services, chapter 3, Cambridge University Press, Cambridge, United Kingdom and New York, NY, USA, https://doi.org/10.1017/9781009325844.005, 2022.

Croft, B., Lohmann, U., and von Salzen, K.: Black carbon ageing in the Canadian Centre for Climate modelling and analysis atmospheric general circulation model, Atmospheric Chemistry and Physics, 5, 1931–1949, https://doi.org/10.5194/acp-5-1931-2005, 2005.

d'Almeida, G., Koepke, P., and Shettle, E.: Atmospheric Aerosols: Global Climatology and Radiative Characteristics, A. Deepak Publishing, Hampton, VA, 1991.

Deivanayagam, T., English, S., Hickel, J., Bonifacio, J., Guinto, R., Hill, K., Huq, M., Issa, R., Mulindwa, H., Nagginda, H., de Morais Sato, R., Selvarajah, S., Sharma, C., and Devakumar, D.: Envisioning environmental equity: climate change, health, and racial justice, The Lancet, 402, 64–78, https://doi.org/https://doi.org/10.1016/S0140-6736(23)00919-4, 2023.

Deroubaix, A., Brasseur, G., Gaubert, B., Labuhn, I., Menut, L., Siour, G., and Tuccella, P.: Response of surface ozone concentration to emission reduction and meteorology during the COVID-19 lockdown in Europe, Meteorological Applications, 28, e1990, https://doi.org/10.1002/met.1990, 2021.

Diamond, M. S. and Wood, R.: Limited Regional Aerosol and Cloud Microphysical Changes Despite Unprecedented Decline in Nitrogen Oxide Pollution During the February 2020 COVID-19 Shutdown in China, Geophysical Research Letters, 47, https://doi.org/10.1029/2020GL088913, 2020.

Digby, R. A. R., Gillett, N. P., Monahan, A. H., and Cole, J. N. S.: An Observational Constraint on Aviation-Induced Cirrus From the COVID-19-Induced Flight Disruption, Geophysical Research Letters, 48, https://doi.org/10.1029/2021GL095882, 2021.

Digby, R. A. R., Gillett, N. P., Monahan, A. H., von Salzen, K., Gkikas, A., Song, Q., and Zhang, Z.: How Well Do Earth System Models Reproduce the Observed Aerosol Response to Rapid Emission Reductions? A COVID-19 Case Study, Atmospheric Chemistry and Physics, 24, https://doi.org/10.5194/acp-24-2077-2024, 2024.

Diner, D., Beckert, J., Reilly, T., Bruegge, C., Conel, J., Kahn, R., Martonchik, J., Ackerman, T., Davies, R., Gerstl, S., Gordon, H., Muller, J.-P., Myneni, R., Sellers, P., Pinty, B., and Verstraete, M.: Multi-Angle Imaging SpectroRadiometer (MISR) Instrument Description and Experiment Overview, IEEE Transactions on Geoscience and Remote Sensing, 36, https://doi.org/10.1109/36.700992, 1998.

Dubovik, O., Herman, M., Holdak, A., Lapyonok, T., Tanré, D., Deuzé, J. L., Ducos, F., Sinyuk, A., and Lopatin, A.: Statistically optimized inversion algorithm for enhanced retrieval of aerosol properties from spectral multi-angle polarimetric satellite observations, Atmos. Meas. Tech., 4, 975–1018, 2011.

Dunne, E. M., Gordon, H., Kürten, A., Almeida, J., Duplissy, J., Williamson, C., Ortega, I. K., Pringle, K. J., Adamov, A., Baltensperger, U., Barmet, P., Benduhn, F., Bianchi, F., Breitenlechner, M., Clarke, A., Curtius, J., Dommen, J., Donahue, N. M., Ehrhart, S., Flagan, R. C., Franchin, A., Guida, R., Hakala, J., Hansel, A., Heinritzi, M., Jokinen, T., Kangasluoma, J., Kirkby, J., Kulmala, M., Kupc, A., Lawler, M. J., Lehtipalo, K., Makhmutov, V., Mann, G., Mathot, S., Merikanto, J., Miettinen, P., Nenes, A., Onnela, A., Rap, A., Reddington, C. L. S., Riccobono, F., Richards, N. A. D., Rissanen, M. P., Rondo, L., Sarnela, N., Schobesberger, S., Sengupta, K., Simon, M., Sipilä, M., Smith, J. N., Stozkhov, Y., Tomé, A., Tröstl, J., Wagner, P. E., Wimmer, D., Winkler, P. M., Worsnop, D. R., and Carslaw, K. S.: Global atmospheric particle formation from CERN CLOUD measurements, Science, 354, 1119–1124, https://doi.org/10.1126/science.aaf2649, 2016.

Eyring, V., Bony, S., Meehl, G. A., Senior, C. A., Stevens, B., Stouffer, R. J., and Taylor, K. E.: Overview of the Coupled Model Intercomparison Project Phase 6 (CMIP6) Experimental Design and Organization, Geoscientific Model Development, 9, https://doi.org/10.5194/gmd-9-1937-2016, 2016.

Eyring, V., Gillett, N., Achuta Rao, K., Barimalala, R., Barreiro Parrillo, M., Bellouin, N., Cassou, C., Durack, P., Kosaka, Y., McGregor, S., Min, S., Morgenstern, O., and Sun, Y.: Human Influences on the Climate System, chapter 3, pp. 287–422, Cambridge University Press, Cambridge, United Kingdom and New York, NY, USA, https://doi.org/10.1017/9781009157896.005, 2021.

Fasullo, J. T., Rosenbloom, N., Buchholz, R. R., Danabasoglu, G., Lawrence, D. M., and Lamarque, J.-F.: Coupled Climate Responses to Recent Australian Wildfire and COVID-19 Emissions Anomalies Estimated in CESM2, Geophysical Research Letters, 48, https://doi.org/10.1029/2021GL093841, 2021.

Fiedler, S., Wyser, K., Rogelj, J., and van Noije, T.: Radiative Effects of Reduced Aerosol Emissions during the COVID-19 Pandemic and the Future Recovery, Atmospheric Research, 264, https://doi.org/10.1016/j.atmosres.2021.105866, 2021.

Field, R. D., Hickman, J. E., Geogdzhayev, I. V., Tsigaridis, K., and Bauer, S. E.: Changes in Satellite Retrievals of Atmospheric Composition over Eastern China during the 2020 COVID-19 Lockdowns, Atmospheric Chemistry and Physics, 21, https://doi.org/10.5194/acp-21-18333-2021, 2021.

Flanner, M., Liu, X., Zhou, C., Penner, J., and Jiao, C.: Enhanced solar energy absorption by internally-mixed black carbon in snow grains, Atmospheric Chemistry and Physics, 12, 4699–4721, https://doi.org/10.5194/acp-12-4699-2012, 2012.

FlightRadar24: FlightRadar24 Live Air Traffic, URL `https://www.flightradar24.com`, 2020a.

FlightRadar24: Commercial flights down 42% in 2020, URL `https://www.flightradar24.com/blog/commercial-flights-down-42-in-2020/`, 2020b.

FlightRadar24: Aviation's slow recovery: May air traffic statistics, URL `https://www.flightradar24.com/blog/aviations-slow-recovery-may-air-traffic-statistics/`, 2020c.

FlightRadar24: FlightRadar24: Flight Tracking Statistics, URL `https://www.flightradar24.com/data/statistics`, 2021.

Forster, P. M., Richardson, T., Maycock, A. C., Smith, C. J., Samset, B. H., Myhre, G., Andrews, T., Pincus, R., and Schulz, M.: Recommendations for diagnosing effective radiative forcing from climate models for CMIP6, Journal of Geophysical Research: Atmospheres, 121, 12,460–12,475, https://doi.org/10.1002/2016JD025320, 2016.

Forster, P. M., Forster, H. I., Evans, M. J., Gidden, M. J., Jones, C. D., Keller, C. A., Lamboll, R. D., Quéré, C. L., Rogelj, J., Rosen, D., Schleussner, C.-F., Richardson, T. B., Smith, C. J., and Turnock, S. T.: Current and Future Global Climate

Impacts Resulting from COVID-19, Nature Climate Change, 10, https://doi.org/10.1038/s41558-020-0883-0, 2020.

Fyfe, J. C., Kharin, V. V., Swart, N., Flato, G. M., Sigmond, M., and Gillett, N. P.: Quantifying the Influence of Short-Term Emission Reductions on Climate, Science Advances, 7, https://doi.org/10.1126/sciadv.abf7133, 2021.

Ganguly, D., Rasch, P. J., Wang, H., and Yoon, J.-H.: Climate Response of the South Asian Monsoon System to Anthropogenic Aerosols, Journal of Geophysical Research: Atmospheres, 117, https://doi.org/10.1029/2012JD017508, 2012.

Gao, J., Yang, Y., Wang, H., Wang, P., Li, H., Li, M., Ren, L., Yue, X., and Liao, H.: Fast Climate Responses to Emission Reductions in Aerosol and Ozone Precursors in China during 2013–2017, Atmospheric Chemistry and Physics, 22, https://doi.org/10.5194/acp-22-7131-2022, 2022.

Gaubert, B., Bouarar, I., Doumbia, T., Liu, Y., Stavrakou, T., Deroubaix, A., Darras, S., Elguindi, N., Granier, C., Lacey, F., Müller, J.-F., Shi, X., Tilmes, S., Wang, T., and Brasseur, G. P.: Global Changes in Secondary Atmospheric Pollutants During the 2020 COVID-19 Pandemic, Journal of Geophysical Research: Atmospheres, 126, https://doi.org/10.1029/2020JD034213, 2021.

Gensheimer, J., Chen, J., Turner, A. J., Shekhar, A., Wenzel, A., and Keutsch, F. N.: What Are the Different Measures of Mobility Telling Us About Surface Transportation CO2 Emissions During the COVID-19 Pandemic?, Journal of Geophysical Research: Atmospheres, 126, https://doi.org/10.1029/2021JD034664, 2021.

Gettelman, A., Chen, C.-C., and Bardeen, C. G.: The Climate Impact of COVID-19-induced Contrail Changes, Atmospheric Chemistry and Physics, 21, https://doi.org/10.5194/acp-21-9405-2021, 2021.

Ghan, S.: Technical Note: Estimating Aerosol Effects on Cloud Radiative Forcing, Atmospheric Chemistry and Physics, 13, https://doi.org/10.5194/acp-13-9971-2013, 2013.

Gkatzelis, G. I., Gilman, J. B., Brown, S. S., Eskes, H., Gomes, A. R., Lange, A. C., McDonald, B. C., Peischl, J., Petzold, A., Thompson, C. R., and Kiendler-Scharr, A.: The Global Impacts of COVID-19 Lockdowns on Urban Air Pollution, Elementa: Science of the Anthropocene, 9, https://doi.org/10.1525/elementa.2021.00176, 2021.

Gkikas, A., Proestakis, E., Amiridis, V., Kazadzis, S., Di Tomaso, E., Tsekeri, A., Marinou, E., Hatzianastassiou, N., and Pérez García-Pando, C.: ModIs Dust AeroSol (MIDAS): A Global Fine-Resolution Dust Optical Depth Data Set, Atmospheric Measurement Techniques, 14, https://doi.org/10.5194/amt-14-309-2021, 2021.

Gliß, J., Mortier, A., Schulz, M., Andrews, E., Balkanski, Y., Bauer, S. E., Benedictow, A. M. K., Bian, H., Checa-Garcia, R., Chin, M., Ginoux, P., Griesfeller, J. J., Heckel, A., Kipling, Z., Kirkevåg, A., Kokkola, H., Laj, P., Le Sager, P., Lund, M. T., Lund Myhre, C., Matsui, H., Myhre, G., Neubauer, D., van Noije, T., North, P., Olivié, D. J. L., Rémy, S., Sogacheva, L., Takemura, T., Tsigaridis, K., and Tsyro, S. G.: AeroCom Phase III Multi-Model Evaluation of the Aerosol Life Cycle and Optical Properties Using Ground- and Space-Based Remote Sensing as Well as Surface in Situ Observations, Atmospheric Chemistry and Physics, 21, https://doi.org/10.5194/acp-21-87-2021, 2021.

Goldberg, D. L., Anenberg, S. C., Griffin, D., McLinden, C. A., Lu, Z., and Streets, D. G.: Disentangling the Impact of the COVID-19 Lockdowns on Urban NO2 From Natural Variability, Geophysical Research Letters, 47, https://doi.org/10.1029/2020GL089269, 2020.

Gouda, K., Gogeri, I., and ThippaReddy, A.: Assessment of Aerosol Optical Depth over Indian Subcontinent during COVID-19 lockdown (March–May 2020), Environmental Monitoring and Assessment, 194, 1573–2959, https://doi.org/10.1007/s10661-022-09855-3, 2022.

Grewe, V., Matthes, S., Frömming, C., Brinkop, S., Jöckel1, P., Gierens, K., Champougny, T., Fuglestvedt, J., Haslerud, A., Irvine, E., and Shine, K.: Feasibility of climate-optimized air traffic routing for trans-Atlantic flights, Environmental Research Letters, 12, https://doi.org/10.1088/1748-9326/aa5ba0, 2017.

Griffin, D., McLinden, C. A., Racine, J., Moran, M. D., Fioletov, V., Pavlovic, R., Mashayekhi, R., Zhao, X., and Eskes, H.: Assessing the Impact of Corona-Virus-19 on Nitrogen Dioxide Levels over Southern Ontario, Canada, Remote Sensing, 12, https://doi.org/10.3390/rs12244112, 2020.

Gulev, S., Thorne, P., Ahn, J., Dentener, F., Domingues, C., Gerland, S., Gong, D., Kaufman, D., Nnamchi, H., Quaas, J., Rivera, J., Sathyendranath, S.and Smith, S., Trewin, B., von Schuckmann, K., and Vose, R.: Changing State of the Climate System, chapter 2, pp. 287–422, Cambridge University Press, Cambridge, United Kingdom and New York, NY, USA, https://doi.org/10.1017/9781009157896.004, 2021.

Hajima, T., Watanabe, M., Yamamoto, A., Tatebe, H., Noguchi, M. A., Abe, M., Ohgaito, R., Ito, A., Yamazaki, D., Okajima, H., Ito, A., Takata, K., Ogochi, K., Watanabe, S., and Kawamiya, M.: Development of the MIROC-ES2L Earth system model and the evaluation of biogeochemical processes and feedbacks, Geoscientific Model Development, 13, 2197–2244, https://doi.org/10.5194/gmd-13-2197-2020, 2020.

Hale, T., Angrist, N., Goldszmidt, R., Kria, B., Petherick, A., Phillips, T., Webster, S., Cameron-Blake, E., Hallas, L., Majumdar, S., and Tatlow, H.: A global panel database of pandemic policies (Oxford COVID-19 Government Response Tracker)., Nature Human Behaviour, https://doi.org/10.1038/s41562-021-01079-8, 2021.

Hammer, M. S., van Donkelaar, A., Martin, R. V., McDuffie, E. E., Lyapustin, A., Sayer, A. M., Hsu, N. C., Levy, R. C., Garay, M. J., Kalashnikova, O. V., and Kahn, R. A.: Effects of COVID-19 Lockdowns on Fine Particulate Matter Concentrations, Science Advances, 7, https://doi.org/10.1126/sciadv.abg7670, 2021.

Hersbach, H., Bell, B., Berrisford, P., Biavati, G., Horányi, A., Muñoz Sabater, J., Nicolas, J., Peubey, C., Radu, R., Rozum, I., Schepers, D., Simmons, A., Soci, C., Dee, D., and Thépaut, J.-N.: ERA5 hourly data on single levels from 1979 to present. Copernicus Climate Change Service (C3S) Climate Data Store (CDS)., https://doi.org/10.24381/cds.adbb2d47, 2018.

Hersbach, H., Bell, B., Berrisford, P., Hirahara, S., Horányi, A., Muñoz-Sabater, J., Nicolas, J., Peubey, C., Radu, R., Schepers, D., Simmons, A., Soci, C., Abdalla, S., Abellan, X., Balsamo, G., Bechtold, P., Biavati, G., Bidlot, J., Bonavita, M., De Chiara, G., Dahlgren, P., Dee, D., Diamantakis, M., Dragani, R., Flemming, J., Forbes, R., Fuentes, M., Geer, A., Haimberger, L., Healy, S., Hogan, R. J., Hólm, E., Janisková, M., Keeley, S., Laloyaux, P., Lopez, P., Lupu, C., Radnoti, G., de Rosnay, P., Rozum, I., Vamborg, F., Villaume, S., and Thépaut, J.-N.: The ERA5 Global Reanalysis, Quarterly Journal of the Royal Meteorological Society, 146, https://doi.org/10.1002/qj.3803, 2020.

Heyn, I., Block, K., Mülmenstädt, J., Gryspeerdt, E., Kühne, P., Salzmann, M., and Quaas, J.: Assessment of simulated aerosol effective radiative forcings in the terrestrial spectrum, Geophysical Research Letters, 44, 1001–1007, https://doi.org/10.1002/2016GL071975, 2017.

Hienola, A., Partanen, A.-I., Pietikäinen, J.-P., O'Donnell, D., Korhonen, H., Matthews, H. D., and Laaksonen, A.: The Impact of Aerosol Emissions on the 1.5°C Pathways, Environmental Research Letters, 13, https://doi.org/10.1088/1748-9326/aab1b2, 2018.

Hodnebrog, Ø., Myhre, G., and Samset, B. H.: How Shorter Black Carbon Lifetime Alters Its Climate Effect, Nature Communications, 5, https://doi.org/10.1038/ncomms6065, 2014.

Hoesly, R. M., Smith, S. J., Feng, L., Klimont, Z., Janssens-Maenhout, G., Pitkanen, T., Seibert, J. J., Vu, L., Andres, R. J., Bolt, R. M., Bond, T. C., Dawidowski, L., Kholod, N., Kurokawa, J.-i., Li, M., Liu, L., Lu, Z., Moura, M. C. P., O'Rourke, P. R., and Zhang, Q.: Historical (1750–2014) Anthropogenic Emissions of Reactive Gases and Aerosols from the Community Emissions Data System (CEDS), Geoscientific Model Development, 11, https://doi.org/10.5194/gmd-11-369-2018, 2018.

Hong, G., Yang, P., Minnis, P., Hu, Y. X., and North, G.: Do Contrails Significantly Reduce Daily Temperature Range?, \grl, 35, https://doi.org/10.1029/2008GL036108, 2008.

Hu, D., Alfarra, M. R., Szpek, K., Langridge, J. M., Cotterell, M. I., Flynn, M. J., Shao, Y., Voliotis, A., Du, M., Liu, D., Johnson, B., McFiggans, G., Haywood, J. M., Coe, H., and Allan, J.: Refractive Index of Engine-Emitted Black Carbon and the Influence of Organic Coatings on Optical Properties, Journal of Geophysical Research: Atmospheres, 128, e2023JD039 178, https://doi.org/10.1029/2023JD039178, 2023.

Huang, X., Ding, A., Gao, J., Zheng, B., Zhou, D., Qi, X., Tang, R., Wang, J., Ren, C., Nie, W., Chi, X., Xu, Z., Chen, L., Li, Y., Che, F., Pang, N., Wang, H., Tong, D., Qin, W., Cheng, W., Liu, W., Fu, Q., Liu, B., Chai, F., Davis, S. J., Zhang, Q., and He, K.: Enhanced Secondary Pollution Offset Reduction of Primary Emissions during COVID-19 Lockdown in China, National Science Review, 8, https://doi.org/10.1093/nsr/nwaa137, 2021.

Hubanks, P., Platnick, S., King, M., and Ridgway, B.: MODIS Atmosphere L3 Gridded Product Algorithm Theoretical Basis Document (ATBD) and Users Guide, 2020.

IATA Pressroom: 2020 Worst Year in History for Air Travel Demand, URL `https://www.iata.org/en/pressroom/pr/2021-02-03-02/`, 2021.

Ibrahim, S., Landa, M., Pesek, O., Pavelka, K., and Halounova, L.: Space-Time Machine Learning Models to Analyze COVID-19 Pandemic Lockdown Effects on Aerosol Optical Depth over Europe, Remote Sensing, 13, https://doi.org/10.3390/rs13153027, 2021.

Jia, M., Evangeliou, N., Eckhardt, S., Huang, X., Gao, J., Ding, A., and Stohl, A.: Black Carbon Emission Reduction Due to COVID-19 Lockdown in China, Geophysical Research Letters, 48, https://doi.org/10.1029/2021GL093243, 2021.

Jones, C. D., Hickman, J. E., Rumbold, S. T., Walton, J., Lamboll, R. D., Skeie, R. B., Fiedler, S., Forster, P. M., Rogelj, J., Abe, M., Botzet, M., Calvin, K., Cassou, C., Cole, J. N. S., Davini, P., Deushi, M., Dix, M., Fyfe, J. C., Gillett, N. P., Ilyina, T., Kawamiya, M., Kelley, M., Kharin, S., Koshiro, T., Li, H., Mackallah, C., Müller, W. A., Nabat, P., van Noije, T., Nolan, P., Ohgaito, R., Olivié, D., Oshima, N., Parodi, J., Reerink, T. J., Ren, L., Romanou, A., Séférian, R., Tang, Y., Timmreck, C., Tjiputra, J., Tourigny, E., Tsigaridis, K., Wang, H., Wu, M., Wyser, K., Yang, S., Yang, Y., and Ziehn, T.: The Climate Response to Emissions Reductions Due to COVID-19: Initial Results From CovidMIP, Geophysical Research Letters, 48, https://doi.org/10.1029/2020GL091883, 2021.

Kahn, R. A., Nelson, D. L., Garay, M. J., Levy, R. C., Bull, M. A., Diner, D. J., Martonchik, J. V., Paradise, S. R., Hansen, E. G., and Remer, L. A.: MISR Aerosol Product Attributes and Statistical Comparisons With MODIS, IEEE Transactions on Geoscience and Remote Sensing, 47, https://doi.org/10.1109/TGRS.2009.2023115, 2009.

Kärcher, B.: Cirrus Clouds and Their Response to Anthropogenic Activities, Current Climate Change Reports, 3, https://doi.org/10.1007/s40641-017-0060-3, 2017.

Kärcher, B.: Formation and Radiative Forcing of Contrail Cirrus, Nature Communications, 9, https://doi.org/10.1038/s41467-018-04068-0, 2018.

Karcher, B., Mohler, O., DeMott, P. J., Pechtl, S., and Yu, F.: Insights into the Role of Soot Aerosols in Cirrus Cloud Formation, Atmos. Chem. Phys., 2007.

Kärcher, B., Burkhardt, U., Unterstrasser, S., and Minnis, P.: Factors Controlling Contrail Cirrus Optical Depth, Atmospheric Chemistry and Physics, 9, https://doi.org/10.5194/acp-9-6229-2009, 2009.

Kärcher, B., Mahrt, F., and Marcolli, C.: Process-Oriented Analysis of Aircraft Soot-Cirrus Interactions Constrains the Climate Impact of Aviation, Communications Earth & Environment, 2, https://doi.org/10.1038/s43247-021-00175-x, 2021.

Kim, M.-H., Omar, A. H., Tackett, J. L., Vaughan, M. A., Winker, D. M., Trepte, C. R., Hu, Y., Liu, Z., Poole, L. R., Pitts, M. C., Kar, J., and Magill, B. E.: The CALIPSO version 4 automated aerosol classification and lidar ratio selection algorithm, Atmos. Meas. Tech., 11, 6107–6135, https://doi.org/10.5194/amt-11-6107-2018, 2018.

King, M. D., Platnick, S., Menzel, W. P., Ackerman, S. A., and Hubanks, P. A.: Spatial and temporal distribution of clouds observed by MODIS onboard the Terra and Aqua satellites, IEEE Trans. Geosci. Remote Sens., 51, 3826–3852, https://doi.org/10.1109/TGRS.2012.2227333, 2013.

Koch, D. and Del Genio, A. D.: Black Carbon Semi-Direct Effects on Cloud Cover: Review and Synthesis, Atmospheric Chemistry and Physics, 10, https://doi.org/10.5194/acp-10-7685-2010, 2010.

Koch, D., Schulz, M., Kinne, S., McNaughton, C., Spackman, J. R., Balkanski, Y., Bauer, S., Berntsen, T., Bond, T. C., Boucher, O., Chin, M., Clarke, A., De Luca, N., Dentener, F., Diehl, T., Dubovik, O., Easter, R., Fahey, D. W., Feichter, J., Fillmore, D., Freitag, S., Ghan, S., Ginoux, P., Gong, S., Horowitz, L., Iversen, T., Kirkev&aring, G, A., Klimont, Z., Kondo, Y., Krol, M., Liu, X., Miller, R., Montanaro, V., Moteki, N., Myhre, G., Penner, J. E., Perlwitz, J., Pitari, G., Reddy, S., Sahu, L., Sakamoto, H., Schuster, G., Schwarz, J. P., Seland, Ø., Stier, P., Takegawa, N., Takemura, T., Textor, C., van Aardenne, J. A., and Zhao, Y.:

Evaluation of Black Carbon Estimations in Global Aerosol Models, Atmospheric Chemistry and Physics, 9, https://doi.org/10.5194/acp-9-9001-2009, 2009.

Kong, L., Tang, X., Zhu, J., Wang, Z., Sun, Y., Fu, P., Gao, M., Wu, H., Lu, M., Wu, Q., Huang, S., Sui, W., Li, J., Pan, X., Wu, L., Akimoto, H., and Carmichael, G. R.: Unbalanced Emission Reductions of Different Species and Sectors in China during COVID-19 Lockdown Derived by Multi-Species Surface Observation Assimilation, Atmospheric Chemistry and Physics Discussions, https://doi.org/10.5194/acp-2022-729, 2023.

Krieler, E., O'Neill, B., Hallegatte, S., Kram, T., Lempert, R., Moss, R., and WIlbanks, T.: The need for and use of socio-economic scenarios for climate change analysis: A new approach based on shared socio-economic pathways, Global Environmental Change, 22, 807–822, https://doi.org/10.1016/j.gloenvcha.2012.05.005, 2012.

Kroll, J. H., Heald, C. L., Cappa, C. D., Farmer, D. K., Fry, J. L., Murphy, J. G., and Steiner, A. L.: The Complex Chemical Effects of COVID-19 Shutdowns on Air Quality, Nature Chemistry, 12, https://doi.org/10.1038/s41557-020-0535-z, 2020.

Lamarque, J.-F., Kyle, G. P., Meinshausen, M., Riahi, K., Smith, S. J., van Vuuren, D. P., Conley, A. J., and Vitt, F.: Global and regional evolution of short-lived radiatively-active gases and aerosols in the Representative Concentration Pathways, Climatic Change, 109, https://doi.org/10.1007/s10584-011-0155-0, 2011.

Lamboll, R. D., Jones, C. D., Skeie, R. B., Fiedler, S., Samset, B. H., Gillett, N. P., Rogelj, J., and Forster, P. M.: Modifying Emissions Scenario Projections to Account for the Effects of COVID-19: Protocol for CovidMIP, Geoscientific Model Development, 14, https://doi.org/10.5194/gmd-14-3683-2021, 2021.

Le, T., Wang, Y., Liu, L., Yang, J., Yung, Y. L., Li, G., and Seinfeld, J. H.: Unexpected Air Pollution with Marked Emission Reductions during the COVID-19 Outbreak in China, Science, 369, https://doi.org/10.1126/science.abb7431, 2020.

Le Quéré, C., Jackson, R. B., Jones, M. W., Smith, A. J. P., Abernethy, S., Andrew, R. M., De-Gol, A. J., Willis, D. R., Shan, Y., Canadell, J. G., Friedlingstein, P., Creutzig, F., and Peters, G. P.: Temporary Reduction in Daily Global CO2 Emissions during the COVID-19 Forced Confinement, Nature Climate Change, 10, https://doi.org/10.1038/s41558-020-0797-x, 2020.

Lee, D. S., Fahey, D. W., Skowron, A., Allen, M. R., Burkhardt, U., Chen, Q., Doherty, S. J., Freeman, S., Forster, P. M., Fuglestvedt, J., Gettelman, A., De León, R. R., Lim, L. L., Lund, M. T., Millar, R. J., Owen, B., Penner, J. E., Pitari, G., Prather, M. J., Sausen, R., and Wilcox, L. J.: The Contribution of Global Aviation to Anthropogenic Climate Forcing for 2000 to 2018, Atmospheric Environment, 244, https://doi.org/10.1016/j.atmosenv.2020.117834, 2021.

Levy, R. C., Mattoo, S., Sawyer, V., Shi, Y., Colarco, P. R., Lyapustin, A. I., Wang, Y., and Remer, L. A.: Exploring Systematic Offsets between Aerosol Products from the Two MODIS Sensors, Atmospheric Measurement Techniques, 11, https://doi.org/10.5194/amt-11-4073-2018, 2018.

Li, J., von Salzen, K., Peng, Y., Zhang, H., and Liang, X.: Evaluation of black carbon semi–direct radiative effect in a climate model, Journal of Geophysical Research: Atmospheres, 118, 4715–4728, https://doi.org/10.1002/jgrd.50327, 2013.

Li, J., Sun, Z., Liu, Y., You, Q., Chen, G., and Bao, Q.: Top-of-Atmosphere Radiation Budget and Cloud Radiative Effects Over the Tibetan Plateau and Adjacent Monsoon Regions From CMIP6 Simulations, Journal of Geophysical Research: Atmospheres, 126, https://doi.org/10.1029/2020JD034345, 2021.

Li, X., Bei, N., Wu, J., Liu, S., Wang, Q., Tian, J., Liu, L., Wang, R., and Li, G.: The Heavy Particulate Matter Pollution During the COVID-19 Lockdown Period in the Guanzhong Basin, China, Journal of Geophysical Research: Atmospheres, 127, https://doi.org/10.1029/2021JD036191, 2022.

Li, Z., Lau, W. K.-M., Ramanathan, V., Wu, G., Ding, Y., Manoj, M. G., Liu, J., Qian, Y., Li, J., Zhou, T., Fan, J., Rosenfeld, D., Ming, Y., Wang, Y., Huang, J., Wang, B., Xu, X., Lee, S.-S., Cribb, M., Zhang, F., Yang, X., Zhao, C., Takemura, T., Wang, K., Xia, X., Yin, Y., Zhang, H., Guo, J., Zhai, P. M., Sugimoto, N., Babu, S. S., and Brasseur, G. P.: Aerosol and Monsoon Climate Interactions over Asia, Reviews of Geophysics, 54, https://doi.org/10.1002/2015RG000500, 2016.

Liu, F., Yon, J., Fuentes, A., Lobo, P., Smallwood, G. J., and Corbin, J. C.: Review of Recent Literature on the Light Absorption Properties of Black Carbon: Refractive Index, Mass Absorption Cross Section, and Absorption Function, Aerosol Science and Technology, 54, https://doi.org/10.1080/02786826.2019.1676878, 2020.

Liu, F., Wang, M., and Zheng, M.: Effects of COVID-19 lockdown on global air quality and health, Science of The Total Environment, 755, https://doi.org/10.1016/j.scitotenv.2020.142533, 2021.

Liu, X., Easter, R. C., Ghan, S. J., Zaveri, R., Rasch, P., Shi, X., Lamarque, J.-F., Gettelman, A., Morrison, H., Vitt, F., Conley, A., Park, S., Neale, R., Hannay, C., Ekman, A. M. L., Hess, P., Mahowald, N., Collins, W., Iacono, M. J., Bretherton, C. S., Flanner, M. G., and Mitchell, D.: Toward a minimal representation of aerosols in climate models: description and evaluation in the Community Atmosphere Model CAM5, Geoscientific Model Development, 5, 709–739, https://doi.org/10.5194/gmd-5-709-2012, 2012.

Lohmann, U. and Feichter, J.: Global indirect aerosol effects: a review, Atmospheric Chemistry and Physics, 5, 715–737, https://doi.org/10.5194/acp-5-715-2005, 2005.

Lund, M., Samset, B., Skeie, R., Watson-Parris, D., Katich, J., Schwarz, J., and Weinzierl, B.: Short Black Carbon lifetime inferred from a global set of aircraft observations, npj Climate and Atmospheric Science, 1, https://doi.org/10.1038/s41612-018-0040-x, 2018.

Lund, M. T., Myhre, G., Skeie, R. B., Samset, B. H., and Klimont, Z.: Implications of Differences between Recent Anthropogenic Aerosol Emission Inventories for Diagnosed AOD and Radiative Forcing from 1990 to 2019, Atmospheric Chemistry and Physics, 23, https://doi.org/10.5194/acp-23-6647-2023, 2023.

Madge, C.: May 2020 becomes the sunniest calendar month on record, URL `https://www.metoffice.gov.uk/about-us/press-office/news/weather-and-climate/2020/2020-spring-and-may-stats`, 2020.

Mangla, R., J, I., and S.s., C.: Inter-Comparison of Multi-Satellites and Aeronet AOD over Indian Region, Atmospheric Research, 240, https://doi.org/10.1016/j.atmosres.2020.104950, 2020.

Mashayekhi, R., Pavlovic, R., Racine, J., Moran, M. D., Manseau, P. M., Duhamel, A., Katal, A., Miville, J., Niemi, D., Peng, S. J., Sassi, M., Griffin, D., and McLinden, C. A.: Isolating the Impact of COVID-19 Lockdown Measures on Urban Air Quality in Canada, Air Quality, Atmosphere & Health, 14, https://doi.org/10.1007/s11869-021-01039-1, 2021.

Matsui, H.: Development of a global aerosol model using a two-dimensional sectional method: 1. Model design, Journal of Advances in Modeling Earth Systems, 9, 1921–1947, https://doi.org/10.1002/2017MS000936, 2017.

Menne, M. J., Durre, I., Korzeniewski, B., McNeal, S., Thomas, K., Yin, X., Anthony, S., Ray, R., Vose, R. S., Gleason, B. E., and Houston, T. G.: Global Historical Climatology Network - Daily (GHCN-Daily), Version 3.28, https://doi.org/10.7289/V5D21VHZ, 2012a.

Menne, M. J., Durre, I., Vose, R. S., Gleason, B. E., and Houston, T. G.: An Overview of the Global Historical Climatology Network - Daily Database, J. Atmos. Oceanic Technol., 29, https://doi.org/10.1175/JTECH-D-11-00103.1, 2012b.

Minnis, P., Ayers, J. K., Palikonda, R., and Phan, D.: Contrails, Cirrus Trends, and Climate, Journal of Climate, 17, https://doi.org/10.1175/1520-0442(2004)017<1671:CCTAC>2.0.CO;2, 2004.

Myhre, G., Berglen, T. F., Johnsrud, M., Hoyle, C. R., Berntsen, T. K., Christopher, S. A., Fahey, D. W., Isaksen, I. S. A., Jones, T. A., Kahn, R. A., Loeb, N., Quinn, P., Remer, L., Schwarz, J. P., and Yttri, K. E.: Modelled radiative forcing of the direct aerosol effect with multi-observation evaluation, Atmospheric Chemistry and Physics, 9, 1365–1392, https://doi.org/10.5194/acp-9-1365-2009, 2009a.

Myhre, G., Kvalevåg, M., Rädel, G., Cook, J., Shine, K., Clarke, H., Karcher, F., Markowicz, K., Kardas, A., Wolkenberg, P., Balkanski, Y., Ponater, M., Forster, P., Rap, A., and Rodriguez De Leon, R.: Intercomparison of Radiative Forcing Calculations of Stratospheric Water Vapour and Contrails, Meteorologische Zeitschrift, 18, https://doi.org/10.1127/0941-2948/2009/0411, 2009b.

Namazi, M., von Salzen, K., and Cole, J. N. S.: Simulation of black carbon in snow and its climate impact in the Canadian Global Climate Model, Atmospheric Chemistry and Physics, 15, 10 887–10 904, https://doi.org/10.5194/acp-15-10887-2015, 2015.

Omar, A. H., Winker, D. M., Vaughan, M. A., Hu, Y., Trepte, C. R., Ferrare, R. A., Lee, K.-P., Hostetler, C. A., Kittaka, C., Rogers, R. R., Kuehn, R. E., and Liu, Z.: The CALIPSO Automated Aerosol Classification and Lidar Ratio Selection Algorithm, Journal of Atmospheric and Oceanic Technology, 26, https://doi.org/10.1175/2009JTECHA1231.1, 2009.

O'Neill, B. C., Tebaldi, C., van Vuuren, D. P., Eyring, V., Friedlingstein, P., Hurtt, G., Knutti, R., Kriegler, E., Lamarque, J.-F., Lowe, J., Meehl, G. A., Moss, R., Riahi, K., and Sanderson, B. M.: The Scenario Model Intercomparison Project (ScenarioMIP) for CMIP6, Geoscientific Model Development, 9, https://doi.org/10.5194/gmd-9-3461-2016, 2016.

Ordóñez, C., Garrido-Perez, J. M., and García-Herrera, R.: Early spring near-surface ozone in Europe during the COVID-19 shutdown: Meteorological effects outweigh emission changes, Science of The Total Environment, 747, https://doi.org/10.1016/j.scitotenv.2020.141322, 2020.

Pan, X., Ichoku, C., Chin, M., Bian, H., Darmenov, A., Colarco, P., Ellison, L., Kucsera, T., da Silva, A., Wang, J., Oda, T., and Cui, G.: Six Global Biomass Burning Emission Datasets: Intercomparison and Application in One Global Aerosol Model, Atmospheric Chemistry and Physics, 20, https://doi.org/10.5194/acp-20-969-2020, 2020.

Parmesan, C., Morecroft, M., Trisurat, Y., Adrian, R., Anshari, G., Arneth, A., Gao, Q., Gonzalez, P., Harris, R., Price, J., Stevens, N., and Talukdarr, G.: Terrestrial and Freshwater Ecosystems and Their Services, chapter 2, Cambridge University Press, Cambridge, United Kingdom and New York, NY, USA, https://doi.org/10.1017/9781009325844.004, 2022.

Paulot, F., Paynter, D., Ginoux, P., Naik, V., and Horowitz, L. W.: Changes in the Aerosol Direct Radiative Forcing from 2001 to 2015: Observational Constraints and Regional Mechanisms, Atmospheric Chemistry and Physics, 18, https://doi.org/10.5194/acp-18-13265-2018, 2018.

Peng, J., Hu, M., Guo, S., Du, Z., Zheng, J., Shang, D., Levy Zamora, M., Zeng, L., Shao, M., Wu, Y.-S., Zheng, J., Wang, Y., Glen, C., Collins, D., Molina, M., and Zhang, R.: Markedly enhanced absorption and direct radiative forcing of black carbon under polluted urban environments, Proceedings of the National Academy of Sciences, 113, 4266–4271, https://doi.org/10.1073/pnas.1602310113, 2016.

Peng, Y. and Lohmann, U.: Sensitivity study of the spectral dispersion of the cloud droplet size distribution on the indirect aerosol effect, Geophysical Research Letters, 30, https://doi.org/10.1029/2003GL017192, 2003.

Persad, G. G., Samset, B. H., and Wilcox, L. J.: Aerosols Must Be Included in Climate Risk Assessments, Nature, 611, https://doi.org/10.1038/d41586-022-03763-9, 2022.

Platnick, S., King, M., and Hubanks, P.: MODIS Atmosphere L3 Monthly Product. NASA MODIS Adaptive Processing System, Goddard Space Flight Center, https://doi.org/dx.doi.org/10.5067/MODIS/MOD08_M3.061, 2017.

Povey, A. C. and Grainger, R. G.: Known and Unknown Unknowns: Uncertainty Estimation in Satellite Remote Sensing, Atmospheric Measurement Techniques, 8, https://doi.org/10.5194/amt-8-4699-2015, 2015.

Quaas, J., Gryspeerdt, E., Vautard, R., and Boucher, O.: Climate Impact of Aircraft-Induced Cirrus Assessed from Satellite Observations before and during COVID-19, Environmental Research Letters, 16, https://doi.org/10.1088/1748-9326/abf686, 2021.

Ramachandran, G. and Reist, P. C.: Characterization of Morphological Changes in Agglomerates Subject to Condensation and Evaporation Using Multiple Fractal Dimensions, Aerosol Science and Technology, 23, 431–442, https://doi.org/10.1080/02786829508965326, 1995.

Ramachandran, S., Rupakheti, M., and Cherian, R.: Insights into Recent Aerosol Trends over Asia from Observations and CMIP6 Simulations, Science of The Total Environment, 807, https://doi.org/10.1016/j.scitotenv.2021.150756, 2022.

Rani, S. and Kumar, R.: Spatial distribution of aerosol optical depth over India during COVID-19 lockdown phase-1, Spatial Information Research, 30, 417–426, https://doi.org/10.1007/s41324-022-00442-9, 2022.

Ranjan, A., Patra, A., and Gorai, A.: Effect of lockdown due to SARS COVID-19 on aerosol optical depth (AOD) over urban and mining regions in India, Science of The Total Environment, 745, https://doi.org/10.1016/j.scitotenv.2020.141024, 2020.

Reddington, C. L., Turnock, S. T., Conibear, L., Forster, P. M., Lowe, J. A., Ford, L. B., Weaver, C., van Bavel, B., Dong, H., Alizadeh, M. R., and Arnold, S. R.: Inequalities in Air Pollution Exposure and Attributable Mortality in a Low Carbon Future, Earth's Future, 11, e2023EF003 697, https://doi.org/https://doi.org/10.1029/2023EF003697, 2023.

Reynolds, R., Rayner, N., Smith, T., Stokes, D., and Wang, W.: An improved in situ and satellite SST analysis for climate, Journal of Climate, 15, 2002.

Riahi, K., van Vuuren, D. P., Kriegler, E., Edmonds, J., O'Neill, B. C., Fujimori, S., Bauer, N., Calvin, K., Dellink, R., Fricko, O., Lutz, W., Popp, A., Cuaresma, J. C., Kc, S., Leimbach, M., Jiang, L., Kram, T., Rao, S., Emmerling, J., Ebi, K., Hasegawa, T., Havlik, P., Humpenöder, F., Da Silva, L. A., Smith, S., Stehfest, E., Bosetti, V., Eom, J., Gernaat, D., Masui, T., Rogelj, J., Strefler, J., Drouet, L., Krey, V., Luderer, G., Harmsen, M., Takahashi, K., Baumstark, L., Doelman, J. C., Kainuma, M., Klimont, Z., Marangoni, G., Lotze-Campen, H., Obersteiner, M., Tabeau, A., and Tavoni, M.: The Shared Socioeconomic Pathways and Their Energy, Land Use, and Greenhouse Gas Emissions Implications: An Overview, Global Environmental Change, 42, https://doi.org/10.1016/j.gloenvcha.2016.05.009, 2017.

Riemer, N., Ault, A. P., West, M., Craig, R. L., and Curtis, J. H.: Aerosol Mixing State: Measurements, Modeling, and Impacts, Reviews of Geophysics, 57, 187–249, https://doi.org/10.1029/2018RG000615, 2019.

Rosenow, J., Fricke, H., Luchkova, T., and Schultz, M.: Minimizing contrail formation by rerouting around dynamic ice-supersaturated regions, Aeron Aero Open Access J., 2, https://doi.org/10.15406/aaoaj.2018.02.00039, 2018.

Samset, B. H.: Aerosol Absorption Has an Underappreciated Role in Historical Precipitation Change, Communications Earth & Environment, 3, https://doi.org/10.1038/s43247-022-00576-6, 2022.

Samset, B. H., Myhre, G., Schulz, M., Balkanski, Y., Bauer, S., Berntsen, T. K., Bian, H., Bellouin, N., Diehl, T., Easter, R. C., Ghan, S. J., Iversen, T., Kinne, S., Kirkevåg, A., Lamarque, J.-F., Lin, G., Liu, X., Penner, J. E., Seland, Ø., Skeie, R. B., Stier, P., Takemura, T., Tsigaridis, K., and Zhang, K.: Black Carbon Vertical Profiles Strongly Affect Its Radiative Forcing Uncertainty, Atmospheric Chemistry and Physics, 13, https://doi.org/10.5194/acp-13-2423-2013, 2013.

Samset, B. H., Myhre, G., Forster, P. M., Hodnebrog, Ø., Andrews, T., Faluvegi, G., Fläschner, D., Kasoar, M., Kharin, V., Kirkevåg, A., Lamarque, J.-F., Olivié, D., Richardson, T., Shindell, D., Shine, K. P., Takemura, T., and Voulgarakis, A.: Fast and Slow Precipitation Responses to Individual Climate Forcers: A PDRMIP Multimodel Study, Geophysical Research Letters, 43, https://doi.org/10.1002/2016GL068064, 2016.

Samset, B. H., Sand, M., Smith, C. J., Bauer, S. E., Forster, P. M., Fuglestvedt, J. S., Osprey, S., and Schleussner, C.-F.: Climate Impacts From a Removal of Anthropogenic Aerosol Emissions, Geophysical Research Letters, 45, https://doi.org/10.1002/2017GL076079, 2018a.

Samset, B. H., Stjern, C. W., Andrews, E., Kahn, R. A., Myhre, G., Schulz, M., and Schuster, G. L.: Aerosol Absorption: Progress Towards Global and Regional Constraints, Current Climate Change Reports, 4, https://doi.org/10.1007/s40641-018-0091-4, 2018b.

Samset, B. H., Fuglestvedt, J. S., and Lund, M. T.: Delayed Emergence of a Global Temperature Response after Emission Mitigation, Nature Communications, 11, https://doi.org/10.1038/s41467-020-17001-1, 2020.

Sand, M., Berntsen, T., von Salzen, K., Flanner, M., Langner, J., and Victor, D.: Response of Arctic temperature to changes in emissions of short-lived climate forcers, Nature Climate Change, 6, 286–289, https://doi.org/10.1038/nclimate2880, 2016.

Sand, M., Samset, B. H., Tsigaridis, K., Bauer, S. E., and Myhre, G.: Black Carbon and Precipitation: An Energetics Perspective, Journal of Geophysical Research: Atmospheres, 125, https://doi.org/10.1029/2019JD032239, 2020.

Sand, M., Samset, B. H., Myhre, G., Gliß, J., Bauer, S. E., Bian, H., Chin, M., Checa-Garcia, R., Ginoux, P., Kipling, Z., Kirkevåg, A., Kokkola, H., Le Sager, P., Lund, M. T., Matsui, H., van Noije, T., Olivié, D. J. L., Remy, S., Schulz, M., Stier, P., Stjern, C. W., Takemura, T., Tsigaridis, K., Tsyro, S. G., and Watson-Parris, D.: Aerosol Absorption in Global Models from AeroCom Phase III, Atmospheric Chemistry and Physics, 21, https://doi.org/10.5194/acp-21-15929-2021, 2021.

Sandhu, A. S. and Baldini, J. U. L.: Evaluating the Significance of the Contrail Effect on Diurnal Temperature Range Using the Eyjafjallajökull Eruption-Related Flight Disruption, \grl, 45, https://doi.org/10.1029/2018GL080899, 2018.

Sassen, K.: Contrail-Cirrus and Their Potential for Regional Climate Change, Bulletin of the American Meteorological Society, 78, https://doi.org/10.1175/1520-0477(1997)078<1885:CCATPF>2.0.CO;2, 1997.

Sayer, A. M., Govaerts, Y., Kolmonen, P., Lipponen, A., Luffarelli, M., Mielonen, T., Patadia, F., Popp, T., Povey, A. C., Stebel, K., and Witek, M. L.: A Review and Framework for the Evaluation of Pixel-Level Uncertainty Estimates in Satellite Aerosol Remote Sensing, Atmospheric Measurement Techniques, 13, https://doi.org/10.5194/amt-13-373-2020, 2020.

Schumann, U., Poll, I., Teoh, R., Koelle, R., Spinielli, E., Molloy, J., Koudis, G. S., Baumann, R., Bugliaro, L., Stettler, M., and Voigt, C.: Air Traffic and Contrail

Changes during COVID-19 over Europe: Amodel Study, Preprint, Clouds and Precipitation/Atmospheric Modelling/Troposphere/Physics (physical properties and processes), https://doi.org/10.5194/acp-2021-62, 2021.

Schuster, G. L., Vaughan, M., MacDonnell, D., Su, W., Winker, D., Dubovik, O., Lapyonok, T., and Trepte, C.: Comparison of CALIPSO aerosol optical depth retrievals to AERONET measurements, and a climatology for the lidar ratio of dust, Atmos. Chem. Phys., 12, 7431–7452, https://doi.org/10.5194/acp-12-7431-2012, 2012.

Schutgens, N., Sayer, A. M., Heckel, A., Hsu, C., Jethva, H., de Leeuw, G., Leonard, P. J. T., Levy, R. C., Lipponen, A., Lyapustin, A., North, P., Popp, T., Poulsen, C., Sawyer, V., Sogacheva, L., Thomas, G., Torres, O., Wang, Y., Kinne, S., Schulz, M., and Stier, P.: An AeroCom–AeroSat Study: Intercomparison of Satellite AOD Datasets for Aerosol Model Evaluation, Atmospheric Chemistry and Physics, 20, https://doi.org/10.5194/acp-20-12431-2020, 2020.

Schutgens, N., Dubovik, O., Hasekamp, O., Torres, O., Jethva, H., Leonard, P. J. T., Litvinov, P., Redemann, J., Shinozuka, Y., de Leeuw, G., Kinne, S., Popp, T., Schulz, M., and Stier, P.: AEROCOM and AEROSAT AAOD and SSA Study – Part 1: Evaluation and Intercomparison of Satellite Measurements, Atmospheric Chemistry and Physics, 21, https://doi.org/10.5194/acp-21-6895-2021, 2021.

Seland, Ø., Bentsen, M., Olivié, D., Toniazzo, T., Gjermundsen, A., Graff, L. S., Debernard, J. B., Gupta, A. K., He, Y.-C., Kirkevåg, A., Schwinger, J., Tjiputra, J., Aas, K. S., Bethke, I., Fan, Y., Griesfeller, J., Grini, A., Guo, C., Ilicak, M., Karset, I. H. H., Landgren, O., Liakka, J., Moseid, K. O., Nummelin, A., Spensberger, C., Tang, H., Zhang, Z., Heinze, C., Iversen, T., and Schulz, M.: Overview of the Norwegian Earth System Model (NorESM2) and key climate response of CMIP6 DECK, historical, and scenario simulations, Geoscientific Model Development, 13, 6165–6200, https://doi.org/10.5194/gmd-13-6165-2020, 2020.

Sellar, A. A., Jones, C. G., Mulcahy, J. P., Tang, Y., Yool, A., Wiltshire, A., O'Connor, F. M., Stringer, M., Hill, R., Palmieri, J., Woodward, S., de Mora, L., Kuhlbrodt, T., Rumbold, S. T., Kelley, D. I., Ellis, R., Johnson, C. E., Walton, J., Abraham, N. L., Andrews, M. B., Andrews, T., Archibald, A. T., Berthou, S., Burke, E., Blockley, E., Carslaw, K., Dalvi, M., Edwards, J., Folberth, G. A., Gedney, N., Griffiths, P. T., Harper, A. B., Hendry, M. A., Hewitt, A. J., Johnson, B., Jones, A., Jones, C. D., Keeble, J., Liddicoat, S., Morgenstern, O., Parker, R. J., Predoi, V., Robertson, E., Siahaan, A., Smith, R. S., Swaminathan, R., Woodhouse, M. T., Zeng, G., and Zerroukat, M.: UKESM1: Description and Evaluation of the U.K. Earth System Model, Journal of Advances in Modeling Earth Systems, 11, 4513–4558, https://doi.org/10.1029/2019MS001739, 2019.

Shettle, E. P. and Fenn, R. W.: Models for the Aerosols of the Lower Atmosphere and the Effects of Humidity Variations on their Optical Properties, vol. 79, Air Force Geophysics Laboratory, Air Force Systems Command, United States, 1979.

Shi, X. and Brasseur, G. P.: The Response in Air Quality to the Reduction of Chinese Economic Activities During the COVID-19 Outbreak, Geophysical Research Letters, 47, https://doi.org/10.1029/2020GL088070, 2020.

Shindell, D. and Smith, C. J.: Climate and Air-Quality Benefits of a Realistic Phase-out of Fossil Fuels, Nature, 573, https://doi.org/10.1038/s41586-019-1554-z, 2019.

Shindell, D., Kuylenstierna, J. C. I., Vignati, E., van Dingenen, R., Amann, M., Klimont, Z., Anenberg, S. C., Muller, N., Janssens-Maenhout, G., Raes, F., Schwartz, J., Faluvegi, G., Pozzoli, L., Kupiainen, K., Höglund-Isaksson, L., Emberson, L., Streets, D., Ramanathan, V., Hicks, K., Oanh, N. T. K., Milly, G., Williams, M., Demkine, V., and Fowler, D.: Simultaneously Mitigating Near-Term Climate Change and Improving Human Health and Food Security, Science, 335, https://doi.org/10.1126/science.1210026, 2012.

Sicard, P., De Marco, A., Agathokleous, E., Feng, Z., Xu, X., Paoletti, E., Rodriguez, J. J. D., and Calatayud, V.: Amplified ozone pollution in cities during the COVID-19 lockdown, Science of The Total Environment, 735, https://doi.org/10.1016/j.scitotenv.2020.139542, 2020.

Siciliano, B., Dantas, G., da Silva, C. M., and Arbilla, G.: Increased ozone levels during the COVID-19 lockdown: Analysis for the city of Rio de Janeiro, Brazil, Science of The Total Environment, 737, https://doi.org/10.1016/j.scitotenv.2020.139765, 2020.

Sigmond, M., Anstey, J., Arora, V., Digby, R., Gillett, N., Kharin, V., Merryfield, W., Reader, C., Scinocca, J., Swart, N., Virgin, J., Abraham, C., Cole, J., Lambert, N., Lee, W.-S., Liang, Y., Malinina, E., Rieger, L., von Salzen, K., Seiler, C., Seinen, C., Shao, A., Sospedra-Alfonso, R., Wang, L., and Yang, D.: Improvements in the Canadian Earth System Model (CanESM) through Systematic Model Analysis: CanESM5.0 and CanESM5.1, Geoscientific Model Development, 16, https://doi.org/10.5194/gmd-16-6553-2023, 2023.

Sillmann, J., Pozzoli, L., Vignati, E., Kloster, S., and Feichter, J.: Aerosol Effect on Climate Extremes in Europe under Different Future Scenarios, Geophysical Research Letters, 40, https://doi.org/10.1002/grl.50459, 2013.

Smith, S., Ahsan, H., and Mott, A.: CEDS v. 2021.04.21 gridded emissions data. Community Emissions Data System (CEDS)., https://doi.org/10.25584/PNNLDataHub/1779095, 2021.

Smith, S. E., Ting, M., Wu, Y., and Zheng, C.: Beyond the Lockdowns: Satellite Observations of Aerosol Optical Depth through 2020, the First Year of the COVID-19 Pandemic, Environmental Research Letters, 17, https://doi.org/10.1088/1748-9326/ac7889, 2022.

Sogacheva, L., Popp, T., Sayer, A. M., Dubovik, O., Garay, M. J., Heckel, A., Hsu, N. C., Jethva, H., Kahn, R. A., Kolmonen, P., Kosmale, M., de Leeuw, G., Levy, R. C., Litvinov, P., Lyapustin, A., North, P., Torres, O., and Arola, A.: Merging Regional and Global Aerosol Optical Depth Records from Major Available Satellite Products, Atmospheric Chemistry and Physics, 20, https://doi.org/10.5194/acp-20-2031-2020, 2020.

Sokhi, R. S., Singh, V., Querol, X., Finardi, S., Targino, A. C., Andrade, M. d. F., Pavlovic, R., Garland, R. M., Massagué, J., Kong, S., Baklanov, A., Ren, L., Tarasova, O., Carmichael, G., Peuch, V.-H., Anand, V., Arbilla, G., Badali, K., Beig, G., Belalcazar, L. C., Bolignano, A., Brimblecombe, P., Camacho, P., Casallas, A., Charland, J.-P., Choi, J., Chourdakis, E., Coll, I., Collins, M., Cyrys, J., da Silva, C. M., Di Giosa, A. D., Di Leo, A., Ferro, C., Gavidia-Calderon, M., Gayen, A., Ginzburg, A., Godefroy, F., Gonzalez, Y. A., Guevara-Luna, M., Haque, S. M., Havenga, H., Herod, D., Hõrrak, U., Hussein, T., Ibarra, S., Jaimes, M., Kaasik, M., Khaiwal, R., Kim, J., Kousa, A., Kukkonen, J., Kulmala, M., Kuula, J., La Violette, N., Lanzani, G., Liu, X., MacDougall, S., Manseau, P. M., Marchegiani, G., McDonald, B., Mishra, S. V., Molina, L. T., Mooibroek, D., Mor, S., Moussiopoulos, N., Murena, F., Niemi, J. V., Noe, S., Nogueira, T., Norman, M., Pérez-Camaño, J. L., Petäjä, T., Piketh, S., Rathod, A., Reid, K., Retama, A., Rivera, O., Rojas, N. Y., Rojas-Quincho, J. P., San José, R., Sánchez, O., Seguel, R. J., Sillanpää, S., Su, Y., Tapper, N., Terrazas, A., Timonen, H., Toscano, D., Tsegas, G., Velders, G. J. M., Vlachokostas, C., von Schneidemesser, E., Vpm, R., Yadav, R., Zalakeviciute, R., and Zavala, M.: A Global Observational Analysis to Understand Changes in Air Quality during Exceptionally Low Anthropogenic Emission Conditions, Environment International, 157, https://doi.org/10.1016/j.envint.2021.106818, 2021.

Song, Q., Zhang, Z., Yu, H., Ginoux, P., and Shen, J.: Global Dust Optical Depth Climatology Derived from CALIOP and MODIS Aerosol Retrievals on Decadal Timescales: Regional and Interannual Variability, Atmospheric Chemistry and Physics, 21, https://doi.org/10.5194/acp-21-13369-2021, 2021.

Song, X., Hu, Y., Ma, Y., Jiang, L., Wang, X., Shi, A., Zhao, J., Liu, Y., Liu, Y., Tang, J., Li, X., Zhang, X., Guo, Y., and Wang, S.: Is short-term and long-term exposure to black carbon associated with cardiovascular and respiratory diseases? A systematic review and meta-analysis based on evidence reliability., BMJ Open, 12, https://doi.org/10.1136/bmjopen-2021-049516, 2022.

Stordal, F., Myhre, G., Stordal, E. J. G., Rossow, W. B., Lee, D. S., Arlander, D. W., and Svendby, T.: Is There a Trend in Cirrus Cloud Cover Due to Aircraft Traffic?, Atmospheric Chemistry & Physics, 5, 2005.

Swart, N. C., Cole, J. N. S., Kharin, V. V., Lazare, M., Scinocca, J. F., Gillett, N. P., Anstey, J., Arora, V., Christian, J. R., Hanna, S., Jiao, Y., Lee, W. G., Majaess, F., Saenko, O. A., Seiler, C., Seinen, C., Shao, A., Sigmond, M., Solheim, L., von Salzen, K., Yang, D., and Winter, B.: The Canadian Earth System Model Version 5 (CanESM5.0.3), Geoscientific Model Development, 12, https://doi.org/10.5194/gmd-12-4823-2019, 2019.

Szopa, S., Naik, V., Adhikary, B., Artaxo, P., Berntsen, T., Collins, W., Fuzzi, S., Gallardo, L., Kiendler Scharr, A., Klimont, Z., Liao, H., Unger, N., and Zanis, P.: Short-Lived Climate Forcers, chapter 6, pp. 817–922, Cambridge University Press, Cambridge, United Kingdom and New York, NY, USA, https://doi.org/10.1017/9781009157896.008, 2021.

Takemura, T., Nakajima, T., Dubovik, O., Holben, B. N., and Kinne, S.: Single-scattering albedo and radiative forcing of various aerosol species with a global three-dimensional model, Journal of Climate, 15, 333–352, https://doi.org/10.1175/1520-0442(2002)015<0333:SSAARF>2.0.CO;2, 2002.

Taylor, J. W., Wu, H., Szpek, K., Bower, K., Crawford, I., Flynn, M. J., Williams, P. I., Dorsey, J., Langridge, J. M., Cotterell, M. I., Fox, C., Davies, N. W., Haywood, J. M., and Coe, H.: Absorption closure in highly aged biomass burning smoke, Atmospheric Chemistry and Physics, 20, 11 201–11 221, https://doi.org/10.5194/acp-20-11201-2020, 2020.

Taylor, K., Williamson, D., and Zwiers, F.: The sea surface temperature and sea-ice concentration boundary conditions for AMIP II simulations, PCMDI Report No. 60, Tech. rep., Program for Climate Model Diagnosis and Intercomparison, University of California, Lawrence Livermore National Laboratory, Livermore, CA 94550, 2000.

Tegen, I., Neubauer, D., Ferrachat, S., Siegenthaler-Le Drian, C., Bey, I., Schutgens, N., Stier, P., Watson-Parris, D., Stanelle, T., Schmidt, H., Rast, S., Kokkola, H., Schultz, M., Schroeder, S., Daskalakis, N., Barthel, S., Heinold, B., and Lohmann, U.: The global aerosol-climate model ECHAM6.3-HAM2.3 - Part 1: Aerosol evaluation, Geoscientific Model Development, 12, 1643–1677, https://doi.org/10.5194/gmd-12-1643-2019, 2019.

Thornhill, G. D., Collins, W. J., Kramer, R. J., Olivié, D., Skeie, R. B., O'Connor, F. M., Abraham, N. L., Checa-Garcia, R., Bauer, S. E., Deushi, M., Emmons, L. K., Forster, P. M., Horowitz, L. W., Johnson, B., Keeble, J., Lamarque, J.-F., Michou, M., Mills, M. J., Mulcahy, J. P., Myhre, G., Nabat, P., Naik, V., Oshima, N., Schulz, M., Smith, C. J., Takemura, T., Tilmes, S., Wu, T., Zeng, G., and Zhang, J.: Effective Radiative Forcing from Emissions of Reactive Gases and Aerosols – a Multi-Model Comparison, Atmospheric Chemistry and Physics, 21, https://doi.org/10.5194/acp-21-853-2021, 2021.

Travis, D. J. and Changnon, S. A.: Evidence of Jet Contrail Influences on Regional-Scale Diurnal Temperature Range, Journal of Weather Modification, 29, 1997.

Travis, D. J., Carleton, A. M., and Lauritsen, R. G.: Climatology: Contrails Reduce Daily Temperature Range, \nat, 418, https://doi.org/10.1038/418601a, 2002.

van der Werf, G. R., Randerson, J. T., Giglio, L., van Leeuwen, T. T., Chen, Y., Rogers, B. M., Mu, M., van Marle, M. J. E., Morton, D. C., Collatz, G. J., Yokelson, R. J., and Kasibhatla, P. S.: Global fire emissions estimates during 1997–2016, Earth System Science Data, 9, 697–720, https://doi.org/10.5194/essd-9-697-2017, 2017.

van Heerwaarden, C. C., Mol, W. B., Veerman, M. A., Benedict, I., Heusinkveld, B. G., Knap, W. H., Kazadzis, S., Kouremeti, N., and Fiedler, S.: Record High Solar Irradiance in Western Europe during First COVID-19 Lockdown Largely Due to Unusual Weather, Communications Earth & Environment, 2, https://doi.org/10.1038/s43247-021-00110-0, 2021.

van Marle, M. J. E., Kloster, S., Magi, B. I., Marlon, J. R., Daniau, A.-L., Field, R. D., Arneth, A., Forrest, M., Hantson, S., Kehrwald, N. M., Knorr, W., Lasslop, G., Li, F., Mangeon, S., Yue, C., Kaiser, J. W., and van der Werf, G. R.: Historic Global Biomass Burning Emissions for CMIP6 (BB4CMIP) Based on Merging Satellite Observations with Proxies and Fire Models (1750–2015), Geoscientific Model Development, 10, https://doi.org/10.5194/gmd-10-3329-2017, 2017.

van Noije, T., Bergman, T., Le Sager, P., O'Donnell, D., Makkonen, R., Gonçalves-Ageitos, M., Döscher, R., Fladrich, U., von Hardenberg, J., Keskinen, J.-P., Korhonen, H., Laakso, A., Myriokefalitakis, S., Ollinaho, P., Pérez García-Pando, C., Reerink, T., Schrödner, R., Wyser, K., and Yang, S.: EC-Earth3-AerChem: a global climate model with interactive aerosols and atmospheric chemistry participating in CMIP6, Geoscientific Model Development, 14, 5637–5668, https://doi.org/10.5194/gmd-14-5637-2021, 2021.

van Vuuren, D., Edmonds, J., Kainuma, M., Riahi, K., Thomson, A., Hibbard, K., Hurtt, G. C., Kram, T., Krey, V., Lamarque, J.-F., Masui, T., Meinshausen, M., Nakicenovic, n., Smith, S. J., and Rose, S. K.: The representative concentration pathways: an overview, Climatic Change, 109, 1573–1480, https://doi.org/10.1007/s10584-011-0148-z, 2011.

van Vuuren, D., Riahi, K., Moss, R., Edmonds, J., Thomson, A., Nakicenovic, N., Kram, T., Berkhoudt, F., Swart, R., Janetos, A., Rose, S., and Arnell, N.: A proposal for a new scenario framework to support research and assessment in different climate research communities, Global Environmental Change, 22, https://doi.org/10.1016/j.gloenvcha.2011.08.002, 2012.

Venter, Z. S., Aunan, K., Chowdhury, S., and Lelieveld, J.: COVID-19 Lockdowns Cause Global Air Pollution Declines, Proceedings of the National Academy of Sciences, 117, https://doi.org/10.1073/pnas.2006853117, 2020.

Verma, S., Ghosh, S., Boucher, O., Wang, R., and Menut, L.: Black carbon health impacts in the Indo-Gangetic plain: Exposures, risks, and mitigation, Science Advances, 8, 21–35, https://doi.org/10.1126/sciadv.abo4093, 2021.

Vogel, A., Alessa, G., Scheele, R., Weber, L., Dubovik, O., North, P., and Fiedler, S.: Uncertainty in Aerosol Optical Depth From Modern Aerosol-Climate Models, Reanalyses, and Satellite Products, Journal of Geophysical Research: Atmospheres, 127, https://doi.org/10.1029/2021JD035483, 2022.

Voigt, C., Kleine, J., Sauer, D., Moore, R. H., Bräuer, T., Le Clercq, P., Kaufmann, S., Scheibe, M., Jurkat-Witschas, T., Aigner, M., Bauder, U., Boose, Y., Borrmann, S., Crosbie, E., Diskin, G. S., DiGangi, J., Hahn, V., Heckl, C., Huber, F., Nowak, J. B., Rapp, M., Rauch, B., Robinson, C., Schripp, T., Shook, M., Winstead, E., Ziemba, L., Schlager, H., and Anderson, B. E.: Cleaner Burning Aviation Fuels Can Reduce Contrail Cloudiness, Communications Earth & Environment, 2, https://doi.org/10.1038/s43247-021-00174-y, 2021.

von Salzen, K.: Piecewise Log-Normal Approximation of Size Distributions for Aerosol Modelling, Atmospheric Chemistry and Physics, 6, https://doi.org/10.5194/acp-6-1351-2006, 2006.

von Salzen, K., Scinocca, J. F., McFarlane, N. A., Li, J., Cole, J. N. S., Plummer, D., Verseghy, D., Reader, M. C., Ma, X., Lazare, M., and Solheim, L.: The Canadian Fourth Generation Atmospheric Global Climate Model (CanAM4). Part I: Representation of Physical Processes, Atmosphere-Ocean, 51, https://doi.org/10.1080/07055900.2012.755610, 2013.

von Salzen, K., Whaley, C. H., Anenberg, S. C., Van Dingenen, R., Klimont, Z., Flanner, M. G., Mahmood, R., Arnold, S. R., Beagley, S., Chien, R.-Y., Christensen, J. H., Eckhardt, S., Ekman, A. M. L., Evangeliou, N., Faluvegi, G., Fu, J. S., Gauss, M., Gong, W., Hjorth, J. L., Im, U., Krishnan, S., Kupiainen, K., Kühn, T., Langner, J., Law, K. S., Marelle, L., Olivié, D., Onishi, T., Oshima, N., Paunu, V.-V., Peng, Y., Plummer, D., Pozzoli, L., Rao, S., Raut, J.-C., Sand, M., Schmale, J., Sigmond, M., Thomas, M. A., Tsigaridis, K., Tsyro, S., Turnock, S. T., Wang, M., and Winter, B.: Clean Air Policies Are Key for Successfully Mitigating Arctic Warming, Communications Earth & Environment, 3, https://doi.org/10.1038/s43247-022-00555-x, 2022.

Wang, H., Easter, R. C., Zhang, R., Ma, P.-L., Singh, B., Zhang, K., Ganguly, D., Rasch, P. J., Burrows, S. M., Ghan, S. J., Lou, S., Qian, Y., Yang, Y., Feng, Y., Flanner, M., Leung, L. R., Liu, X., Shrivastava, M., Sun, J., Tang, Q., Xie, S., and Yoon, J.-H.: Aerosols in the E3SM Version 1: New Developments and Their Impacts on Radiative Forcing, Journal of Advances in Modeling Earth Systems, 12, e2019MS001 851, https://doi.org/10.1029/2019MS001851, 2019.

Wang, H., Peng, Y., von Salzen, K., Yang, Y., Zhou, W., and Zhao, D.: Evaluation of a quasi-steady-state approximation of the cloud droplet growth equation (QDGE) scheme for aerosol activation in global models using multiple aircraft data over both continental and marine environments, Geoscientific Model Development, 15, 2949–2971, https://doi.org/10.5194/gmd-15-2949-2022, 2022.

Wang, L., Li, M., Yu, S., Chen, X., Li, Z., Zhang, Y., Jiang, L., Xia, Y., Li, J., Liu, W., Li, P., Lichtfouse, E., Rosenfeld, D., and Seinfeld, J. H.: Unexpected Rise of Ozone in Urban and Rural Areas, and Sulfur Dioxide in Rural Areas during the Coronavirus City Lockdown in Hangzhou, China: Implications for Air Quality, Environmental Chemistry Letters, 18, https://doi.org/10.1007/s10311-020-01028-3, 2020.

Wang, R., Balkanski, Y., Boucher, O., Ciais, P., Schuster, G. L., Chevallier, F., Samset, B. H., Liu, J., Piao, S., Valari, M., and Tao, S.: Estimation of Global Black Carbon Direct Radiative Forcing and Its Uncertainty Constrained by Observations, Journal of Geophysical Research: Atmospheres, 121, https://doi.org/10.1002/2015JD024326, 2016.

Wang, R., Andrews, E., Balkanski, Y., Boucher, O., Myhre, G., Samset, B. H., Schulz, M., Schuster, G. L., Valari, M., and Tao, S.: Spatial Representativeness Error in the Ground-Level Observation Networks for Black Carbon Radiation Absorption, Geophysical Research Letters, 45, 2106–2114, https://doi.org/10.1002/2017GL076817, 2018.

Wang, Z., Lin, L., Xu, Y., Che, H., Zhang, X., Zhang, H., Dong, W., Wang, C., Gui, K., and Xie, B.: Incorrect Asian Aerosols Affecting the Attribution and Projection of Regional Climate Change in CMIP6 Models, npj Climate and Atmospheric Science, 4, https://doi.org/10.1038/s41612-020-00159-2, 2021.

Watson-Parris, D., Christensen, M. W., Laurenson, A., Clewley, D., Gryspeerdt, E., and Stier, P.: Shipping Regulations Lead to Large Reduction in Cloud Perturbations, Proceedings of the National Academy of Sciences, 119, https://doi.org/10.1073/pnas.2206885119, 2022.

Weber, J., Shin, Y. M., Sykes, J. S., Archer-Nicholls, S., Abraham, N. L., and Archibald, A. T.: Minimal Climate Impacts From Short-Lived Climate Forcers Following Emission Reductions Related to the COVID-19 Pandemic, Geophysical Research Letters, 47, https://doi.org/10.1029/2020GL090326, 2020.

Wei, J., Peng, Y., Mahmood, R., Sun, L., and Guo, J.: Intercomparison in Spatial Distributions and Temporal Trends Derived from Multi-Source Satellite Aerosol Products, Atmospheric Chemistry and Physics, 19, https://doi.org/10.5194/acp-19-7183-2019, 2019.

Wei, J., Li, Z., Sun, L., Peng, Y., Liu, L., He, L., Qin, W., and Cribb, M.: MODIS Collection 6.1 3 Km Resolution Aerosol Optical Depth Product: Global Evaluation and Uncertainty Analysis, Atmospheric Environment, 240, https://doi.org/10.1016/j.atmosenv.2020.117768, 2020.

Wei, L., Lu, Z., Wang, Y., Liu, X., Wang, W., Wu, C., Zhao, X., Rahimi, S., Xia, W., and Jiang, Y.: Black Carbon-Climate Interactions Regulate Dust Burdens over India Revealed during COVID-19, Nature Communications, 13, https://doi.org/10.1038/s41467-022-29468-1, 2022.

Westervelt, D. M., You, Y., Li, X., Ting, M., Lee, D. E., and Ming, Y.: Relative Importance of Greenhouse Gases, Sulfate, Organic Carbon, and Black Carbon Aerosol for South Asian Monsoon Rainfall Changes, Geophysical Research Letters, 47, https://doi.org/10.1029/2020GL088363, 2020.

Winker, D. M., Vaughan, M. A., Omar, A., Hu, Y., Powell, K. A., Liu, Z., Hunt, W. H., and Young, S. A.: Overview of the CALIPSO Mission and CALIOP Data Processing Algorithms, Journal of Atmospheric and Oceanic Technology, 26, https://doi.org/10.1175/2009JTECHA1281.1, 2009.

World Health Organization: `https://www.who.int/emergencies/disease-outbreak-news/item/2020-DON229`, last accessed 2022-12-05, 2020a.

World Health Organization: `https://www.who.int/director-general/speeches/detail/who-director-general-s-opening-remarks-at-the-media-briefing-on-covid-19`, last accessed 2022-12-05, 2020b.

Wu, K., Li, J., von Salzen, K., and Zhang, F.: Explicit solutions to the mixing rules with three-component inclusions, Journal of Quantitative Spectroscopy and Radiative Transfer, 207, 78–82, https://doi.org/10.1016/j.jqsrt.2017.12.020, 2018.

Wyche, K., Nichols, M., Parfitt, H., Beckett, P., Gregg, D., Smallbone, K., and Monks, P.: Changes in ambient air quality and atmospheric composition and reactivity in the South East of the UK as a result of the COVID-19 lockdown, Science of The Total Environment, 755, https://doi.org/10.1016/j.scitotenv.2020.142526, 2021.

Xie, X., Myhre, G., Liu, X., Li, X., Shi, Z., Wang, H., Kirkevåg, A., Lamarque, J.-F., Shindell, D., Takemura, T., and Liu, Y.: Distinct Responses of Asian Summer Monsoon to Black Carbon Aerosols and Greenhouse Gases, Atmospheric Chemistry and Physics, 20, https://doi.org/10.5194/acp-20-11823-2020, 2020.

Xu, K., Cui, K., Young, L.-H., Hsieh, Y.-K., Wang, Y.-F., Zhang, J., and Wan, S.: Impact of the COVID-19 Event on Air Quality in Central China, Aerosol and Air Quality Research, 20, https://doi.org/10.4209/aaqr.2020.04.0150, 2020.

Yang, J., Sakhvidi, M. J. Z., de Hoogh, K., Vienneau, D., Siemiatyck, J., Zins, M., Goldberg, M., Chen, J., Lequy, E., and Jacquemin, B.: Long-term exposure to black carbon and mortality: A 28-year follow-up of the GAZEL cohort, Environment International, 157, https://doi.org/10.1016/j.envint.2021.106805, 2021.

Yang, P., Hong, G., Dessler, A. E., Ou, S. S. C., Liou, K.-N., Minnis, P., and Harshvardhan: Contrails and Induced Cirrus: Optics and Radiation, Bulletin of the American Meteorological Society, 91, https://doi.org/10.1175/2009BAMS2837.1, 2010.

Young, S. A., Vaughan, M. A., Garnier, A., Tackett, J. L., Lambeth, J. D., and Powell, K. A.: Extinction and Optical Depth Retrievals for CALIPSO's Version 4 Data Release, Atmospheric Measurement Techniques, 11, https://doi.org/10.5194/amt-11-5701-2018, 2018.

Yu, H., Chin, M., Bian, H., Yuan, T., Prospero, J. M., Omar, A. H., Remer, L. A., Winker, D. M., Yang, Y., Zhang, Y., and Zhang, Z.: Quantification of trans-Atlantic dust transport from seven-year (2007–2013) record of CALIPSO lidar measurements, Remote Sensing of Environment, 159, 232–249, https://doi.org/10.1016/j.rse.2014.12.010, 2015.

Yukimoto, S., Kawai, H., Koshiro, T., Oshima, N., Yoshida, K., Urakawa, S., Tsujino, H., Deushi, M., Tanaka, T., Hosaka, M., Yabu, S., Yoshimura, H., Shindo, E., Mizuta, R., Obata, A., Adachia, Y., and Ishii, M.: The Meteorological Research Institute Earth System Model Version 2.0, MRI-ESM2.0: Description and Basic Evaluation of the Physical Component, Journal of the Meteorological Society of Japan. Ser. II, 97, 931–965, https://doi.org/10.2151/jmsj.2019-051, 2019.

Zanatta, M., Mertes, S., Jourdan, O., Dupuy, R., Järvinen, E., Schnaiter, M., Eppers, O., Schneider, J., Jurányi, Z., and Herber, A.: Airborne Investigation of Black Carbon Interaction with Low-Level, Persistent, Mixed-Phase Clouds in the Arctic Summer, Atmospheric Chemistry and Physics, 23, https://doi.org/10.5194/acp-23-7955-2023, 2023.

Zerefos, C. S., Eleftheratos, K., Balis, D. S., Zanis, P., Tselioudis, G., and Meleti, C.: Evidence of Impact of Aviation on Cirrus Cloud Formation, Atmospheric Chemistry & Physics, 3, 2003.

Zhang, J. and Rothrock, D.: Modeling Global Sea Ice with a Thickness and Enthalpy Distribution Model in Generalized Curvilinear Coordinates, Monthly Weather Review, 131, https://doi.org/10.1175/1520-0493(2003)131<0845:MGSIWA>2.0.CO;2, 2003.

Zhang, L., Gong, S., Padro, J., and Barrie, L.: A size-segregated particle dry deposition scheme for an atmospheric aerosol module, Atmospheric Environment, 35, 49–560, 2001.

Zhao, A., Ryder, C. L., and Wilcox, L. J.: How Well Do the CMIP6 Models Simulate Dust Aerosols?, Atmospheric Chemistry and Physics, 22, https://doi.org/10.5194/acp-22-2095-2022, 2022.

Zhao, M., Golaz, J.-C., Held, I. M., Guo, H., Balaji, V., Benson, R., Chen, J.-H., Chen, X., Donner, L. J., Dunne, J. P., Dunne, K., Durachta, J., Fan, S.-M., Freidenreich, S. M., Garner, S. T., Ginoux, P., Harris, L. M., Horowitz, L. W., Krasting, J. P., Langenhorst, A. R., Liang, Z., Lin, P., Lin, S.-J., Malyshev, S. L., Mason, E., Milly, P. C. D., Ming, Y., Naik, V., Paulot, F., Paynter, D., Phillipps, P., Radhakrishnan, A., Ramaswamy, V., Robinson, T., Schwarzkopf, D., Seman, C. J., Shevliakova, E., Shen, Z., Shin, H., Silvers, L. G., Wilson, J. R., Winton, M., Wittenberg, A. T., Wyman, B., and Xiang, B.: The GFDL Global Atmosphere and Land Model AM4.0/LM4.0: 1. Simulation Characteristics With Prescribed SSTs, Journal of Advances in Modeling Earth Systems, 10, 691–734, https://doi.org/10.1002/2017MS001208, 2018.

Zheng, B., Tong, D., Li, M., Liu, F., Hong, C., Geng, G., Li, H., Li, X., Peng, L., Qi, J., Yan, L., Zhang, Y., Zhao, H., Zheng, Y., He, K., and Zhang, Q.: Trends in China's Anthropogenic Emissions since 2010 as the Consequence of Clean Air Actions, Atmospheric Chemistry and Physics, 18, https://doi.org/10.5194/acp-18-14095-2018, 2018.

Zheng, Y. and Unger, N.: Reducing Planetary Health Risks Through Short-Lived Climate Forcer Mitigation, GeoHealth, 5, https://doi.org/10.1029/2021GH000422, 2021.

Zhou, W., Lei, L., Du, A., Zhang, Z., Li, Y., Yang, Y., Tang, G., Chen, C., Xu, W., Sun, J., Li, Z., Fu, P., Wang, Z., and Sun, Y.: Unexpected Increases of Severe Haze Pollution During the Post COVID-19 Period: Effects of Emissions, Meteorology, and Secondary Production, Journal of Geophysical Research: Atmospheres, 127, https://doi.org/10.1029/2021JD035710, 2022.

Ziehn, T., Chamberlain, M. A., Law, R. M., Lenton, A., Bodman, R. W., Dix, M., Stevens, L., Wang, Y., and Srbinovsky, J.: The Australian Earth System Model: ACCESS-ESM1.5, Journal of Southern Hemisphere Earth Systems Science, 70, 193–214, https://doi.org/10.1071/ES19035, 2020.

Zuo, H., Balmaseda, M., and Mogensen, K.: The new eddy-permitting ORAP5 ocean reanalysis: description, evaluation and uncertainties in climate signals, Climate Dynamics, 49, https://doi.org/10.1007/s00382-015-2675-1, 2017.